UNIVERSITY OF OKLAHOMA

GRADUATE COLLEGE

MAPPING HYDRAULIC FRACTURE USING SHEAR WAVE

A THESIS

SUBMITTED TO THE GRADUATE FACULTY

in partial fulfillment of the requirements for the

Degree of

MASTER OF SCIENCE

By

PRITESH BHOUMICK
Norman, Oklahoma
2018

MAPPING HYDRAULIC FRACTURE USING SHEAR WAVE

A THESIS APPROVED FOR THE
MEWBOURNE SCHOOL OF PETROLEUM AND GEOLOGICAL ENGINEERING

BY

Dr. Carl H. Sondergeld, Chair

Dr. Chandra S. Rai

Dr. Siddharth Misra

To my parents Dhanesh and Tapati, and my sister Pupul for their unconditional love and never-ending support.

ACKNOWLEDGEMENTS

I am indebted to my advisors, Dr. Carl Sondergeld and Dr. Chandra Rai, for providing me with the opportunity to be part of their Integrated Core Characterization Center (IC^3) research group. Their intellect, subject knowledge and passion for petrophysical research is amazing and have been a great source of motivation for me. I feel lucky to have them as my advisors. I am sincerely thankful to Dr. Siddharth Misra for his valuable inputs in reviewing my thesis, and for being a part of my thesis committee.

I am deeply thankful to Bruce Spears for spearheading the experimental setup for this research and providing valuable technical support at every juncture of my work. I am thankful to Gary Stowe for his help during the various stages of this research work.

I appreciate the efforts of my fellow IC^3 friends Abhinav Mittal, Son Dang and Akash Damani for guiding me during the research work. I would also like to thank my friends Pratiksha Tathed and Goutham Talluru for being a family away from home and for making my life at OU, a memorable one.

I express my sincere gratitude to my parents and my sister for their love, patience and support. My accomplishments so far are as much theirs as they are mine.

TABLE OF CONTENTS

LIST OF TABLES

LIST OF FIGURES

ABSTRACT

It has become critical to understand the location of hydraulic fracture and the extent to which it stimulates a reservoir to plan future drilling and completions. Various methods have been used to map the fracture propagation. Microseismic event mapping is a common field technique which uses the elastic energy generated during the fracturing process (see Albright and Pearson, 1982, Rutledge and Phillips, 2003 and Warpinski et al., 2004). Acoustic emission are utilized in mapping hydraulic fractures and assessing fracture mechanisms in laboratory studies as well (Matsunaga et al., 1993, Masuda et al., 2003, Damani et al., 2012). Other methods include using temperature sensors to monitor the fracture propagation in real time (Holley et al., 2010). Scanning Electron Microscopy (SEM) is used to image and map the Stimulated Reservoir Volume (SRV) of the fracture generated in laboratory experiments (Damani et al., 2012). With the advancements in Computed Tomography, it is possible to acquire artificially created 3-D fracture structures as well as the fracture aperture maps (Karpyn et al., 2003). Electromagnetic geophysical principles also offer a method to determine the location of the proppant in the far-field of fractured wells (Palisch et al., 2017). Electromagnetic transmitters are lowered to the fracture zone in the well and response is measured by surface receivers. Electrically conducting proppant is introduced into the fractured zone (Cannan 2015; Aldridge 2016). Measurement is taken before fracturing and post-fracture to estimate the difference due to the proppant introduction and estimate the SRV (Rassenfoss, 2016). Digital Image Correlation techniques helps to analyze the strain development over the surface of the sample in real time providing fracture initiation and propagation, however, it is also limited to laboratory scale measurement (Mokhtari et al., 2017). Methods, such as SEM provide detailed fracture imaging; they are incapable of

capturing the macroscale of the fracture system or the near-real-time fracture development, and suitable only for laboratory observation.

Even with the extensive use of hydraulic fracturing, a fundamental understanding in the micro-scale is lacking. This experimental investigation is aimed at understanding the complexity of hydraulic fracturing using polarized shear wave attributes. We studied the shear wave response in one 6" diameter, 6" in length cylindrical Tennessee sandstone (vertical core) and 2 pyrophyllite samples (horizontal cores) before and after fracturing and analysed the change in the shear wave travel time, and signal attenuation to map fracture density and morphology.

Each sample is hydraulically fractured under uniaxial conditions (Tennessee sandstone fractured using water; one pyrophyllite sample fractured using water, other one with oil) with an effective maximum stress of ≈830 psi applied perpendicular to the natura foliation. Tennessee sandstone sample is isotropic while the pyrophyllite samples exhibit a P-wave anisotropy of 20% and displays transverse anisotropy. Acoustic emissions (AE) were recorded using sixteen 1-MHz piezoelectric P-wave transducers; the spatial acoustic emission density was mapped. Berryman's strong anisotropy model was used to build an anisotropic velocity model for AE event locations for pyrophyllite samples. Post-fracturing polarized shear wave velocity measurements were conducted using an array of seven pairs of polarized shear wave transducers to record discrete shear wave velocity measurements. Fourier analysis of the post-failure recorded shear waveforms mapped attenuation associated with the stimulated reservoir volume which was consistent with the shear wave velocity analysis. Using O'Connell and Budiansky's Self-Consistent model (O' Connell and Budiansky, 1974), crack density is also mapped for the fractured sample.

Maximum shear wave velocity reduction observed (for both shear wave polarizations) in Tennessee sandstone is 24% post fracture, while it is as high as 30% in pyrophyllite fractured using water and is around 25% in pyrophyllite fractured using oil. Shear wave frequency map is consistent with the physically observed fracture for Tennessee sandstone as well as both the pyrophyllite samples. Crack density is observed to be more than twice in Tennessee sandstone (0.18 – 0.28) compared to in pyrophyllite (0.09 – 0.12). Secondary microfractures appear normal to the primary fractures in the horizontal plane in all three samples.

1 INTRODUCTION

1.1 Background

Hydraulic fracturing in combination with horizontal drilling has made the extraction of hydrocarbon from unconventional shale resources economically feasible. It has spurred an oil and gas "boom" in various parts of the country.

The extensive use of hydraulic fracturing in unconventional well completions, particularly in shale wells, has resulted in a $20 billion industry (Figure 1.1) (Economides, 2011).

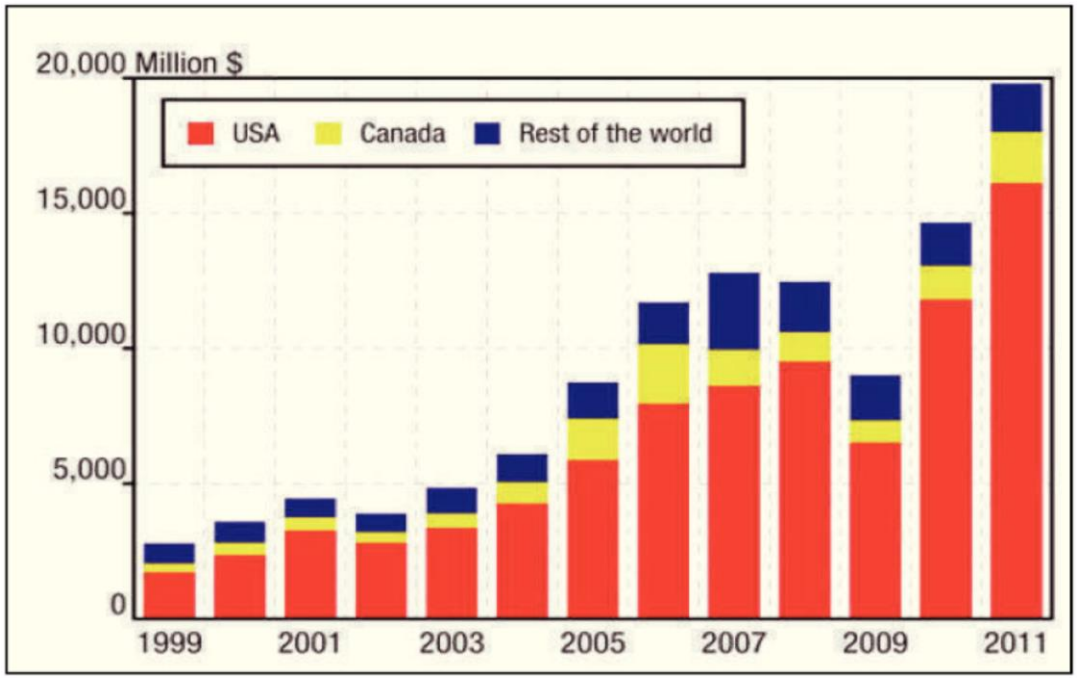

Figure 1.1 Global hydraulic fracturing market value. U.S. continues to be the leader in hydraulic fracturing (Economides, 2011)

The proportion of natural gas extracted using hydraulic fracturing has seen a dramatic rise from 23% (API, American Petroleum Institute, 2013) in 2011 to nearly 50% in 2015 (Prince and Tovar, 2015). As much as two-thirds of natural gas is extracted using hydraulic fracturing (EIA, 2018). Over half of the natural gas produced in 2017 in the U.S. was from tight gas and shale formations, predominantly produced using hydraulic fracturing (Loomis and Haefele,

2017). The shale gas and tight gas plays proportion is projected to rise to more than two-third by 2050 (see Figure 1.2).

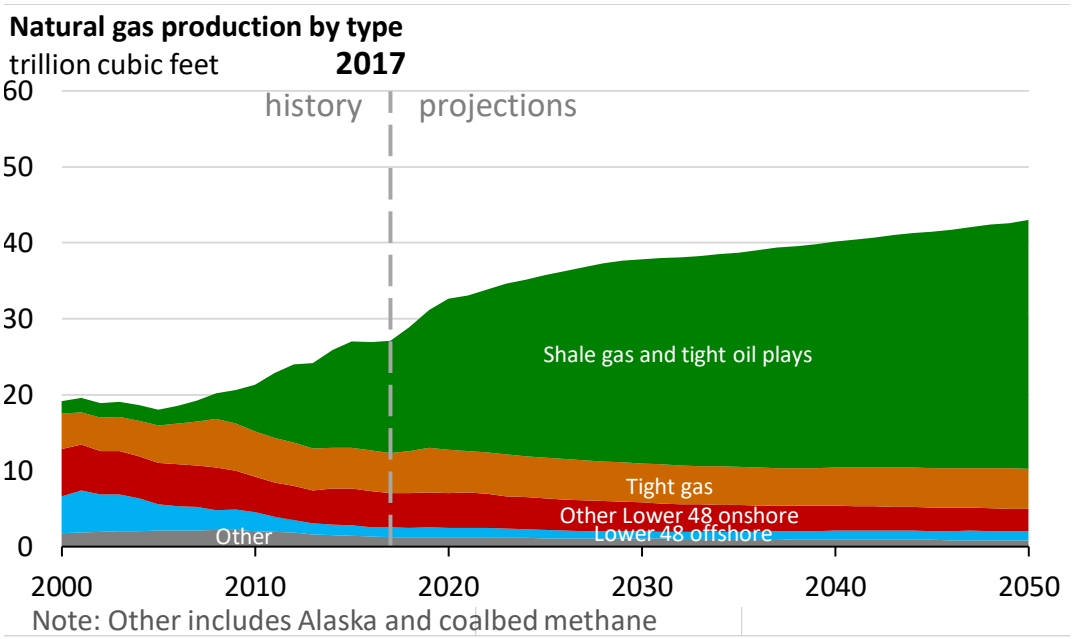

Figure 1.2 U.S. dry natural gas production by source (EIA, Annual Energy Outlook, 2018)

1.2 Shale gas and tight gas

Large-scale natural gas production from shale began around 2000, when shale gas production became a commercial reality in the Barnett. The production of Barnett shale natural gas was pioneered by the Mitchell Energy and Development Corporation in 1981 (EIA, 2017). By 2000, the company had developed a hydraulic fracturing technique that produced commercial volumes of shale gas. Alongside the commercial success at the Barnett shale, other companies started drilling wells in this formation and by 2005, Barnett shale was producing almost half a trillion cubic feet of natural gas per year. Consequently, companies began developing other shale formations in U.S. as well (Loomis and Haefele, 2017). 19 prolific shale plays are identified by EIA (2016). (see Figure 1.3)

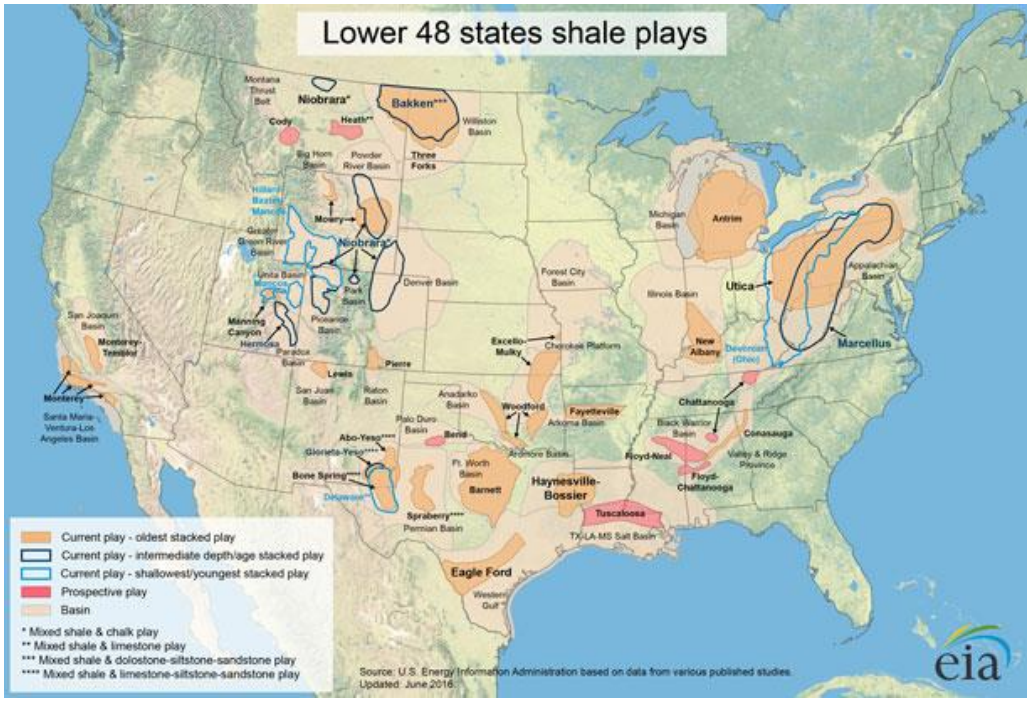

Figure 1.3 Geographical distribution of U.S. shale plays (EIA, Annual Energy Outlook, 2016)

1.3 Hydraulic fracturing

Hydraulic fracturing is critical to the economical production of hydrocarbons from unconventional formations. It constitutes nearly a quarter of the well development cost (see Figure 1.4).

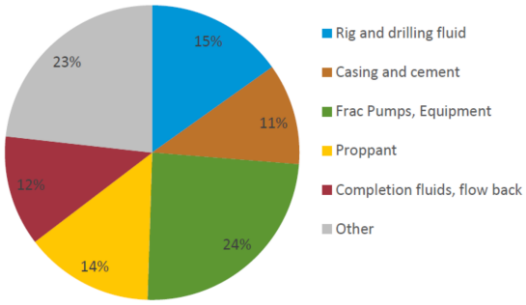

Figure 1.4 Percentage breakdown of cost shares for U.S. onshore oil and natural gas drilling and completion (EIA, 2016)

There are arguments that state that the physical laws governing fractures are known and fracture models are accurate, but the emergence of 'new mechanisms' every few years suggests

that the basic physics incorporated into models has not been as comprehensive as required to model a fracture fully (Warpinski, 1996).

Hydraulic fracturing is the process of forcing a fluid (primarily water) under high pressure from a wellbore against a rock formation until the rock fractures. As the flow rate increases, the pressure differential also increases consequently creating a stress in the formation; increasing the rate, eventually leads to a stress greater than the maximum stress that can be sustained by the formation and the rock physically splits apart. The fracture lengthens and widens as the high-pressure liquid in the wellbore is pumped into the formation. This injected liquid contains proppant or other small solid particles (usually sand or granular man made solid of similar size and property) filling the expanding fracture. When the injection is stopped, and the fluid pressure decreases, and the formation settles back to its original configuration; however, the presence of proppant keeps the fracture open. This allows the hydrocarbon, such as crude oil and natural gas to flow through the rock formation into the wellbore and consequently to the surface.

Using well completion and production data from DrillingInfo and IHS Global Insight, EIA created a profile of oil production in the United States. In 2000, approximately 23,000 hydraulically fractured wells produced 102,000 barrels per day (b/d) of oil, making up less than 2% of the national total. By 2015, the number of hydraulically fractured wells grew to an estimated 300,000, and production from those wells had grown to more than 4.3 million b/d, making up about 50% of the total oil output of the United States (Figure 1.5). These results may vary from other sources because of the types of wells included in the analysis and update schedules of source databases (EIA, 2016).

This new oil production has primarily come from shale and other tight rocks in the Eagle Ford formation and Permian Basin of Texas, and the Bakken and Three Forks formation of Montana and North Dakota (Figure 1.6).

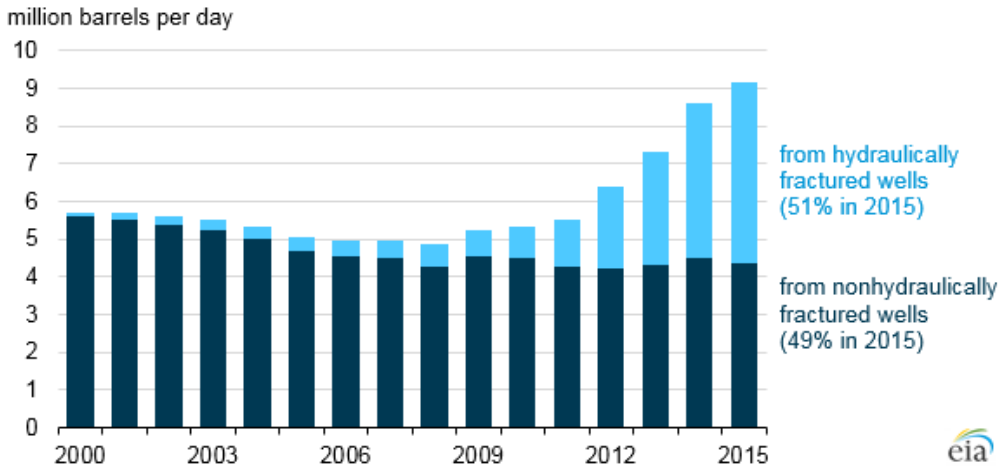

Figure 1.5 Comparison of Oil Production in U.S. by hydraulically fractured and non-hydrulically fractured wells (2000-2015) (EIA, 2016)

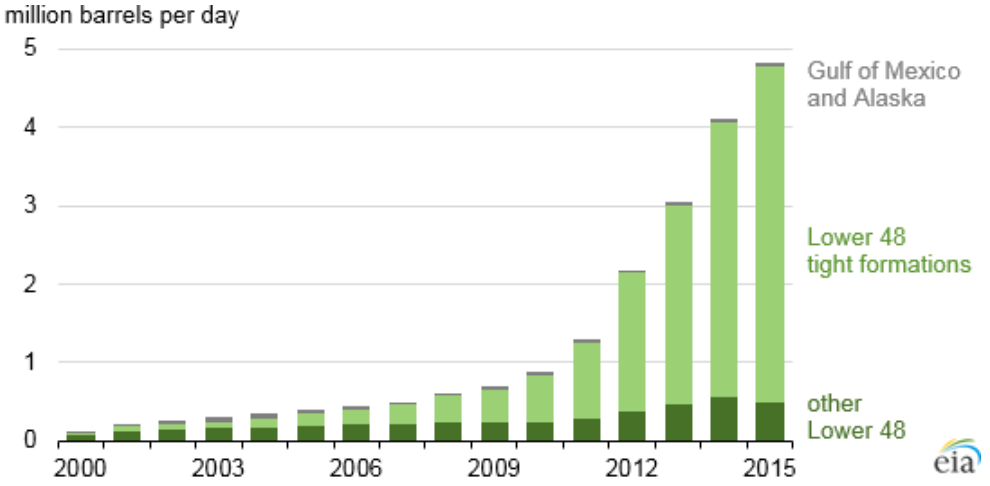

Figure 1.6 Oil production from hydraulically fractured wells in U.S. (2000-2015) (EIA, 2016).

1.4 Motivation

It has become critical to understand the location of hydraulic fracture and the extent to which it stimulates a reservoir to plan future drilling and completions. Various methods have been

used to map the fracture propagation. Microseismic event mapping is a common field technique which uses the elastic energy generated during the fracturing process (see Albright and Pearson, 1982, Rutledge and Phillips, 2003 and Warpinski et al., 2004). Acoustic emission are utilized in mapping hydraulic fractures and assessing fracture mechanisms in laboratory studies as well (Matsunaga et al., 1993, Masuda et al., 2003, Damani et al., 2012). Other methods include using temperature sensors to monitor the fracture propagation in real time (Holley et al., 2010). Scanning Electron Microscopy (SEM) is used to image and map the Stimulated Reservoir Volume (SRV) of the fracture generated in laboratory experiments (Damani et al., 2012). With the advancements in Computed Tomography, it is possible to acquire artificially created 3-D fracture structures as well as the fracture aperture maps (Karpyn et al., 2003). Electromagnetic geophysical principles also offer a method to determine the location of the proppant in the far-field of fractured wells (Palisch et al., 2017). Electromagnetic transmitters are lowered to the fracture zone in the well and response is measured by surface receivers. Electrically conducting proppant is introduced into the fractured zone (Cannan 2015; Aldridge 2016). Measurement is taken before fracturing and post-fracture to estimate the difference due to the proppant introduction and estimate the SRV (Rassenfoss, 2016). Digital Image Correlation techniques helps to analyze the strain development over the surface of the sample in real time providing fracture initiation and propagation, however, it is also limited to laboratory scale measurement (Mokhtari et al., 2017). Methods, such as SEM provide detailed fracture imaging; they are incapable of capturing the macroscale of the fracture system or the near-real-time fracture development, and suitable only for laboratory observation.

Even with the extensive use of hydraulic fracturing, a fundamental understanding in the micro-scale is lacking.

1.5 Research Objective

This experimental investigation is aimed at understanding the complexity of hydraulic fracturing using polarized shear wave attributes. We studied the shear wave response in samples before and after fracturing and analysed the change in the shear wave travel time, and signal attenuation to map fracture density and morphology.

1.6 Synopsis

This thesis is divided into 5 chapters:

Chapter 1 is a brief background and introduction to hydraulic fracturing and polarized shear wave technology used for hydraulic fracture mapping.

Chapter 2 provides the theoretical background to hydraulic fracturing and polarized shear wave technology along with a brief description of previous laboratory and field experiments on hydraulic fracturing and shear wave analysis.

Chapter 3 describes the experimental methodology. Specifications of the instrumentation used, and the rock samples tested reported.

Chapter 4 lists the results and interpretation of the findings.

Chapter 5 lists the major findings of this research and their contribution towards improving interpretation of polarized shear wave response for hydraulic fracture mapping.

Chapter 6 lists the benefits and application of this research

2 LITERATURE SURVEY

2.1 History

The first attempts at fracturing formations for improving production were not hydraulic in nature – they were mostly explosives that were used to break the formation and provide a channel from the reservoir to the wellbore. There are records that mention such practice was followed as early as 1890s. Such processes to stimulate reservoir reached its conclusion with the experimental use of nuclear devices to fracture a relatively shallow, low-permeability formations, in the late 1940s and early 1960s (Coffer et al., 1964 and Howard and Fast, 1970).

By late 1930s, acidizing became an accepted technique for well stimulation. It was observed by several practitioners that injectivity would dramatically increase above a certain "breakdown" pressure (Grebe and Stosser, 1935). It is highly probable that most of the acid treatments carried out then were in fact acid fractures. In 1940, Torrey noticed the pressure-induced fracturing of formations based on his observation during squeeze cementing operations. He presented the data that pressure above a certain value can part the rocks along its bedding plane or other lines of "sedimentary weakness". Similar observations were made by Grebe in 1943 and by Yuster and Calhaun in 1945 for water injection wells.

The first commercial hydraulic fracturing process for stimulation was performed in the Hugoton gas field in Western Kansas, in 1947. It was an unpropped treatment carried out to improve the productivity of Klepper Gas Unit No. 1 well. The well was completed with four gas-producing limestone intervals, one of which had been previously treated with acid. Four separate treatments were pumped, one for each zone, with a primitive packer being employed for isolation. The fluid used for the treatment was war-surplus napalm, an extremely hazardous

operation. In total, 3000 gals of fluid were pumped into each formation (Economides and Martin, 2007). (Figure 2.1)

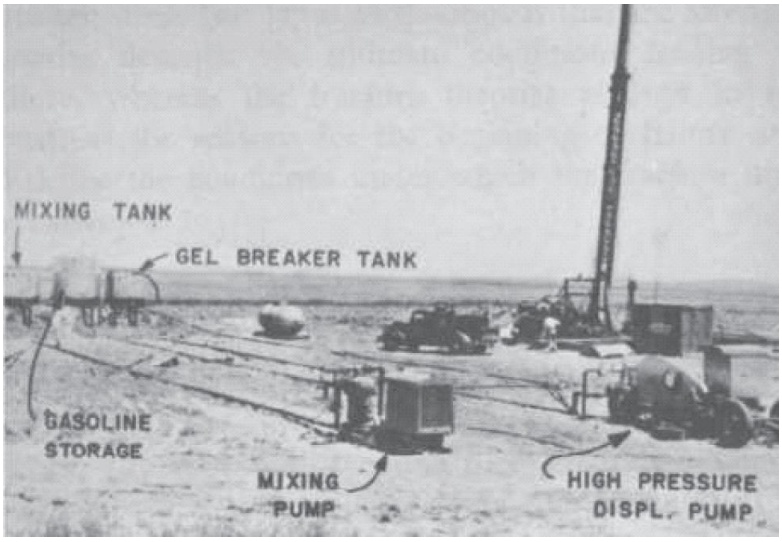

Figure 2.1 Klepper Gas Unit No. 1, Hugoton field, Kansas: The very first frac job

The gas injectivity of some zones increased relative to others post-treatment tests, however, the overall deliverability did not increase. Hydraulic fracture, therefore, could not replace acidizing for limestone formations. However, later in mid-1960s, propped hydraulic fracturing had replaced acidizing as the preferred stimulation method in the Hugoton field.

The hydraulic fracture industry started to use aqueous based fluids for fracturing and fluid additives to neutralize clay reactivity with the development of additives such as viscosifier, clay swelling inhibitor and corrosion inhibitors. The improvement in pumping capacity and perforation placement techniques, in addition to the reduced cost of treatment, led to a considerable increase in the efficiency of the fracturing process. (Hassebroek and Waters, 1964)

Massive Hydraulic Fracturing (MHF) became popular in 1970s where up to 1 million gallons of fracturing fluid and 1 million pounds of proppant were used for stimulating tight gas sands.

Pan American Petroleum performed the first MHF treatment in a well in Stephens County, Oklahoma in 1968. In 1973, Amoco introduced MHF to the Wattenberg Gas Field of the Denver Basin of Colorado, in order to extract gas from low permeability sandstone. Wattenberg field was uneconomic prior to MHF introduction. By 1983, nearly 80,000 hydraulic fracture treatments were carried out constituting to 35-40% of drilled wells being hydraulically fractured (Veatch, 1983).

There was a surge of technological advancement in fracturing shale formations in the 1980s leading to the U.S. vastly increasing its oil and especially natural production that continues to this day. In the 1980s, Mitchell Energy & Development Corp. began experimenting with hydraulic fracturing in the wells in Barnett Shale in Texas. Mitchell Energy drilled the first commercial shale well (C. W. Slay No. 1) in 1981. The well was stimulated using crosslinked fluid and 20/40 mesh proppant. Barnett Shale wells continued to be completed with extensive use of MHF treatments with variable production wells (Fischer et al., 2002).

The first slick water frac treatment that involved the use of treated water and very low concentrations of proppant, was successfully implemented in Cotton Valley formation in East Texas in 1995. This resulted in a considerable savings in treatment cost over previously practiced fracturing treatments (Mayerhofer et al., 1997). Mitchell Energy began experimenting with slick water fracs in shale reservoirs after the success in Cotton Valley project. They came up with designed slick water treatments that vastly optimized the productivity and economics of stimulation despite early failures (Fischer et al., 2002)

Hydraulic fracturing has evolved into a technique suitable to stimulate most wells under extremely varying conditions. With various recent technological advancements such as zipper fracs, highway fracturing, simultaneous fracs and monolayer proppant placement strategies,

hydraulic fracturing has enhanced well performance, and recovered otherwise inaccessible resources in majority of U.S. oil and natural gas splays. Despite all the technological advances, reservoirs are typically considered homogeneous and continuous while modelling the hydraulic fracture treatments. Due to inherent anisotropy and presence of natural fractures, shale reservoirs present challenges in accurate modeling and execution of hydraulic fracturing operations; thereby further introduce challenges in mapping them. Growing concerns over environmental damages caused by hydraulic fracturing add to the requirement to model fractures with higher accuracy considering all the complexity of the formation (Groat and Grimshaw, 2012).

2.2 *In-situ* stress in rocks

Hydraulic fracture orientation and geometry are critical to the success of reservoir management to ensure efficient reservoir recovery. The breakdown pressure and fracture orientation are controlled by the prevailing *in-situ* stresses (Hubbert and Willis, 1957). Principally, the breakdown pressure must overcome the *in-situ* stress concentration around the borehole in addition to the tensile strength of the rock for the fracture to occur. At any point, the stress conditions can be represented by the three orthogonal principal stresses: σ_v (vertical or overburden stress), σ_h and σ_H (two horizontal stresses) as shown in Figure 2.2:

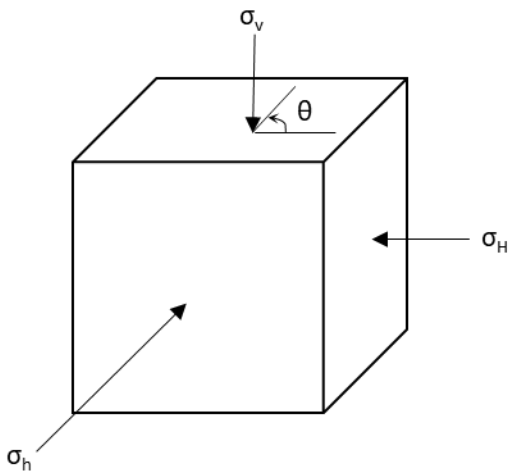

Figure 2.2 Three principal stresses on an element of rock mass at any depth. : σ_v- vertical or overburden stress; σ_h and σ_H - two horizontal stresses

Assuming the borehole to coincide with one of the principal stress directions (σ_v), linear elastic rock behavior and no diffusion of wellbore fluid into the surrounding rock, the stress distribution around the borehole can be expressed as (Timoshenko and Goodier, 1970, and Kirsch, 1898):

$$\sigma_{rr} = P_w \tag{2-1}$$

$$\sigma_{\theta\theta} = (\sigma_h + \sigma_H) - 2(\sigma_h - \sigma_H)cos2\theta - P_w \tag{2-2}$$

$$\tau_{r\theta} = 0 \tag{2-3}$$

where θ is the angle measured counter clockwise with respect to the maximum stress direction (σ_H), σ's denotes the principal stresses mentioned earlier and P_w is the reservoir pressure in the wellbore at the depth under consideration.

At θ = 90°, the hoop stress ($\sigma_{\theta\theta}$) becomes minimum (at r = R):

$$\sigma_{\theta\theta} = 3\sigma_h - \sigma_H - P_w \tag{2-4}$$

The tensile failure tends to initiate perpendicular to the minimum hoop stress ($\sigma_{\theta\theta}$) and consequently the fracture orients along the direction of the maximum principal stress ($\theta = 90^o$). Given that the formation is under a pore pressure, P_o, the tensile failure occurs when the effective pressure ($\sigma_{\theta\theta} - P_o$) at the wellbore reaches the tensile strength (T_o) of the rock (Hubbert and Willis, 1957). Consequently, equation (2-4) becomes:

$$P_b = 3\sigma_h - \sigma_H + T_o - P_o \tag{2-5}$$

$$T_o = P_b - 3\sigma_h + \sigma_h + P_o \tag{2-6}$$

where P_b is the breakdown pressure (upper limit as no fluid diffusion is considered).

The breakdown pressures are lower than calculated by equation (2-5) when we consider the poroelasticity effects (Detournay et al., 1986). The corresponding P_b^1 is:

$$P_b^1 = \frac{3\sigma_h - \sigma_H + T_o - 2\eta P_o}{2(1-\eta)} \tag{2-7}$$

where η is the poroelastic constant (typically 0.25 in value) given by:

$$\eta = \frac{\alpha(1-2\nu)}{2(1-\nu)} \tag{2-8}$$

where ν is the Poisson's ratio of the formation and α is the Biot's coefficient:

$$\alpha = 1 - \frac{K_{dry}}{K_g} \tag{2-9}$$

where K_{dry} and K_g are the dry porous frame and grain bulk modulus of the formation, respectively. For values of α, see Wong et al., 2004.

The diffusion of the fluid into the formation increases the pore pressure that results in lower breakdown pressure.

2.3 Breakdown pressure in a vertical borehole

As already mentioned, hydraulic fracture is initiated when the local minimum principal stress at a position on the wall reaches the tensile strength of the rock (Hubbert and Willis, 1957). In case of vertical borehole, the overburden stress is usually one of the principal stress components and is parallel to the borehole axis. Chitrala (2011) discuss the fracture direction and breakdown pressure for various shallow and deeper wells for vertical borehole. These are summarized in Table 2-1:

Table 2-1 Breakdown pressure and fracture orientation for different vertical well cases (Chitrala, 2011)

Well Depth	Fracture orientation	Breakdown Pressure
<2000 ft.	Horizontal fracture	Equation (2-1)
>2000 ft. (Uncased)	Vertical fracture	Equation (2-4)
>2000 ft. (Cased)	Vertical fracture	Equation (2-5)

2.4 Breakdown pressure in horizontal borehole

Chitrala (2011) discusses the fracture direction and breakdown pressure for horizontal boreholes as summarized below in Table 2-2:

Table 2-2 Upper and lower limits of breakdown pressure and fracture orientation for various horizontal borehole cases (Summarized from Chitrala, 2011)

Stress Configuration	Borehole drilled along σ_h		Borehole drilled along σ_H	
	Breakdown Pressure	Fracture Orientation	Breakdown Pressure	Fracture Orientation
$\sigma_v > \sigma_H > \sigma_h$	$P_b = 3\sigma_H - \sigma_v + T_o - P_o$ $P_b^1 = \frac{3\sigma_H - \sigma_v + T_o + 2\eta P_o}{2(1-\eta)}$	Longitudinal vertical fracture near wellbore reorients into transverse vertical fracture in far field	$P_b = 3\sigma_H - \sigma_v + T_o - P_o$ $P_b^1 = \frac{3\sigma_H - \sigma_v + T_o + 2\eta P_o}{2(1-\eta)}$	Longitudinal vertical fracture near wellbore and in far field
$\sigma_H > \sigma_v > \sigma_h$	$P_b = 3\sigma_v - \sigma_H + T_o - P_o$ $P_b^1 = \frac{3\sigma_v - \sigma_H + T_o + 2\eta P_o}{2(1-\eta)}$	Longitudinal horizontal fracture near wellbore reorients itself into transvers vertical fracture in far field	$P_b = 3\sigma_H - \sigma_v + T_o - P_o$ $P_b^1 = \frac{3\sigma_H - \sigma_v + T_o + 2\eta P_o}{2(1-\eta)}$	Longitudinal vertical fracture near wellbore and in far field

$\sigma_H > \sigma_h > \sigma_v$	$P_b = 3\sigma_V - \sigma_H + T_o - P_o$ $P_b^1 = \frac{3\sigma_H - \sigma_v + T_o + 2\eta P_o}{2(1-\eta)}$	Longitudinal horizontal fracture near wellbore and in far field	$P_b = 3\sigma_H - \sigma_v + T_o - P_o$ $P_b^1 = \frac{3\sigma_H - \sigma_v + T_o + 2\eta P_o}{2(1-\eta)}$	Longitudinal horizontal fracture near wellbore and in far field

The above equations for wellbore breakdown and fracture orientation assume that the rock is elastically isotropic in behavior.

As Hubbert and Willis (1957) have stated that fracture orientation is predominantly dependent on the preexisting stress conditions around the borehole, concluding that it will propagate perpendicular to the minimum principal stress component. As per previous discussions, the borehole orientation defines which local stress component would control the fracture orientation. Three-dimensional mapping of hydraulic fractures become more important in the presence of natural fractures (Zeng, 2002). Several fracture geometry models had been developed such as PKN (Perkins and Kern, 1961) and KGD (Geertsma and De Klerk, 1969) models, that characterize fracture parameters like half length, height and width to assess the success of a hydraulic fracturing job. Smith and Nolte (1981) presented the basis to monitor hydraulic fracture through pressure signatures based on Carter's leak-off model (Carter, 1957). They demonstrated a log-log plot of fracture treating pressure above the closer stress against treating time, that can be used to identify periods of unrestricted extension, confined height, excessive height growth and restricted penetration. Mapping the fracture geometry and orientation is critical to the success of hydraulic fracturing. However, despite various advanced modeling techniques, there is large uncertainty associated with the complexity of fractures introduced by the local formation heterogeneities such as preexisting fractures. This uncertainty necessitates modeling fractures to ascertain the fracture dimensions and orientation which can then be used to improvise future treatments in the same formation.

2.5 Hydraulic fracture diagnostic techniques

A good comparative study of the various hydraulic fracture diagnostic techniques was summarized by Cipolla and Wright (2000). They classified the techniques into three broad groups. The techniques mentioned are listed in Table 2-3 along with the advantages and limitations of each method.

Table 2-3 Fracture Diagnostic Techniques capabilities and limitations (modified from Cipolla and Wright, 2000)

Techniques: **Can Determine** **May Determine** **Cannot Determine**

Group	Diagnostic	Main Limitations	Ability to Estimate							
			Length	Height	Asymmetry	Width	Azimuth	Dip	Volume	Conductivity
Direct, Far Field	**Surface Tilt Fracture Mapping**	• Cannot resolve individual fracture dimensions from surface tiltmeter fracture mapping. • Mapping resolution decreases with depth (fracture azimuth ± 3° @3000 ft. depth and ± 10° @ 10000 ft. depth								
	Downhole Tilt Fracture Mapping	• Resolution in fracture length and height decreases as offset well distances increases • "Big Picture" fracture growth; NOT "small details". • No information about proppant distribution and effective or productive fracture geometry.								
	Microseismic Fracture Mapping	• Individual fracture planes cannot be resolved. • Adequate signal-to-noise ratio limits offset well distance within 1500 ft. of fractured well. • Microseisms may not be generated in all formation types, e.g.: in anisotropic formation • No information about proppant distribution and effective or productive fracture geometry.								
Direct,	**Radioactive Tracers**	• Depth of investigation only about 1-2 ft. away from the fractured well.								

		• Provides only lower bound for fracture height if fracture and well-path are not aligned.								
	Temperature Logging	• Thermal conductivity of different formations can vary, skewing temperature log results. • Post-treatment log requires multiple passes very soon (within 24 hrs.) after the treatment skewing temperature log results. • Provides only lower bound for fracture height if fracture and well-path are not aligned.								
	Production Logging	• Provides only information about zones/perforations contributing to production in cased hole applications.								
	Borehole Image Logging	• Only run in open hole. • Provides fracture orientation near wellbore only.								
	Downhole Video	• Runs mostly in cased holes and provides only information about zones/perforations contributing to production (may have open hole applications).								
	Caliper Logging	• Only run in open hole. • Formation wash outs skew interpretations.								
	Electro-magnetic induction	• Very costly • Dependent on effective placement of electrically conductive proppant with the generated fractures								
Indirect	**Net Pressure Fracture Analysis**	• Results depend on model assumptions and reservoir description. • Requires "calibration" with direct observations.								
	Well Testing	• Results dependent on model assumptions • Requires accurate permeability and reservoir pressure estimates and "calibration".								
	Production Analysis	• Results dependent on model assumptions. • Requires accurate permeability and reservoir pressure estimates and "calibration".								

Real time monitoring of hydraulic fracture growth has made microseismics a popular choice in hydraulic fracture mapping in field. However, there are shortcomings to this method, it cannot be repeated and has poor results in anisotropic formations. In this study, a new approach

utilizing the shear birefringence phenomenon is proposed to map hydraulic fracture in not only isotropic mediums such as tight sandstones but also in highly anisotropic mediums such as pyrophyllite. Comparative study is presented for both microseismic data and shear wave acquisition in the subsequent sections.

2.6 Microseismicity

During hydraulic fracturing stimulation, the stress-induced deformations on pre-existing rock structures or a fracture network releases short duration of acoustic wave emissions, that can be recorded, that are recorded by pre-positioned seismic detectors, namely geophones; these are referred to as microseisms. The emission can be felt in some cases as small as the moment magnitude of an earthquake (-1 to -3). The detected waves can be processed to form images of spatial distribution of hypocenters that aid in real time monitoring of the hydraulic fracture propagation. It reveals the fracture propagation pattern.

The release of energy due to rock failure, as detected by geophones, can be quantified as a convolution of displacement recorded at the seismogram; it is a function of the seismic source, the rock structure and the seismometer, as stated in equation

$$u(t) = x(t)q(t)r(t) \tag{2-10}$$

where $x(t)$ is the source displacement-time function, $q(t)$ is the effect of the rock structure and $r(t)$ is the response of the detecting instrument (Stein and Wysession, 2003). The above expression is Fourier transformed to the frequency domain and can be expressed as equation

$$U(\omega) = X(\omega)Q(\omega)R(\omega) \tag{2-11}$$

where ω is the frequency and $X(\omega), Q(\omega), and\ R(\omega)$ are the corresponding Fourier transformed functions.

The microseisms are detected by placing the geophones at the surface or in a wellbore. The size of these events can be quantified by the seismic moment (M_o):

$$M_o = \mu AD \tag{2-12}$$

where μ is the shear modulus of the rock, A is the source area of the geologic fault where the rupture occurs, and D is the average displacement on A. Moment is generally expressed as log of the seismic moment and ranges from -4 to -1 for microseismic events. For a detectable earthquake, the moment should at least be -3 (Maxwell and Warpinski, 2006).

2.7 Wave Propagation

Shear wave split into two orthogonal phase components displaying different velocities as it propagates through an anisotropic medium. In oil industry, the two components are called S_s and S_f, or slow and fast shear wave, respectively. Slowness difference between the component depends on the extent of anisotropy in the rock. This is among the most direct and unambiguous indicator of seismic anisotropy. (Crampin, 1984; Teanby et al., 2004)

In contrast, P-waves or compressional wave are elastic body waves in which the motion of the particles is in the direction of the wave propagation. They are called primary waves because they arrive before shear waves. (Figure 2.3)

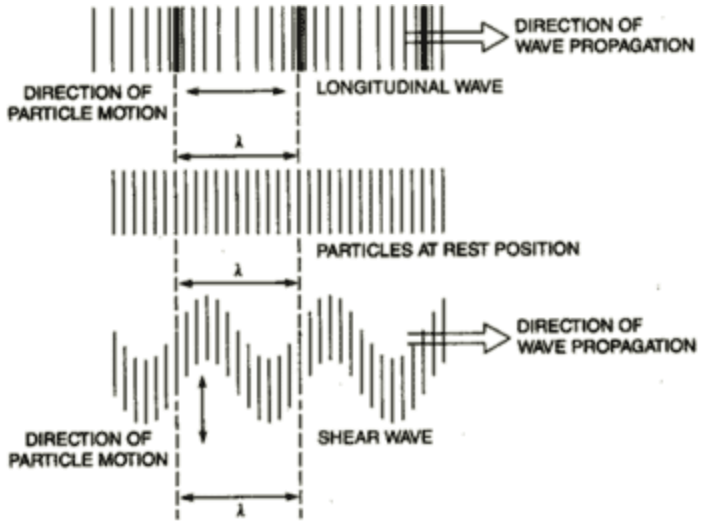

Figure 2.3 P-wave and S-wave propagation (NDT Resource Center, 2017)

The wave motion mentioned above is not a travelling wave but is simple harmonic oscillations about equilibrium positions.

The sensitivity of the seismic wave propagation to cracks and fractures is one of the fundamental observations of rock physics. Cracks and fractures:

- Decrease P- and S- wave velocity,
- Increase velocity dispersion and wave attenuation,
- Increase pressure-dependence of velocity,
- Increase velocity and attenuation,

The potential to map cracks and fractures is to exploit these many different seismic signatures of fractures. Seismic P- and S- waves tend to be "affected" by presence of fractures or cracks when their direction of propagation or their direction of polarization is at an angle to the fracture faces (Figure 2.4) (Nur et al., 1969; Rai and Hanson, 1988). Pressure-dependent anisotropy is a key indicator of fractures.

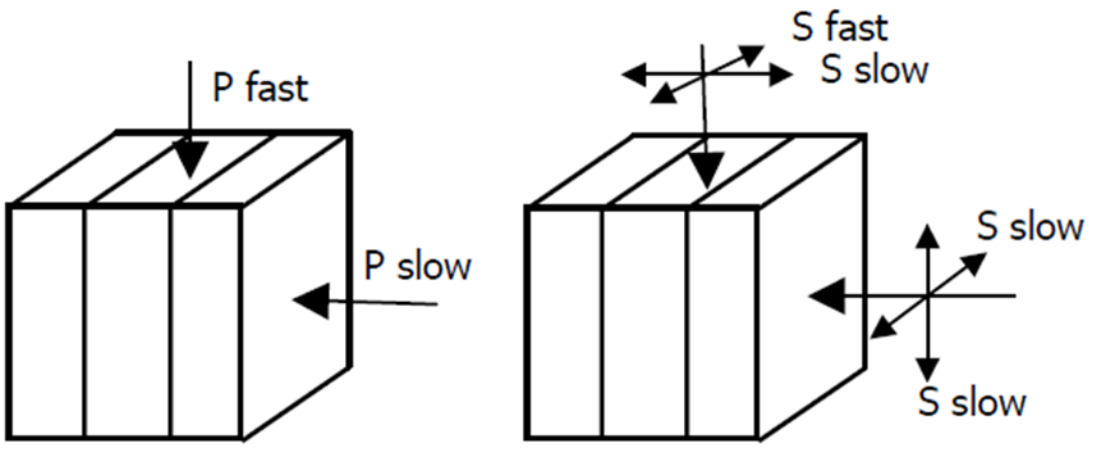

Figure 2.4 Schematic showing P-wave and S-wave propagation through a laminated medium

P-waves are also "affected" by fractures; however, vertically propagating P-waves will not be very sensitive to vertical fractures. S-waves on the other hand have sensitivity to fractures in both horizontal and vertical direction due to their polarization property. Vertically propagating shear waves that are polarized parallel to the fracture planes will travel faster than shear waves polarized perpendicular to the fracture planes. The splitting of incident shear wave on any medium at arbitrary polarization into two modes, fast and slow shear wave, is known as wave splitting. Splitting property of shear waves is not only sensitive to the fracture geometry but also on the fracture orientation, stress and mineralogy. The sensitivity of shear birefringence to fractures is utilized in this study to map hydraulic fracture and its geometry.

2.8 Transversely Isotropic Media

Transverse isotropy is a special case of orthorhombic symmetry with a horizontal plane of symmetry (Tsvankin and Grechka, 2011). They are characterized by an axis of symmetry that is normal to the plane of symmetry.

Horizontally layered shale formations are represented using Vertical Transverse models (VTI) (Figure 2.5 (a)). Wave propagation in VTI medium is governed by the Thomsen's parameter

(as discussed in section 3.1.3(b)) (Thomsen, 1986). Shear wave split into horizontal and vertical polarization phases in the VTI medium (Crampin and Love, 1991).

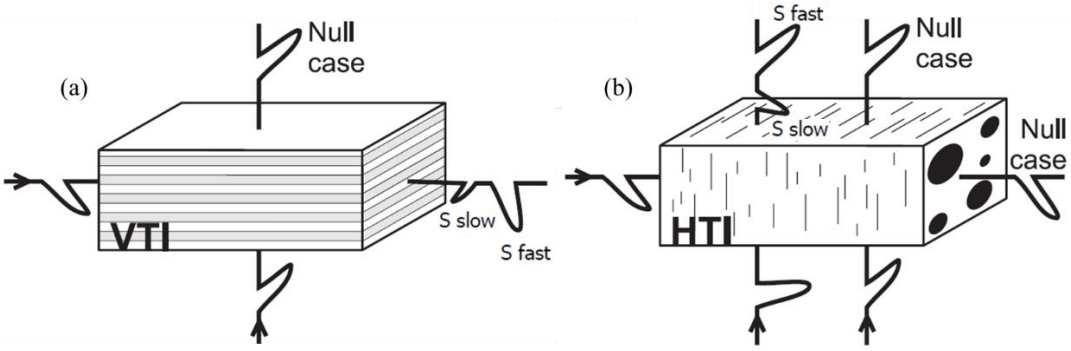

Figure 2.5 Shear wave propagation in VTI medium: vertically travelling shear wave propagates normal to the isotropy plane representing a null case, horizontally travelling shear wave gets polarized with a difference in velocity of the two polarization. (b) Shear wave propagation in HTI medium: horizontally travelling shear wave is the null case here, vertically travelling shear wave is split into slow and fast shear waves with fast shear wave polarized parallel to the fracture (isotropy) plane. (modified from Wuestefeld et al., 2010)

Horizontal Transverse Isotropy (HTI) model on the other hand consist of a single set of azimuthally invariant vertical fractures with an isotropic background (Figure 2.5 (b)). Wave propagation in the HTI medium is governed by the anisotropy parameters developed by Tsvankin (1997).

2.9 Historical development of Shear Wave technique

Velocity anisotropy and shear birefringence are well documented by Waterman and Teutonico, 1957; Verma, 1960 and Simmons and Wang, 1971. There has always been an interest concerning velocity anisotropy in rocks, primarily studies related to earthquake prediction, as reported by Nur and Simmons, 1969; Christensen and Ramananantoandro, 1971; Gupta, 1973; Tilmann and Bennett, 1973; Todd et al., 1973 and Bonner, 1974.

Keith and Crampin (1977), and Crampin (1978, 1981) made the insights into the behavior of shear waves in anisotropic media. Crampin (1977) showed that in an anisotropic medium with simple symmetry (hexagonal, orthorhombic), shear wave splits into orthogonal particle motion moving at different speeds. It was observed that one component propagates with a relatively fast velocity compared to the other component and its polarization defines the apparent fast-axis of the medium. The other slow component is polarized orthogonal to the apparent fast-axis.

There have been encouraging experimental *in-situ* observations by Cox et al., 1989 and through theoretical and experimental lab studies in the rock physics domain (Hudson, 1981; Schoenberg, 1983; Rai and Hanson, 1988; Rathore et al., 1991). The possibility of an anisotropic structure is apparent from the two components of the split shear wave (Savage 1999; Levin 1999; Hartog and Schwartz 2000; Rai and Sondergeld 1992).

In addition to the above laboratory studies, there have been actual field experiments in which the anisotropy in seismic wave propagation has been observed associated with fracturing: Multicomponent-multisource shear data acquired by Alford (1986) at Dilley, Texas, were severely distorted due to shear polarization resulting from propagation through an azimuthally anisotropic medium.

Sondergeld and Rai (1992) studied shear birefringence by propagating shear wave along a fixed direction, with polarization parallel or perpendicular to a principal direction. The velocity of the wave would be the faster component when the transmitter polarization is aligned parallel to the elastic fabric and is slow when it is perpendicular. Such azimuthal anisotropy can be observed by polarized shear wave propagation.

Shear wave splitting has been observed in vertical seismic profiling as well as shown by Gal'perin (1977), Robertson and Corrigan (1983), Winterstein et al. (1995) and Winterstein et al. (2001). Most of the published studies have assumed that the azimuthal directions with respect to the shear wave polarizations are independent of distance and depth along the seismic profile. The issue is the signal to noise ratio is generally poor in shear-wave surface seismic data. It is possible to correct for the shear wave birefringence in the first layer though. Such correction was done by Winterstein and Meadows (1991a and b) in VSPs and by Garotta and Granger (1988) in surface seismic profiles with P to S converted waves. However, since VSPs inherently provide shear wave data at various depths, recognizing more than two birefringent layers through shear wave splitting were preferred over surface seismic profiles (Crampin et al., 1986).

2.10 Laboratory Hydraulic fracturing experiments

Haimson and Fairhurst (1969) experimented on hydraulic fracturing breakdown pressures on porous and permeable hydrostone samples cured with different water-to-hydrostone ratios under triaxial loading. The effect of tectonic stress was observed on the fracture orientation in the study. The observed breakdown pressure was lower than the theoretical value for impermeable rocks while it was observed to be higher for permeable rocks. An inverse relation was observed between borehole diameter and the breakdown pressures. For larger boreholes, breakdown pressures were lower and with higher pressurization rates, the breakdown pressure increased. A similar study by Zoback et al., (1977) on cylindrical rock samples under triaxial stress conditions confirmed that breakdown pressure is indeed dependent on wellbore pressurization rate. They also concluded that fracture propagates in the direction perpendicular to minimum stress.

Daneshy (1973) investigate the effect of inclined wellbore on hydraulic fracturing. He concluded that the fracture would not follow the direction perpendicular to the minimum stress but as it propagates away from the wellbore it will reorient itself perpendicular to the minimum stress. His results were based on triaxial experiments conducted on three sets of rocks (Carthage limestone, Indiana limestone and Hydrostone) with wellbores drilled at various angles to the direction of the applied stress.

Cheung and Haimon (1987) studied the effect of hydraulic fracture propagation and orientation in presence of pre-existing fractures. The experiment was conducted on 4.9 in. x 4.9 in. x 6.7 in. blocks of Niagara dolomite under triaxial stress condition. It was observed that the induced fractures opened up perpendicular to the direction of minimum stress.

Guo et al. (1993 a, b) performed laboratory experiments on gypsum blocks in triaxial stress condition to investigate the behavior of breakdown pressure on varying stress state as well as varying injection rate on fracture characteristics. They observed that as the principal stress decreased, the fracture propagation was faster and wider and longer fractures were induced. However, they also observed that the breakdown pressure did not have any correlation with the conventional tensile fracture theory and that the tensile strength was considerably higher than the experimental value from Brazilian test.

Morita et al. (1996) carried out hydraulic fracturing experiments on Berea sandstone, Castlegate sandstone and Mancos shale to investigate the effect of high solid and solids free drilling fluids on hydraulic fracture. The results showed unstable fracture growth once the drilling fluid enters after the fracture initiation. The fracture growth took place in three different zones: non-invaded zone, mud dehydrated zone and fracture zone. The breakdown pressure

appeared to have strong dependence on factors such as Young's modulus, borehole size and the drilling fluid type.

2.11 Shear wave birefringence to evaluate fracture and crack

There have been few attempts to characterize natural fractures as well as cracks using shear wave birefringence at the field scale. Most of them have been on Vertical Seismic Profile (VSP) data recording. Some of the contributions in evaluating fractures and crack using S-wave are discussed as below:

Tatham et al. (1987) conducted physical model experiments on 16 plexiglass assembly to identify the fracture intensities in the stack. The plates were assembled under water and the gaps between the plexiglasses had thin layers of water to avoid the formation of effective welding between the surfaces. The system acts as a fractured system and shear wave arrivals are observed through the stack for polarizations parallel, perpendicular and at arbitrary angle to the sheets. Tests were carried out on different thicknesses of plexiglass to study the effect of varying number of fractures per wavelength.

Crampin et al. (1989) studied the shear wave splitting in the VSP field data recorded in Austin Chalk reservoir in Texas, Niobrara Chalk reservoir in Wyoming and other areas in US. Shear wave splitting was identified on surface recordings in many of these areas. They observed accurate estimates of crack orientations ($\pm 30^{o}$), crack density ($\pm 5\%$), and aspect ratio (± 0.1) using synthetic seismogram modelling with shear wave VSP data.

Mueller (1991) used a multicomponent multisource shear wave interpretation to predict intensely fractured intervals in the Austin Chalk for a horizontal drilling program. The method involves interpreting the anomalies in the slow shear polarization amplitude data to identify

the fracture growth using Alford rotation technique (Alford, 1986a). Slower shear polarization data was considered more representative of the fracture intensity while the fast shear arrivals were more lithology dependent. A test drill based on two of the fracture intensity calculation on slow shear polarization data yielded significantly higher production than the surrounding wells.

Winterstein and Meadows (1995) presented the results of using VSP method involving shear wave source at the surface and downhole three-component geophones to record shear wave arrivals predominantly along the vertical path to evaluate fracture alignment and intensity. They analyzed the shear birefringence using Alford (1986a) rotation technique to map the inherent fracture geometry by rotating the source-receiver array. They presented data from VSP carried out at Lost Hills Well, San Andreas in Texas, and few other areas in south Texas. Data from the Lost Hills well show clear evidence of fast shear wave polarization direction corresponding to the maximum horizontal stress direction. Winterstein et al. (2001) also present shear wave birefringence data from VSPs carried out in the western half of North America, mainly focusing on Texas and the south wester San Joaquin Basin of California. Interpretation of the S-wave VSP data agreed well with the crossed-dipole data, fracture images and wellbore breakouts.

2.12 Fast Fourier Transform (FFT)

De Figueiredo et al. (2013) studied the velocity and dependence of shear wave frequency in a fractured anisotropic media. They introduced cracks in 10 layers and 17 layers in two samples and measured the shear wave splitting by changing the source frequency. They used FFT to analyze the recorded waveform in the frequency domain to demonstrate the effect of elastic scattering, attenuation, velocity dispersion and crack size in shear wave splitting. The analysis

showed for higher frequencies (of the order of few hundred kHz) produced less shear wave splitting. Low pass filtering of high frequency data revealed small shear wave splitting more effectively. This splitting was higher for larger cracks with smaller density.

3 EXPERIMENTAL METHODOLOGY

3.1 Sample Characterization

3.1.1 Circumferential Velocity Analysis

Circumferential Velocity Analysis (CVA) is the measurement of P-wave velocity across the circumference of the cylindrical sample at different azimuths. The variation in the P-wave velocity along the circumference of the sample gives the magnitude and direction of the P-wave velocity anisotropy in the horizontal plane perpendicular to the axis of the cylinder; it can be useful in estimating the direction of cracks or discontinuities inherent in the rock samples. The CVA measurement were taken using the apparatus setup shown in Figure 3.1.

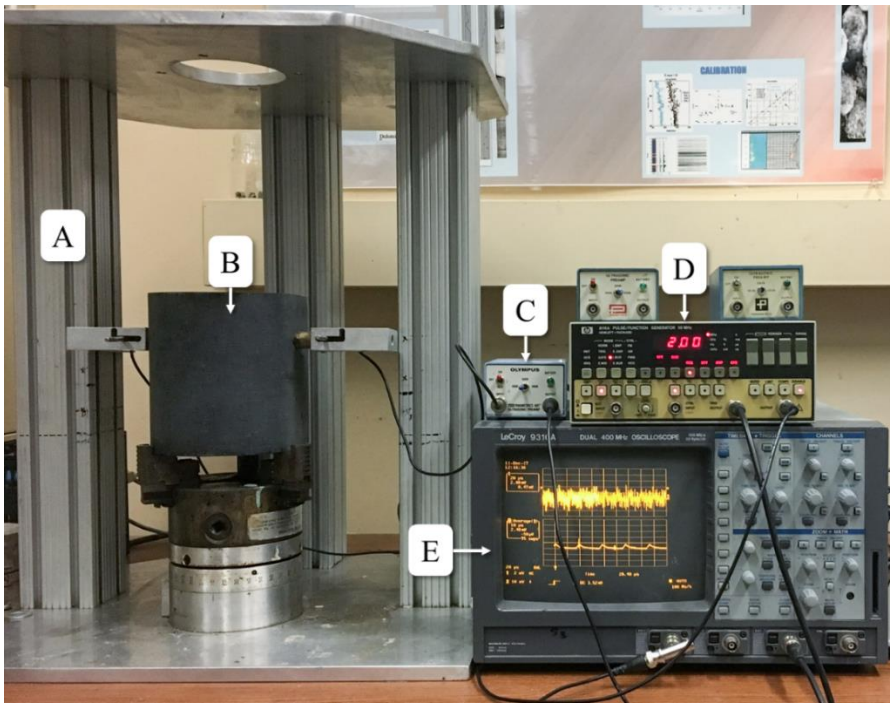

Figure 3.1 Circumferential Velocity Analysis experimental setup. (A) stand with mounted transducers (B) rock sample (C) preamplifier (D) signal generator (E) digital oscilloscope

The rock sample is secured firmly to a 3-jaw rotatable base with a pair of diametrically opposed P-wave transducers mounted on machined brass coupling plates that are in contact with the

cylindrical face of the sample. The base has the flexibility to rotate at a desired angle operated by a digitally controlled electric motor. The signal generator produces a voltage pulse (16 V) generating a P-wave signal of the desired frequency and amplitude, that is transmitted through the sample amplified and fed to a digital oscilloscope where the P-wave arrival signal is picked. The received signal was stacked over 200 times to improve the signal to noise ratio. The first arrival travel time is picked after removing the transducer delay in the brass coupling fixtures. Readings were taken at every 10^{o} with a total of 36 readings around the sample and digitally stored. The procedure was repeated at seven different heights along the length of the sample.

CVA was carried out for the Tennessee sandstone and pyrophyllite samples. The Tennessee sandstone sample was vertical core and pyrophyllite samples were horizontal cores. The results of the CVA are plotted in Figure 3.2 through Figure 3.4. Pyrophyllite samples show a large variation in the P-wave velocity with azimuth while sandstone show very little variation in velocity with azimuth. Strong anisotropic nature of pyrophyllite ($\approx$20%) is reflected by sinusoidal pattern in the P-wave velocity.

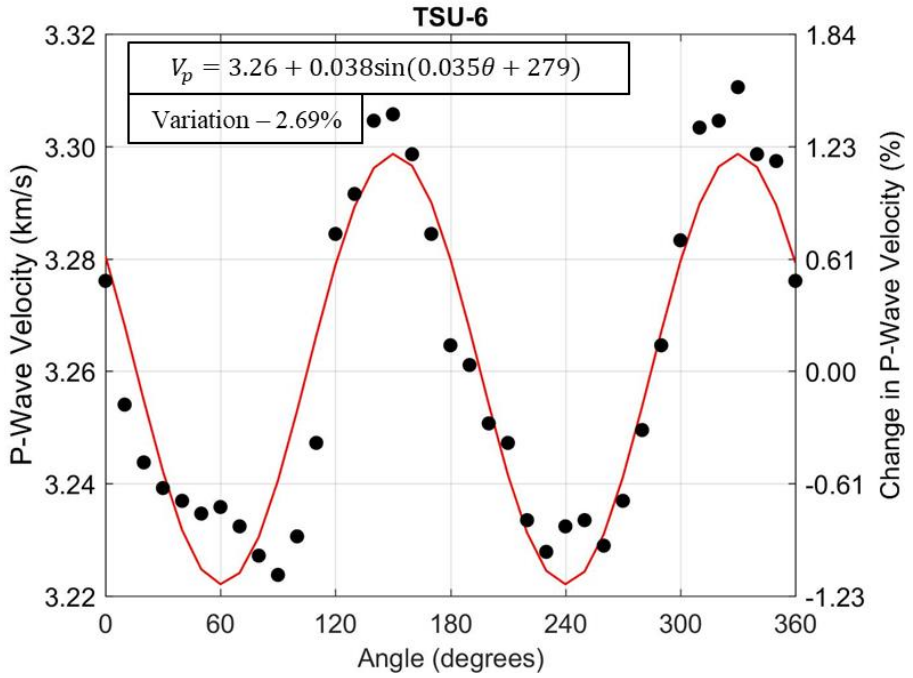

Figure 3.2 Azimuthal distribution of P-wave velocity in Tennessee sandstone sample TSU-6 using CVA. Mean velocity = 3.26 km/s

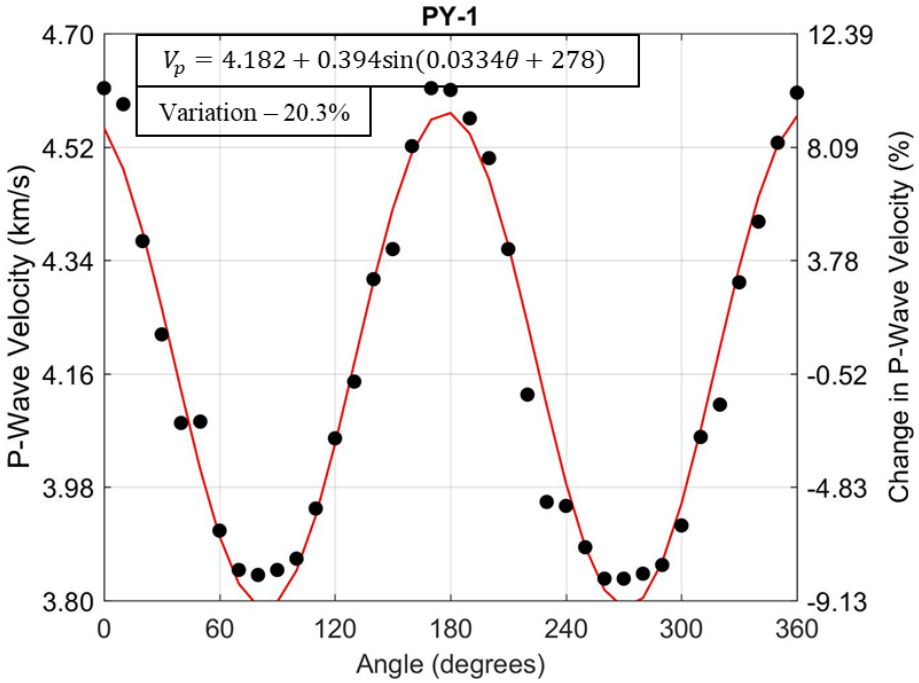

Figure 3.3 Azimuthal distribution of P-wave velocity in pyrophyllite sample PY-1 using CVA. Mean velocity = 4.182 km/s

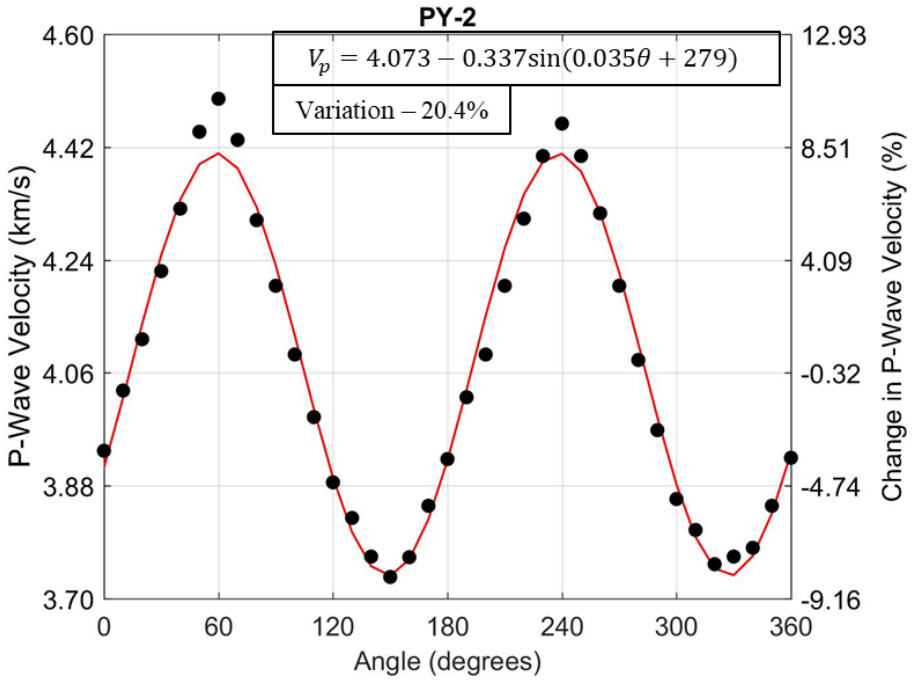

Figure 3.4 Azimuthal distribution of P-wave velocity in pyrophyllite sample PY-2 using CVA. Mean velocity = 4.073 km/s

The sinusoidal variation of velocity with angle is curve fitted with the form of:

$$v(\theta) = A + Bsin(C\theta + D) \qquad (3\text{-}1)$$

where $v(\theta)$ is the P-wave velocity at an angle θ, A is the mean velocity, B is the maximum variation of the sinusoid from its mean, C is inversely related to the period of the sinusoid, and D is the initial phase of the sinusoid. The direction of the highest velocity coincides with the direction of the foliation of the pyrophyllite sample. The variation in sandstone is very small and hence considered isotropic in nature.

3.1.2 Plug Porosity and Permeability measurement

Porosity and permeability of Tennessee sandstone was measure using Core Test AP-608™ permeameter. The permeameter uses Boyle's Law to calculate the porosity. In addition, helium plug porosity is measured independently. Detailed descriptions about helium and AP-608™ measurements are discussed in Kale (2009). The porosity and permeability values of the

Tennessee sandstone sample are shown in Table 3-1. Crushed porosity measurement is higher than plug porosity values since crushed measurements get accessibility to inaccessible pore volume compared to the plug measurements that measures the effective porosity.

Table 3-1 Porosity and permeability values of Tennessee sandstone sample measured using AP608™ and LPP. (Values reported are for 500 psi and 4000 psi confining pressure)

Sample no.	AP608 ϕ (%) (500-4000 psi)	AP608 K (μd) (500-4000 psi)	ϕ_{He} (%)
TSU-6	4.7-4.3	27-7	9.7

3.1.3 Elastic Properties measurement

(a) Tennessee Sandstone

Elastic properties of isotropic material can be defined by two independent elastic constants. As per the CVA data of Tennessee sandstone, the rock material is considered isotropic. The P and S velocity are measured at different confining pressure using native Tennessee sandstone cores. The elastic constants are calculated using the following:

$$K = \rho\left(v_p^2 - \frac{4}{3}v_s^2\right) \tag{3-2}$$

$$G = \rho v_s^2 \tag{3-3}$$

$$v = \frac{\frac{1}{2}\left(\frac{v_p}{v_s}\right)^2 - 1}{\left(\frac{v_p}{v_s}\right)^2 - 1} \tag{3-4}$$

$$E = 2G(1 + v) \tag{3-5}$$

where v_p and v_s are the P-wave velocity and S-wave velocity respectively, K is the bulk modulus, G is the shear modulus, v is the Poisson's ratio and E is the Young's modulus of the isotropic rock.

(b) Pyrophyllite

The CVA data on pyrophyllite samples show the anisotropic nature of the rock material. Pyrophyllite is a fine grained monomineralic metamorphic rock comprised of the mineral pyrophyllite, a member of the illite family, an analogy to natural shale. The anisotropic nature of pyrophyllite is due to preferred orientation of the anisotropic mineral grains. A simplistic model for anisotropy is transverse isotropy model with an axis of symmetry perpendicular to the bedding plane and can be characterized by measuring 5 independent elastic properties. As per Thomsen (1986), most rock material exhibit transverse isotropy that can be modelled based on simplified approximation for weak anisotropy. This model uses three anisotropic parameters (ε, γ and δ) and 2 velocities that depend on 5 independent parameters (C_{11}, C_{13}, C_{33}, C_{44}, and C_{66})

$$\varepsilon = \frac{C_{11} - C_{33}}{2C_{33}} \tag{3-6}$$

$$\gamma = \frac{C_{66} - C_{44}}{2C_{44}} \tag{3-7}$$

$$\delta = \frac{(C_{13} + C_{44})^2 - (C_{33} - C_{44})^2}{2C_{33}(C_{33} - C_{44})} \tag{3-8}$$

In contrast to initial belief that shales exhibit weak anisotropy with ε and γ < 10%, it has been observed by Sondergeld and Rai (2011a) that they are of the range of 60% in most cases. This severely limits the use of Thomsen's approach to quantify phase velocities. Berryman (2008) proposed equations to model phase velocities in strong transverse isotropy. The values of P- and S-wave velocities, as per Berryman's (2002) work is given by:

$$V_p(\theta) = V_p(0)\left(1 + \varepsilon \sin^2\theta + (\epsilon - \delta)\frac{2\sin^2\theta_m \sin^2\theta \cos^2\theta}{1 - \cos 2\theta_m \cos 2\theta}\right) \tag{3-9}$$

$$V_{sv}(\theta) = V_s(0)\left(1 + \frac{v_p(0)^2}{v_s(0)^2}(\epsilon - \delta)\frac{sin^2\,\theta_m\,sin^2\,\theta\,cos^2\,\theta}{1 - cos\,2\theta_m\,cos\,2\theta}\right) \quad (3\text{-}10)$$

where θ_m is the angle when V_{sv} is maximum given by:

$$tan^2\,\theta_m = \frac{C_{33} - C_{44}}{C_{11} - C_{44}} \quad (3\text{-}11)$$

Berryman's formulation extends Thomsen's weak anisotropy model to stronger deviation from isotropy, without affecting the equation's simplicity significantly. The extreme value of V_{sv} is calculated at the correct specified incidence angle θ instead of it always being at $\theta = 45^o$. Wave speed magnitudes are more closely approximated for the incidence angles. Furthermore, $\theta = \theta_m$ (close to the extreme value of V_{sv}) can be deducted for weak anisotropy data analysis as well.

(c) Three Plug Technique

The classical three plug technique to measure anisotropy was summarized by Wang (2002). Three plugs are cored at 0^o, 90^o, and 45^o to the symmetry of the axis as shown in Figure 3.5:

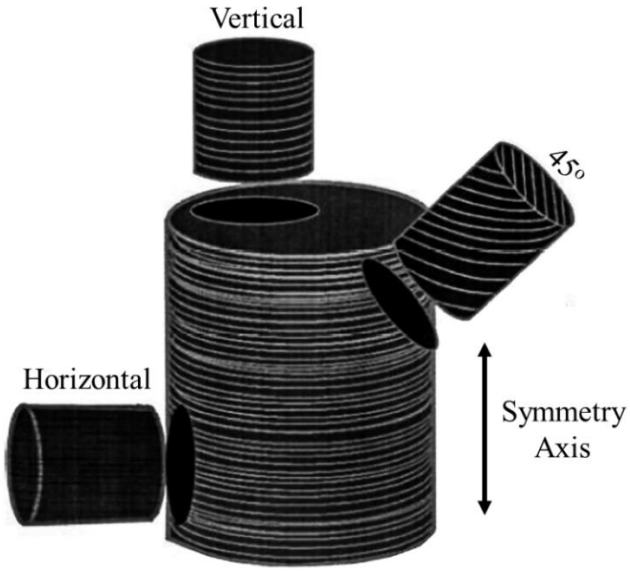

Figure 3.5 Three plug technique to measure transverse isotropy (Wang, 2002)

The P- and S- velocities (V_{s1} and V_{s2} are the shear velocities polarized parallel and perpendicular to the anisotropy symmetry axis; θ is the angle between the core axis and the symmetry axis) are given by the following equations:

$$V_p(\theta) = \sqrt{\frac{A+B}{2\rho}} \tag{3-12}$$

$$V_{s1}(\theta) = \sqrt{\frac{A-B}{2\rho}} \tag{3-13}$$

$$V_{s2}(\theta) = \sqrt{\frac{C_{66}\,sin^2\,\theta + C_{44}\,cos^2\,\theta}{\rho}} \tag{3-14}$$

$$where\ A = C_{11}\,sin^2\,\theta + C_{44} + C_{33}\,cos^2\,\theta \tag{3-15}$$

$$B = \sqrt{[(C_{11}-C_{44})\,sin^2\,\theta - (C_{33}-C_{44})\,cos^2\,\theta]^2 + 4(C_{13}+C_{44})^2\,sin^2\theta\,cos^2\,\theta} \tag{3-16}$$

For θ = 0^o (Vertical plug),

$$V_{p,0} = \sqrt{\frac{C_{33}}{\rho}} \tag{3-17}$$

$$V_{s,0} = V_{s1,0} = V_{s2,0} = \sqrt{\frac{C_{44}}{\rho}} \tag{3-18}$$

For θ = 90^o (Horizontal plug),

$$V_{p,90} = \sqrt{\frac{C_{11}}{\rho}} \tag{3-19}$$

$$V_{s1,90} = \sqrt{\frac{C_{44}}{\rho}} \tag{3-20}$$

$$V_{s2,90} = \sqrt{\frac{C_{66}}{\rho}} \tag{3-21}$$

Using the plugs in the three orientations – 0^o, 90^o, and 45^o, the 5 elastic parameters C_{11}, C_{13}, C_{33}, C_{44}, C_{66} are calculated, assuming transverse isotropy. The three anisotropic constants, $\varepsilon, \gamma, \delta$ are calculated using equations (3-9) and (3-10) subsequently to calculate the three velocities (V_p, V_{sh} and V_{sv}) at any angle θ.

The calculated values of the three anisotropic parameters for pyrophyllite are listed in Table 3-2:

Table 3-2 Anisotropic constants for pyrophyllite

ε	γ	δ
0.183	0.072	-0.004

3.1.1 Minerology Measurement

Fourier Transform Infrared Spectroscopy (FTIR) is used to determine the mineral composition of Tennessee sandstone. FTIR technique is a method to identify minerals in sedimentary rocks by comparing the measured transmission spectra with a library of known mineral spectra

(Sondergeld and Rai, 1993). More details on FTIR are described by Ballard (2007). Herron and Herron (2016) claim to identify 56 minerals using FTIR. Our implementation of FTIR can identify and quantify 16 different commonly found minerals in sedimentary rocks, namely, quartz, calcite, dolomite, smectite, chlorite, illite, kaolinite, pyrite, oligoclase, orthoclase, albite, anhydrite, siderite, mixed clay, apatite and aragonite. The mineral composition of the Tennessee sandstone samples used in this experiment is listed in Table 3-3.

Tennessee sandstone is seen to have on an average 90% quartz and minor amount of mixed clays.

Table 3-3 Mineral composition of Tennessee sandstone measured using FTIR

Mineral	**Tennessee sandstone**
	TSU-6
Quartz	89
Mixed Clay	11

3.2 Equipment and materials for hydraulic fracturing

The experimental configuration consists of two setups: One for recording the acoustic events during the hydraulic fracturing and the other one to make the polarized shear wave survey of the fractured core. Figure 3.6 shows the experimental setup used to conduct the hydraulic fracturing process including the acoustic monitoring system.

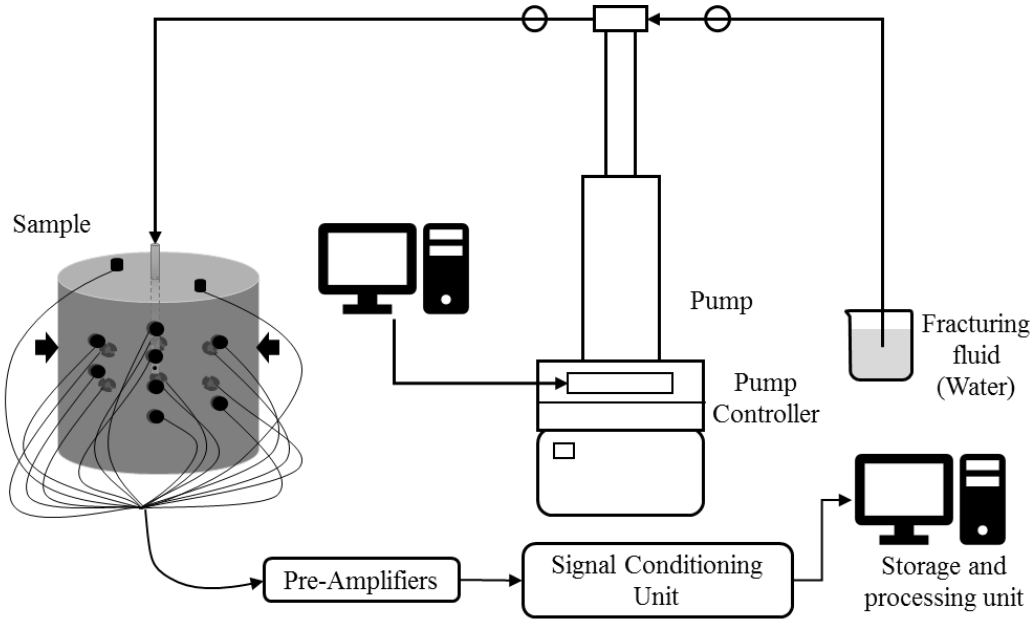

Figure 3.6 Schematic of the complete experimental setup for hydraulic fracturing and acoustic monitoring system

The setup consists of four sub systems: (1) uniaxial loading system (2) pumping unit (3) fluid system and (4) acoustic monitoring system.

3.2.1 Uniaxial Loading System

The uniaxial loading system is custom designed to allow uniaxial loading of rock samples along with simultaneous injection of fracturing fluid and recording of the acoustic events. Stress is applied in the desired direction using a manually operated Enerpac pump that applies stress through a pair of pistons across the sample as shown in Figure 3.7 below:

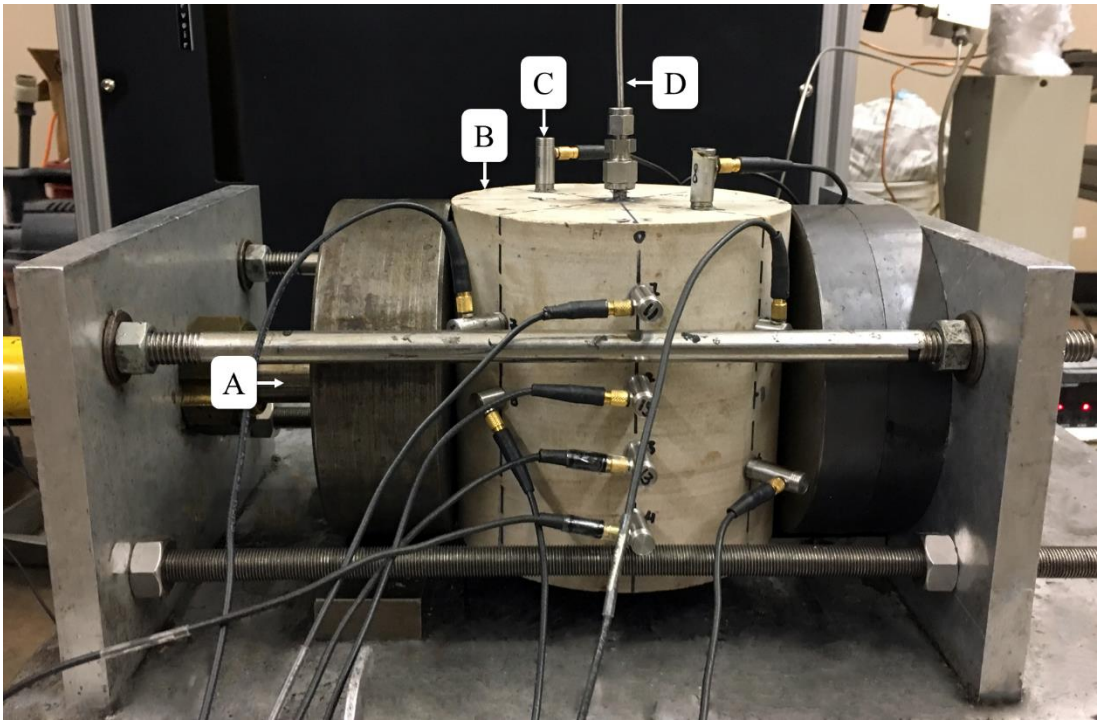

Figure 3.7 Shows components used in the experiment (A) uniaxial loading piston; (B) rock sample; (C) P-wave acoustic transducers; (D) fracturing fluid inlet

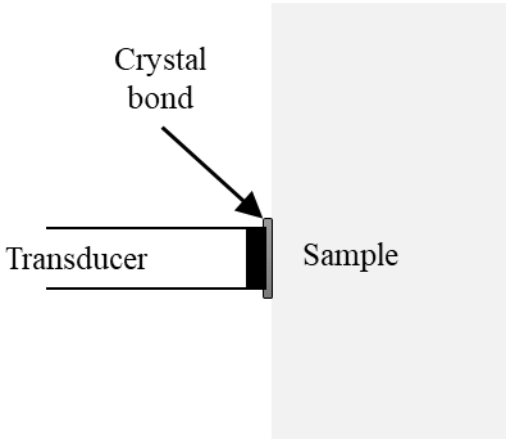

Figure 3.8 Schematic of transducer mounted on rock sample

16 piezoelectric B1025 compressional wave transducers (discussed in Section 3.2.4) were mounted on the rock sample as shown in the Figure 3.7 and Figure 3.8. The transducers are bonded to the rock surface using crystal bond as shown in Figure 3.8. Fracturing injection fluid was pumped through the inlet line and the pressure was observed in the pumping unit.

3.2.2 Pumping Unit

Teledyne Isco 100DX^{TM} pumps were used to inject fracturing fluid into the sample. The pumping system has a maximum pressure rating of 10,000 psi and has a maximum flow rate of 50 ml/min. The cylinder has a maximum capacity of 103 ml with a displacement resolution of 9.65 nanolitres/step. The pump setup is shown in Figure 3.9.

Figure 3.9 Teledyne Isco^{TM} hydraulic pump: (A) pump controller; (B) inlet line; (C) outlet line

3.2.3 Fluid System

The fracturing fluids used for the experiment are distilled water (μ=0.89 cP) and vegetable oil (μ =50 cP). The fracturing fluid is mixed with black dye to highlight fracture visibility on the surface.

3.2.4 Acoustic Emission Monitoring System

(a) Transducer

Each transducer assembly consists of piezoelectric crystals that are mounted on a flat brass coupling plate. Although the sides of the cylindrical core are curved surfaces, the radius of curvature is high enough to allow face of the transducer to adhere properly with the sample. Figure 3.10 shows the image of the transducer assembly. The transducers are small (0.365-inch in diameter, 1-inch in length and 0.25-inch diameter of the piezoelectric crystals). The sensors are 1 MHz B1025 piezoelectric compressional sensors, manufactured by Digital Wave^{TM} Corp. The sensor is designed for a frequency range of 50 kHz to 2 MHz. The transducers are calibrated using an absolute surface wave calibration technique to yield a displacement sensitivity of 40 dB (ref 1 V/µm).

Figure 3.10 P-Wave transducer

(b) Preamplifier

The signal recorded by the piezoelectric crystals is passed to Panametrics – NDT^{TM} model 5660B wide band preamplifiers. The frequency range is flat between the range of 500 kHz - 40 MHz and has a gain setting of either 40 dB or 60 dB. In this study, a gain of 60 dB is

applied for acoustic monitoring during the experiment. The amplified signal is passed on to signal conditioning card of the Digital Wave™ recording system.

(c) Signal Conditioning Unit

The signals from the preamplifier are further amplified and filtered using FM-1™ Low Frequency Ultrasonic Signal Conditioning Unit manufactured by Digital Wave™ Corp. The modules have three sections – internal preamplifier, signal and trigger conditioning sections, and filter settings. The system conditions signal in 20 kHz to 2.3 MHz frequency range before digitizing. The internal amplifiers also can apply up to 42 dB gain in the increments of 6 dB. The signal conditioning and trigger sections of the FM-1™ get the signal after the pre-amplification. The signal condition section thereafter applies an additional gain of 24 dB and high pass frequency filter with a cut-off for low frequency of 20 kHz, 50 kHz, or 100 kHz. The trigger conditioning section applies an additional gain of 21 dB and a high pass frequency filter with threshold settings of 50 kHz, 100 kHz or a low pass frequency filter of 750 kHz, 1 MHz or 5 MHz.

(d) Data Acquisition Module

The data acquisition module is an ICS-645 PCI bus analog input board. The conditioned signal from the FM-1™ unit is fed to this module. The module has 32 channels with a maximum sampling rate of 20 MHz. In this experiment, 16 channels were utilized, and a sampling rate of 5 MHz was used. Figure 3.11 shows the setup for data acquisition module. The schematic for the AE monitoring setup is shown in Figure 3.12:

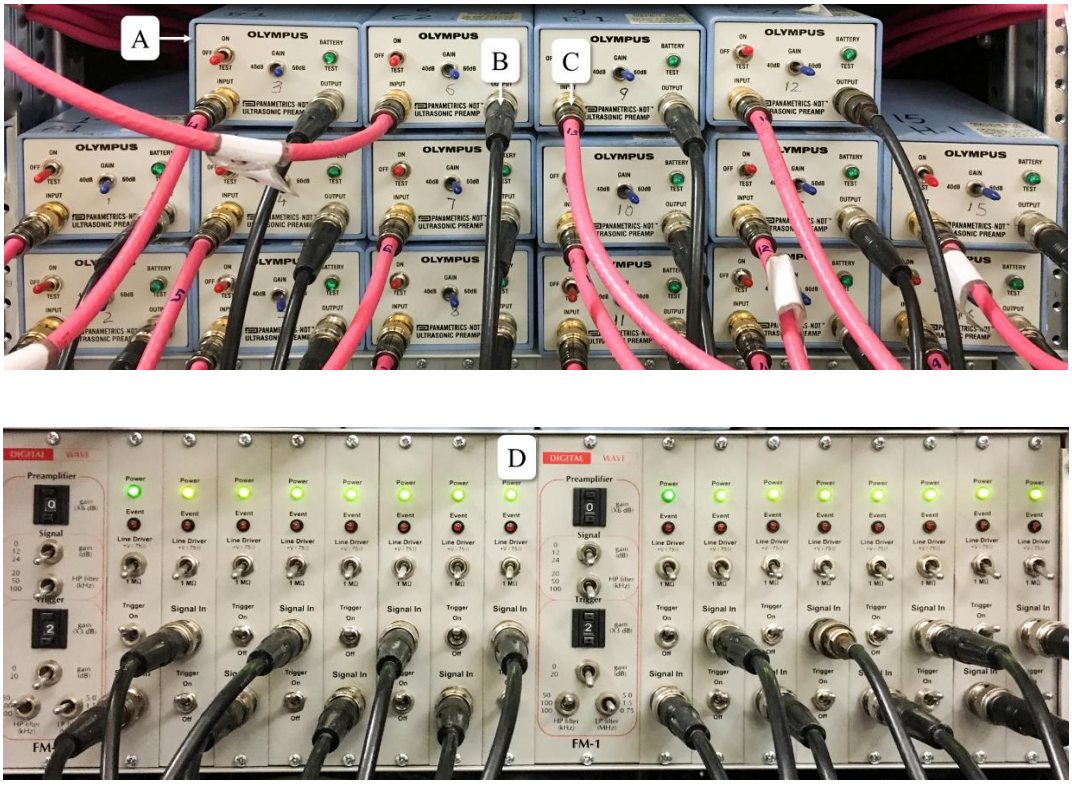

Figure 3.11 Acoustic monitoring system: (A) stack of 16 Preamplifiers (B) amplified signal fed to signal conditioning unit (C) input - received acoustic signal from transducers (D) 16 channel FM-1™ low frequency ultrasonic signal conditioning unit (manufactured by Digital Wave™ Corp.)

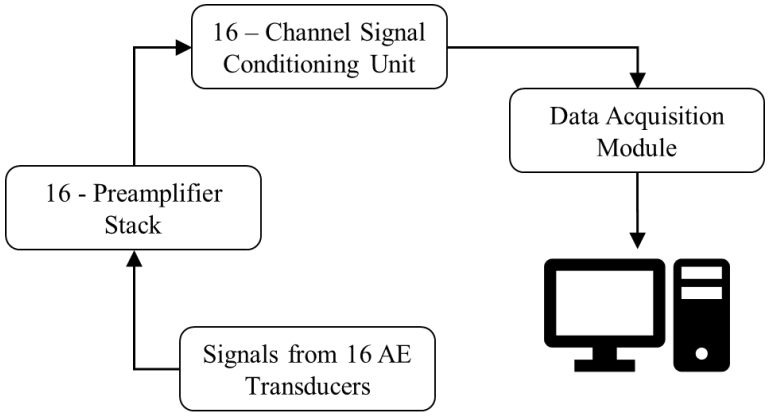

Figure 3.12 Sixteen AE transducers, 16 preamplifiers, signal conditioning unit, data acquisition module and processing unit (Aso, 2009)

3.3 Equipment for shear wave measurement pre- and post-fracture

The experimental setup for shear wave measurement of rock sample is shown in the Figure 3.13 as below:

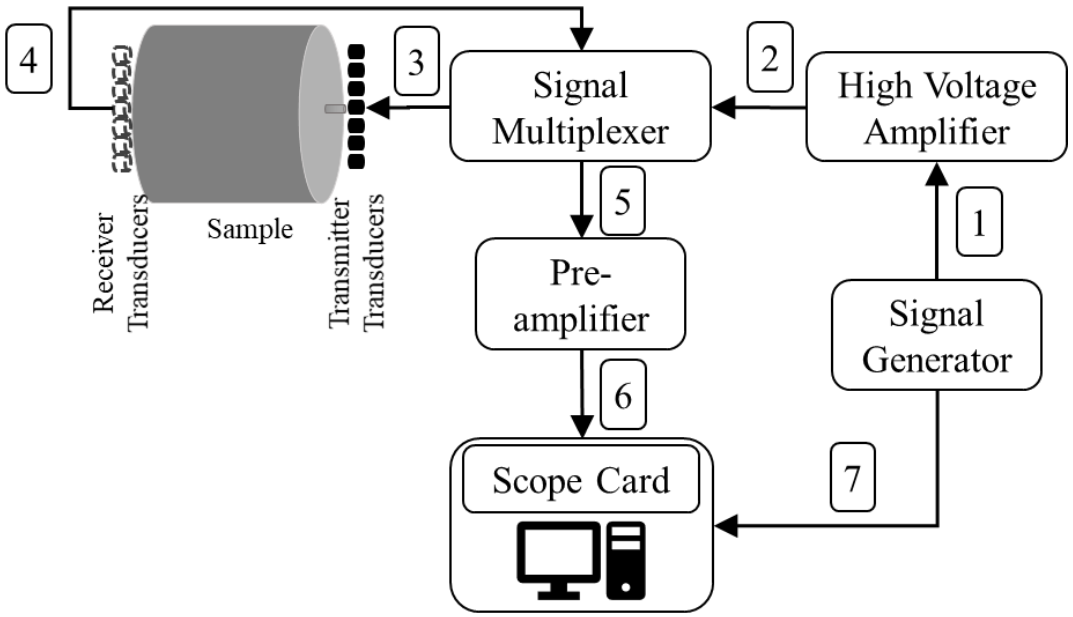

Figure 3.13 Schematic of the complete experimental setup for shear wave recording system (showing the sequence of process)

The setup consists of: (1) signal generator; (2) high voltage amplifier (3) signal multiplexer; (4) S-wave transducers; (5) pre-amplifiers; (6) scope system (7) motor for core movement. The workflow is shown by the numbers over the arrows for signal movement in Figure 3.13. Each sub-system is discussed in subsequent sections.

3.3.1 Signal Generator

The signal generator used is Agilent Technologies 33220A (shown in Figure 3.14). A burst of mono-frequency sinusoidal signals is generated. Signal bursts are sent every 25 μs and recorded at the same time interval.

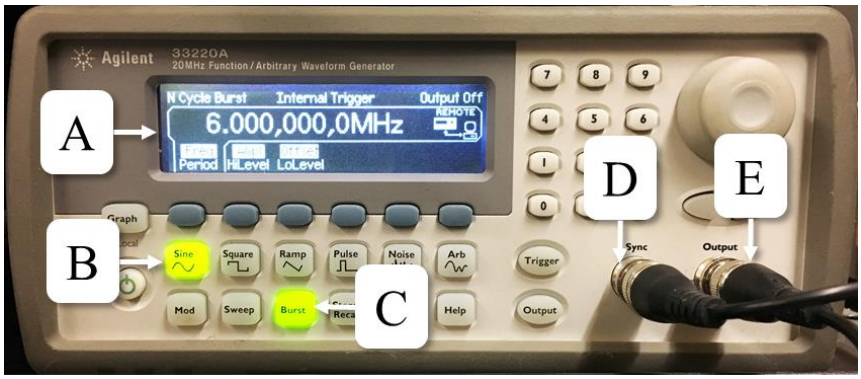

Figure 3.14 Agilent Technologies 3320A 20 MHz function generator: (A) front panel display; (B) sine function generated for this experiment; (C) burst mode; (D) sync connection to the scope card; (E) output to high voltage generator

3.3.2 High Voltage Generator

The high voltage generator is used to amplify the output of the signal generator to drive the transducers. The HV generator, manufactured by Digital Wave™ recording system, has a ±3 dB. response from 25 kHz to 720 kHz, and a total frequency range from 5 kHz to 1 MHz. The amplifier can output 740 V into a 1 MΩ load. HV generator is set to 4.5 V. Figure 3.15 shows the front panel view.

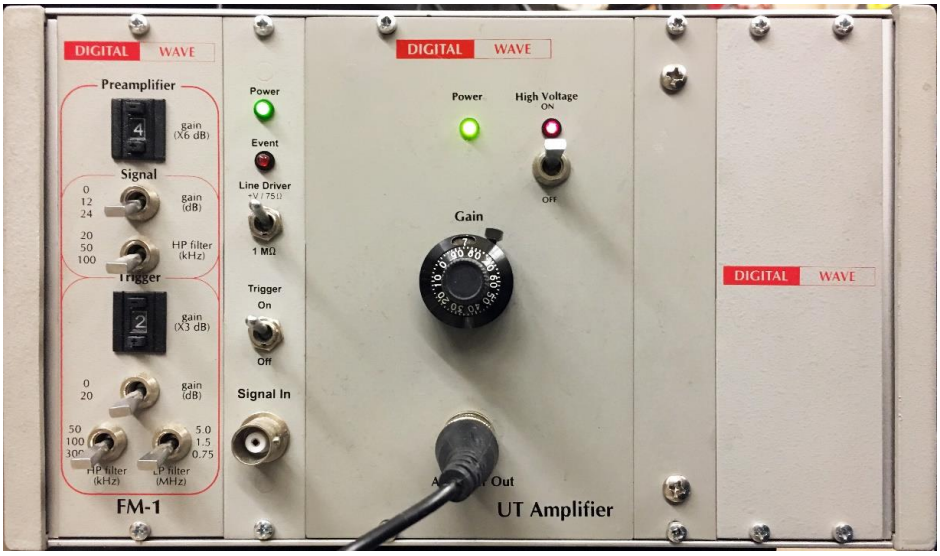

Figure 3.15 High Voltage Generator panel front view, manufactured by Digital Wave™ recording system

3.3.3 Signal Multiplexer

The conditioned signal from the high voltage generator is fed to the GX7610 signal multiplexer module manufactured by Geotest Marvin Test Solutions™. The card has four groups of 1x4 multiplexer scanners that converts the input conditioned signal from the HV generator into 14 output signals. The unique feature about the multiplexer is its ability to handle high voltage.

Input waveform from the high voltage generator is passed sequentially to each transducer one after the other and are recorded by the corresponding receiver transducers.

After data has been acquired and recorded for transducer 1, automatic relay switch occurs to send the signal to transmitter transducer 2 and receive the corresponding signal from receiver transducer 2.

The sequence continues until data from all the 7 pairs of transducers are recorded. More description of the signal switching between transducers is given in the Appendix.

3.3.4 Polarized shear wave transducers

Each transducer assembly consists of 2 piezoelectric crystals with flat surface to match the flat surface of the rock sample. The shear wave assembly is shown in Figure 3.16. The transducers are 0.5 inch, 1 MHz PZT-5A polarized shear crystals manufactured by Boston Piezo-Optics Inc.

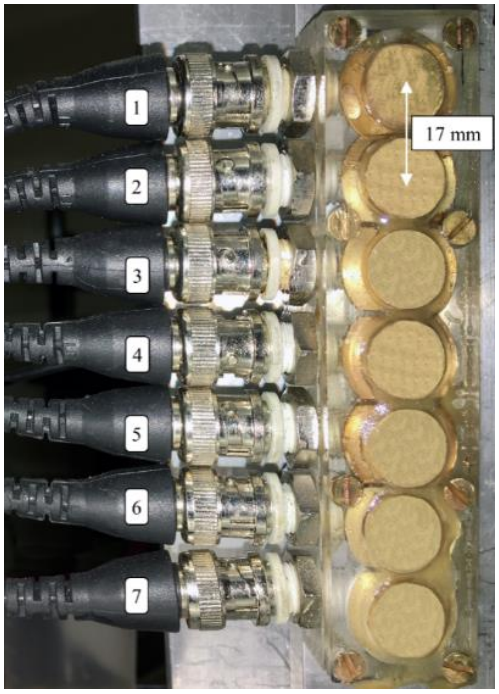

Figure 3.16 Seven ½-inch shear wave transducer stack mounted on spacer bar, positioned 17 mm apart center to center

The transducers are stacked one above the other, 17 mm apart center to center and mounted on a spacer bar, as shown in Figure 3.16.

3.3.5 Preamplifier

The signal acquired from the receiver transducer is passed to a Panametrics – NDT^{TM} model 5660B wide band preamplifiers. It is the same preamplifier as discussed in section 3.2.4 (b). All the transducer output signals pass through the same preamplifier sequentially.

3.3.6 Scope Card

The scope card used is PCI-5122 manufactured by National Instruments. The card is installed in the PCI slot of the computer. The card is a 100 MHz bandwidth, 100 MS/s, 14-bit PCI oscilloscope device. The scope card is shown in Figure 3.17.

Figure 3.17 NI PCI-5122 scope card

3.4 Experimental Procedure

3.4.1 Pre-fracture Shear Wave Measurement

Cylindrical rock samples having diameter 6 inch and approximate length of 6 inch were cut and the flat end surfaces were polished.

One Tennessee sandstone and 2 pyrophyllite samples were tested in this study. Samples TSU-6 and PY-1, 2 were fractured in their native dry state using different injection fluids.

The direction of the natural foliation was established using CVA. The sample is then placed in the shear wave response measuring system to record the polarized shear wave response in two orthogonal polarization relative to the natural foliation as a pre-fracture background check. These measurements are made parallel to the axis of the core. Figure 3.18 shows the experimental setup for recording the polarized shear wave response through the rock sample. Each component is discussed in section 0.

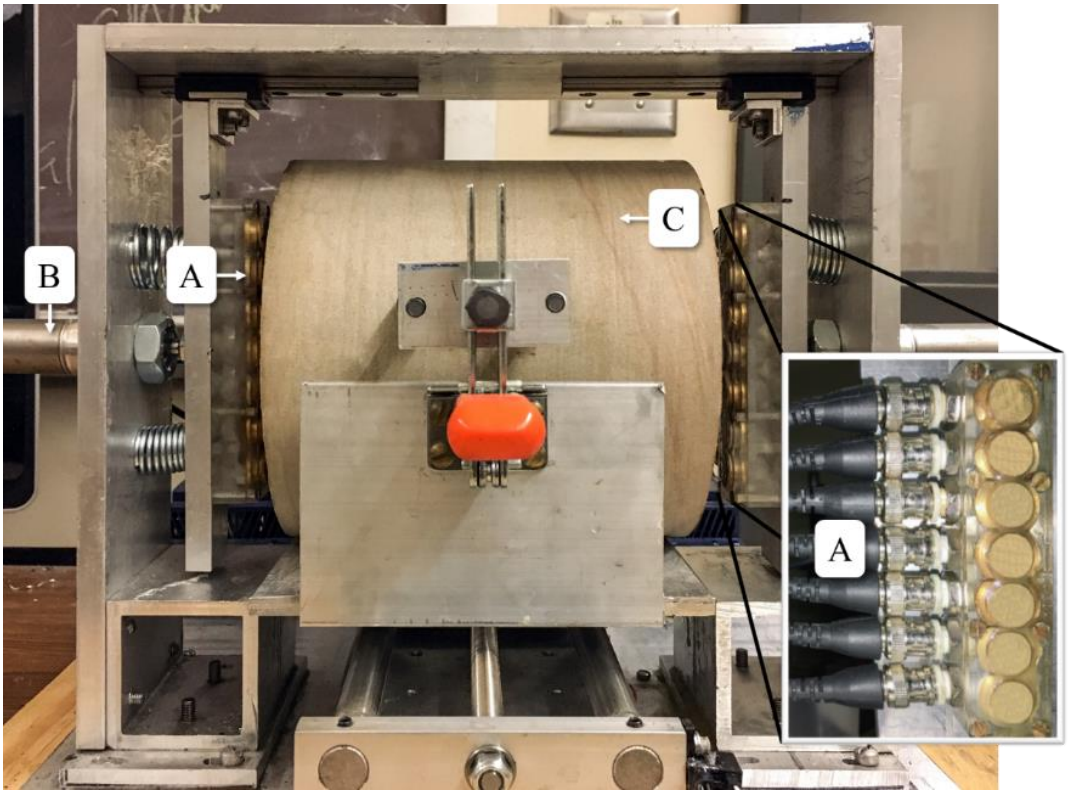

Figure 3.18 Experimental setup for polarized shear wave response measuring system: (A) 0.5 inch. Shear wave transducer positioned 17 mm apart center to center; (B) piston to apply pressure to ensure proper coupling between transducer and sample surface; (C) rock sample

The rock sample is secured with locking system shown in Figure 3.18. The transducer stacks (transmitter and receiver) are pressed to the face of the sample through actuated pressure piston to make a firm coupling. Honey is applied as a coupling agent between the transducer and the rock sample. The rock sample is oriented to have its natural foliation (as determined from CVA) parallel to the transducer polarization. The reading from such orientation is defined as parallel polarization shear wave data. Data is acquired using a 6 MHz pulsed sine wave.

The bottom plate on which the sample rests, is moved laterally every 1 mm while the transducer stack records shear wave response across the faces of the sample, recording 7 shear waveforms at every mm.

The sample is then rotated by 90^{o} to align the transducer polarization with the direction orthogonal to the natural foliation of the rock sample. Shear wave response are recorded the same way as discussed above for the orientation defined as perpendicular polarization shear wave data.

For a 6-inch diameter sample, the 7 pairs of transducers scan the sample across paths shown in Figure 3.19. Greyed-out zone represents the area not scanned by the transducer pairs.

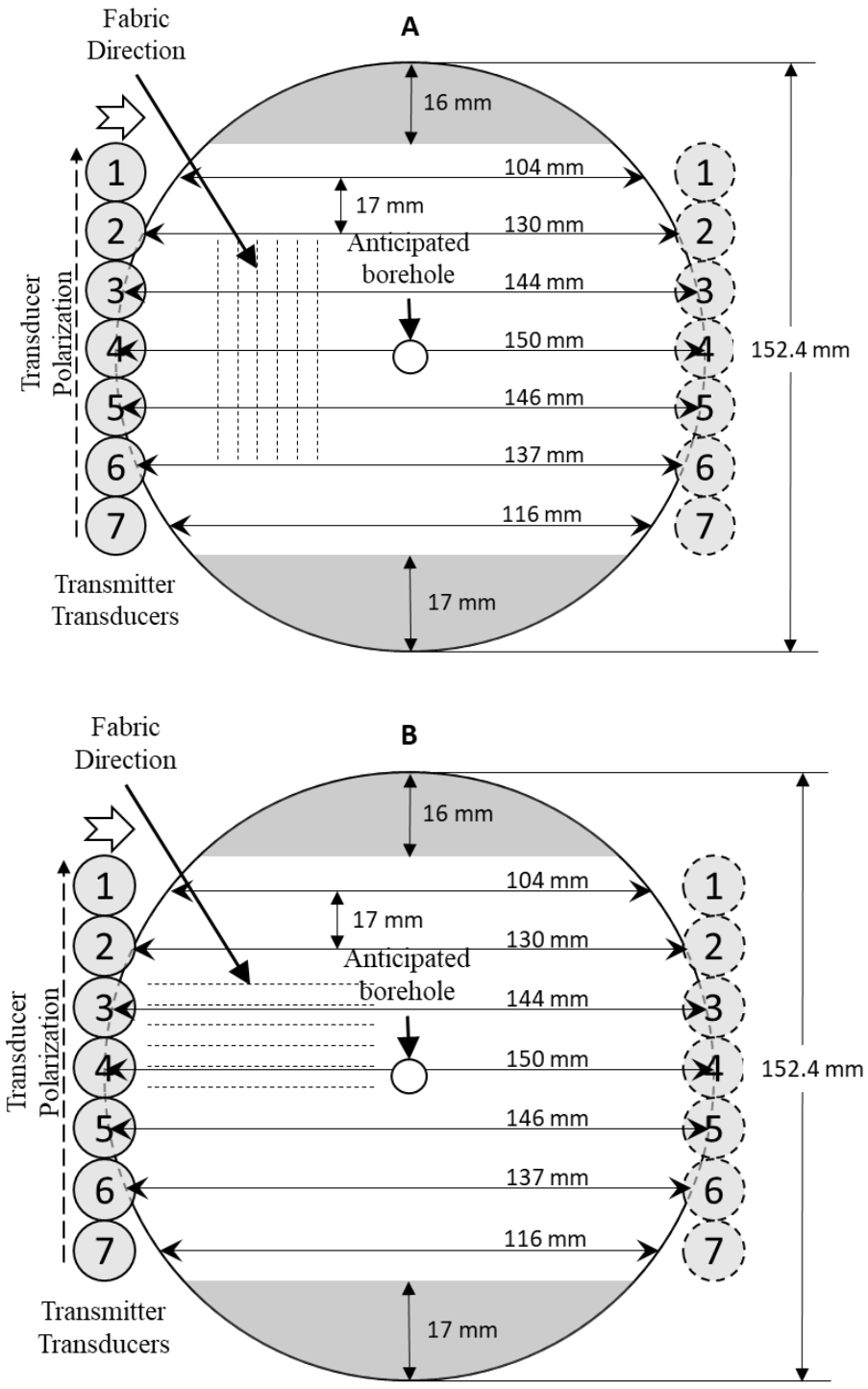

Figure 3.19 Schematic showing transducer positioning and movement with respect to 6" diameter sample flat face. The greyed-out zone on top and bottom represent the area not scanned by the transducer. Arrow on top of transducer stacks show the direction of transducer movement. (A) and (B) denote the two orthogonal polarization of transducer with respect to fabric direction.

3.4.2 Uniaxial Hydraulic Fracturing

A hole of diameter 0.25-inch was drilled at the center of the sample from the top to a depth slightly more than half the specimen length. A concentric borehole of diameter 0.5-inch was drilled at the center of the sample around the previous drill up to a depth of around 0.4 inch to ensure sealing with epoxy around fluid injection tubing. Steel tubing, 0.25-inch in OD and 0.187-inch ID, with two slots 180^o phase apart is positioned approximately 0.15 inch from the bottom and cemented in place using JB Weld™ epoxy. The bottom opening of the tubing was also sealed using the same epoxy before it was inserted into the drilled hole. The epoxy was allowed to set firmly at room temperature for 24 hours.

The dimension and the well parameters for the samples are listed in Table 3-4:

Table 3-4 Rock sample dimension and completion parameters

Sample ID	Dimensions and Completion Parameters (mm)					
	Length	Diameter	Borehole Depth	Counter-borehole depth	Injection Depth	Injection Fluid
TSU-6	154.0	152.5	83.0	11.8	80.0	Water
PY-1	152.6	152.6	78.0	12.1	75.1	Water
PY-2	152.5	152.5	79.8	12	75.0	Oil

16 piezoelectric transducers are mounted on the rock sample with 14 distributed uniformly across the azimuth and height of the curved surface of the sample avoiding the locations where uniaxial horizontal stress would be applied, and two transducers are mounted on the top of the sample. A schematic of the sensor locations along with their Cartesian coordinate (assuming the well top to be the origin) is shown in the Appendix. A schematic of this completion is shown in Figure 3.20:

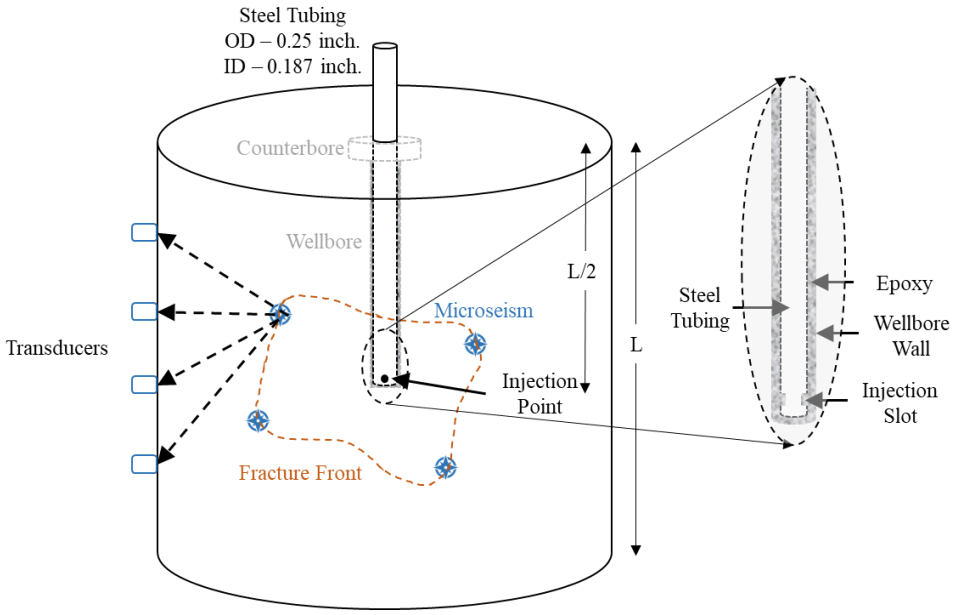

Figure 3.20 Hydraulic fracturing test specimen schematic. Sample is drilled with 0.25 inch. OD centered wellbore with injection point near the end of the tube located approximtely half the length of the sample

Uniaxial stress perpendicular to the foliation in each sample is applied and the effective applied stress is summarized in Table 3-5. Figure 3.21 shows the direction of the foliation by dotted lines and the applied stress by the arrows. Table 3-5 shows the values of effective stress applied perpendicular to the fabric, for each sample.

Table 3-5 Stress state for Tennessee sandstone and pyrophyllite sample hydraulic fracture tests

Sample	Injection fluid	Effective applied stress (psi)
TSU-6	Water	870
PY-1	Water	840
PY-2	Oil	820

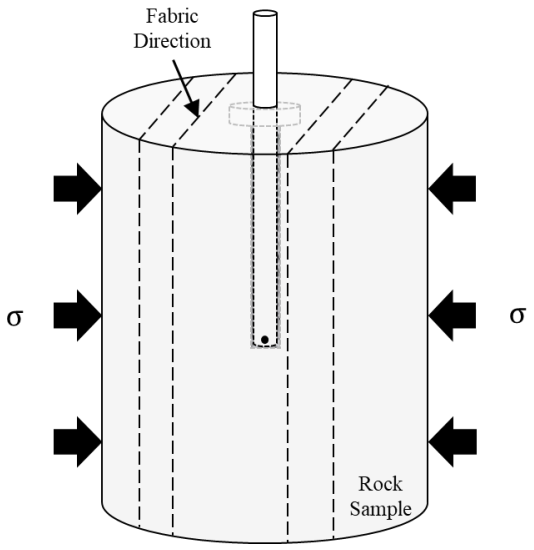

Figure 3.21 Stress and rock fabric orientation for the four samples being tested. Test configuration has maximum stress perpendicular to fabric direction

The sample is fractured by pumping fluid at a constant rate of 15 ml/min through the tubing. The flow rate and the pressure are monitored remotely. Fluid is pumped till breakdown is achieved and a stable pressure flow is established post-breakdown.

3.4.3 Post-Fracture Shear Wave Measurement

The tubing outside the fractured sample is cut off to facilitate shear wave measurements (as explained in section 3.4.1). Shear wave acoustic response is recorded for the fractured sample for the desired transducer polarization with respect to the foliation direction of the rock sample.

The sides of the sample are subsequently cut off 0.5-inch from the sample boundaries (parallel to the fractured plane) to allow recording shear wave response along the sides of the sample as shown in Figure 3.22. This enables analyzing the shear wave response across the plane perpendicular to the direction of the fracture generated. The sample is cut 0.5-inch from both the sides as shown in Figure 3.22 such that the sample is 5 inches in length across the cut

section. It is cut as such because the maximum extension of the pressure-actuated transducer mount is 5-inches as shown in Figure 3.23:

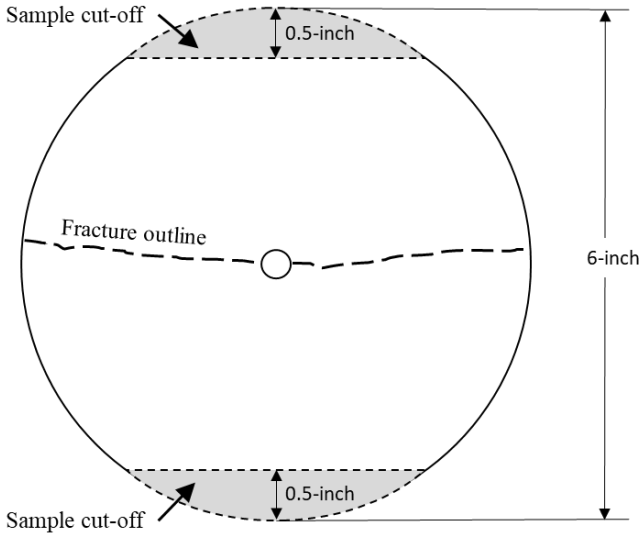

Figure 3.22 Schematic shows the rock sample top view. Sample is cut off on sides 0.5-inch from the ends, parallel to the fracture plane to enable shear wave measurement polarized perpendicular to the fracture plane

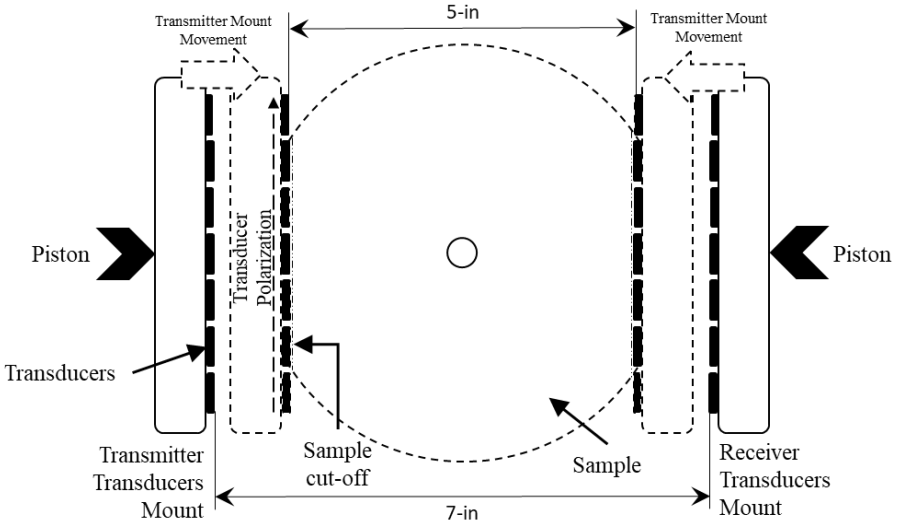

Figure 3.23 Schematic showing transducer mount movement. The transducer mount can extend to accommodate samples sizes ranging from 5 - 7-inch width

Shear wave measurements are taken on the flat surface on the sides of the rock sample in the same way as described in section 3.4.1. Shear wave response is recorded for orthogonal

polarizations in the plane parallel to the fracture plane. Figure 3.24 shows the sample region in which the shear wave measurements are done.

In configuration (B), transducer pairs 1 and 7 (white bordered transducers in Figure 3.24 (B)) do not record any data as they are out of the side flat surface.

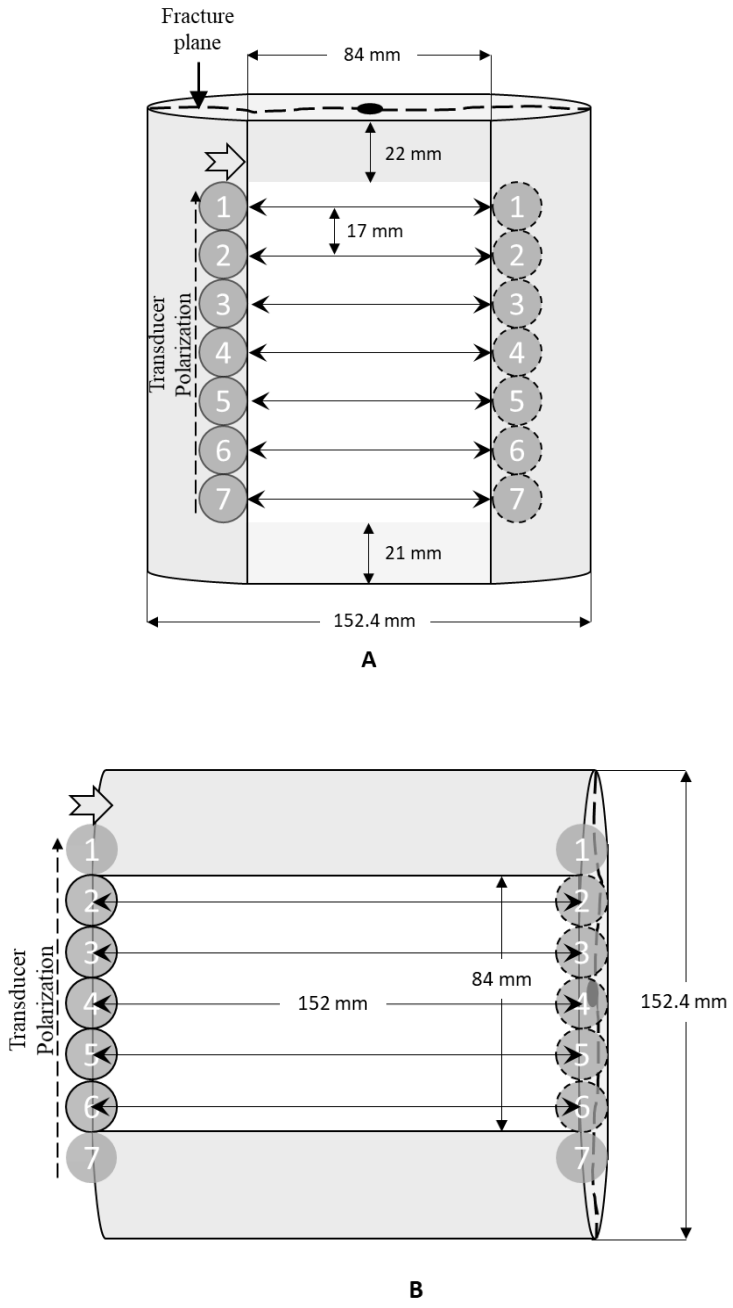

Figure 3.24 Schematic showing transducer positioning and movement with respect to 6" diameter sample cut side face. The greyed-out zone on top and bottom represent the area not scanned by the transducers. Configuration (A) and (B) represent two perpendicular position of rock sample to acquire orthogonal shear wave polarization response. Arrows on top of transducer stacks show the direction of transducer movement.

The sample is cut again on the sides 0.5-inch from the sample boundaries, this time across a plane perpendicular to the fracture plane to allow recording shear wave response on the sides of the sample as shown in Figure 3.25. This enables analyzing the shear wave response across the plane parallel to the direction of the fracture generated.

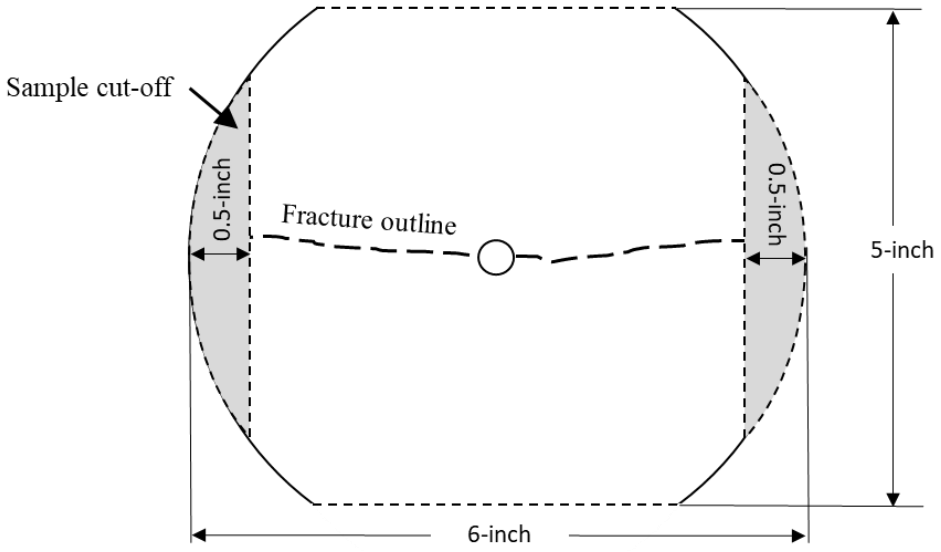

Figure 3.25 Schematic shows the rock sample top view. Sample is cut off on sides 0.5-inch from the ends, perpendicular to the fracture plane to enable shear wave measurement polarized parallel to the fracture plane

Shear wave measurements are taken on the flat surface on the sides of the rock sample in the same way as described in section 3.4.1. Shear wave response is recorded in the same way as is shown in Figure 3.24, but for orthogonal polarizations perpendicular to the fracture plane.

4 RESULTS AND DISCUSSION

4.1 Tennessee Sandstone

Tennessee sandstone is a low porosity and low permeability sandstone (See Table 3-1). It mainly consists for quartz (See Table 3-3). It has an average grain size of approximately 190 μm. CVA results on TSU-6 indicate that it is isotropic (See **Error! Reference source not found.**). Uniaxial hydraulic fracturing test was performed on a Tennessee sandstone sample. Table 4-1 gives the summary of the experiment on the Tennessee sandstone. The fracturing fluid in the experiment was water of 1 cP viscosity at constant injection rate of 15 cc/min at ambient temperature.

Table 4-1 Uniaxial hydraulic fracture test parameters on Tennessee sandstone (vertical core)

Sample ID	Stress (psi)	Fracturing fluid	Flow rate (cc/min)	Breakdown Pressure (psi)	Located AE/Good AE
TSU-6	870	Water	15	2764	1309/3299

4.1.1 Pressure and AE response

The effective applied stress was 870 psi perpendicular to the direction of the foliation as determined by CVA (See Figure 3.2). Figure 4.1 shows the pressure curve (black markers) and the acoustic emission (blue markers) recorded as a function of time. There is a linear increase in pressure at 470 psi/s until the breakdown pressure of 2764 psi when the rock failed. Following the breakdown, the pressure rapidly dropped at the rate of 1876 psi/s to 400 psi, thereafter, increasing to a pressure of 880 psi, which is the pressure about the principal stress.

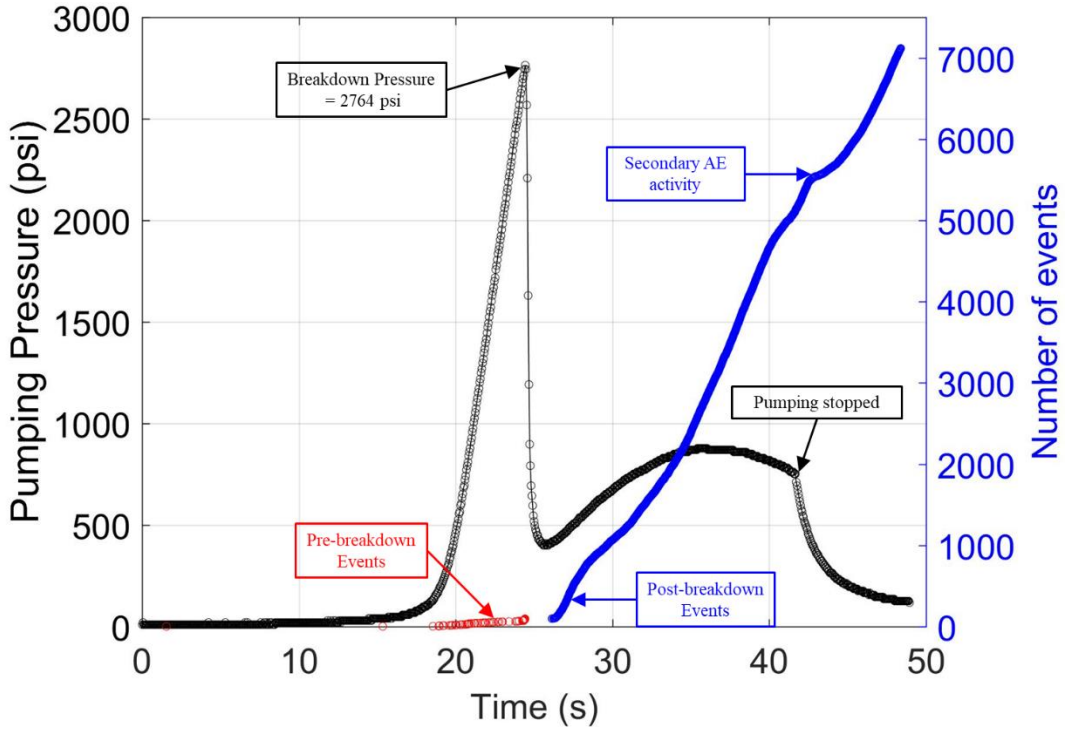

Figure 4.1 Injection pressure (black markers) and acoustic event (red and blue markers) are plotted as a function of time for Tennessee sandstone TSU-6. Red markers are the events occurring before breakdown and blue markers are events after breakdown. There is a gap in AE at breakdown

A total of 7118 acoustic events were recorded using a triggered recording system. It is observed that AE activity begins before the breakdown happens and those pre-breakdown events are plotted in red markers. The pre-breakdown events may occur due to rock failure from the stress induced by the pressurization of the rock and injected fluid entering the pore spaces of the rock.

There is a gap in the AE activity at breakdown and thereafter a sudden burst of AE following the pressure drop. This observed gap may be due to the extremely high rate of AE during the period which could saturate the triggered recording system and hence were not recorded.

After the injection was stopped, a rapid burst of secondary AE was observed. It may be due to the failure of the asperities associated with fracture closure when the injection is stopped (Chitrala, 2011).

4.1.2 AE Location – Methodology

(a) AE location algorithm

The individual first arrival times of the compressional wave acoustic events recorded at each sensor is automatically picked using an algorithm known as STA/LTA, developed by Ortiz (2010). The arrival times are then used to determine the location of the events using least square inversion method. The method is described by Moreno (2011). Assuming a cartesian coordinates of the sensors to be x_s, y_s and z_s, and the coordinates of the ith event as x_i, y_i and z_i, the arrival time for the ith event is then given by:

$$t_i = t_o + \frac{\sqrt{(x_i - x_s)^2 + (y_i - y_s)^2 + (z_i - z_s)^2}}{v} \qquad (4\text{-}1)$$

t_o is the acoustic event origin time and v is the velocity of the medium. The unknowns in equation (4-1) are (x_i, y_i, z_i, t_o). The unknowns constitute the model vector *m* that represents the AE location and the origin time. The equation can be reformulated in vector form as:

$$d = A(m) \qquad (4\text{-}2)$$

d represents the vector comprising of the arrival times at various sensors. '*A*' is the function operating on model vector *m* to result in vector *d*. Here m is the unknown and hence, solving for *m* is an inverse problem. To solve the four unknowns (x_i, y_i, z_i, t_o), we need four equations. We have 16 acoustic sensors, that result in a maximum of sixteen unique equations depending on the quality of acoustic wave recorded for each event as well as the possible identification of the first arrival. This results in a highly over determined problem and an iterative process is necessary to arrive at the best fit model. Equation (4-2) needs to be linearized to arrive at a solution, and only linear least square technique is applied. Linearization is achieved using

Taylor expansion and neglecting the higher order terms. This results in a linear expression as below:

$$\Delta d = G\Delta m \tag{4-3}$$

Where *G* is the partial derivative matrix defined as:

$$G_{ij} = \frac{\partial d_i}{\partial m_j} \tag{4-4}$$

Since *G* is not a square matrix, hence Δm cannot be determined by simply multiplying both sides by G^{-1}. The alternate way to solve the equation is by using an alternate matrix called the generalized inverse of *G*. It is shown in the expression below:

$$\Delta m = [G^T G]^{-1} G^T \Delta d \tag{4-5}$$

G^T is the transpose of matrix *G* and the expression $[G^T G]^{-1}$ gives the generalized inverse of the matrix *G*. This expression can be further improved by accounting for the quality of the signal received at each sensor. That can be achieved by assigning an additional weight to the sensors with higher signal to noise ratio as compared to the ones with poor quality signals. Mathematically, it can be achieved by introducing the covariance matrix (C_d) of the data vector *d* on to equation (4-5):

$$\Delta m = \{[G^T C_d G]^{-1} G^T C_d\} \Delta d \tag{4-6}$$

Equation (4-6) is the weighted least square inverse solution. An initial assumption is made for the model vector m^o to predict the value of data vector d^o using Equation (4-3). The change in data vector is then obtained by:

$$\Delta d = d - d^o \tag{4-7}$$

The assumed model vector m^o, along with the observed data d is used to calculate the expression on the right-hand side in equation (4-6). Substituting the value of Δd from equation (4-7) into equation (4-6) to calculate the change in model vector Δm. This modified value of the model vector is used to improve the initially assumed value of m^o:

$$m = m^o + \Delta m \tag{4-8}$$

The process is iterated to improve the model vector in every subsequent step till the Δm is acceptably small (< 0.001 mm) or an iteration count is exceeded (10,000 iterations).

(b) Circumferential Velocity Analysis

Tennessee sandstone was treated as an isotropic medium and hence a constant velocity model is used to locate the AE. The first arrival travel times from the CVA measurements taken across the circumference of the sample are used to calculate the velocity. The averaged P-wave velocity over all the measured velocities was used to locate AE:

$$V_{avg} = 3.26 \pm 0.09 \text{ km/s}$$

4.1.3 Fracture Orientation and AE Location

The effective uniaxial stress on the sample during fracturing was 870 psi. Physical observation of the fracture shows that the fracture did not traverse completely to the sample top. Two fracture wings developed one on either side of the wellbore in the direction of the stress applied (parallel to X-axis); these are visible on the sides of the sample as shown in Figure 4.2. A uniaxial stress of 870 psi was sufficient to control the orientation of the fracture.

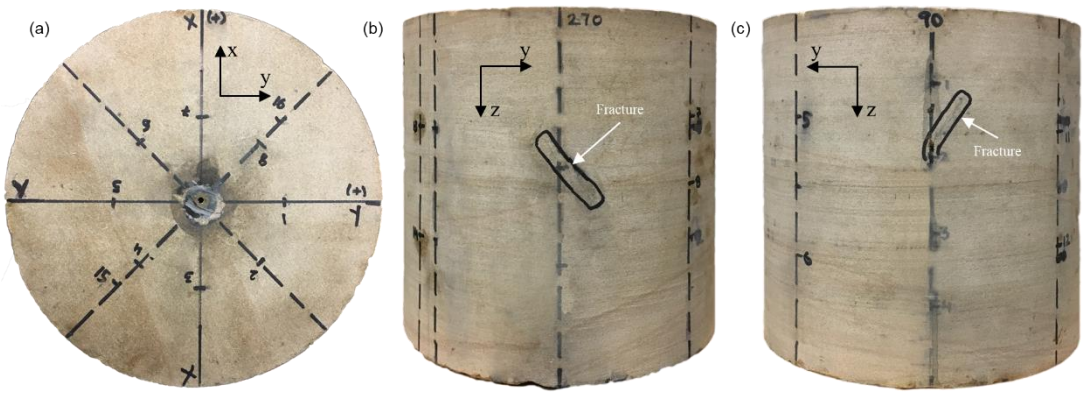

Figure 4.2 Surface observation of induced hydraulic fracture on TSU-6: (a) plan view; (b) and (c) side view (Sample length – 154.0 mm; Diameter – 152.5 mm)

A total of 3299 good and detectable first arrival acoustic events were recorded on at least 8 of 16 sensors; however only 1309 events could be located inside the sample (See Table 4-1). Figure 4.3 shows the plan (Figure 4.3c) and side (Figure 4.3a, b) views of the located AE during the time injection fluid was being injected. Events occurring before the breakdown are marked in red and the post-breakdown events are shown in black. The events are distributed throughout the sample with a vast majority lying along the fracture wings. In general, the distribution in the side view does align with the observed fracture trace on sample surface. The average error in hypocenter locations for this test was $\pm$6.04 mm (calculated using least square error estimation method). It is observed that AE events progress in the direction of the applied stress.

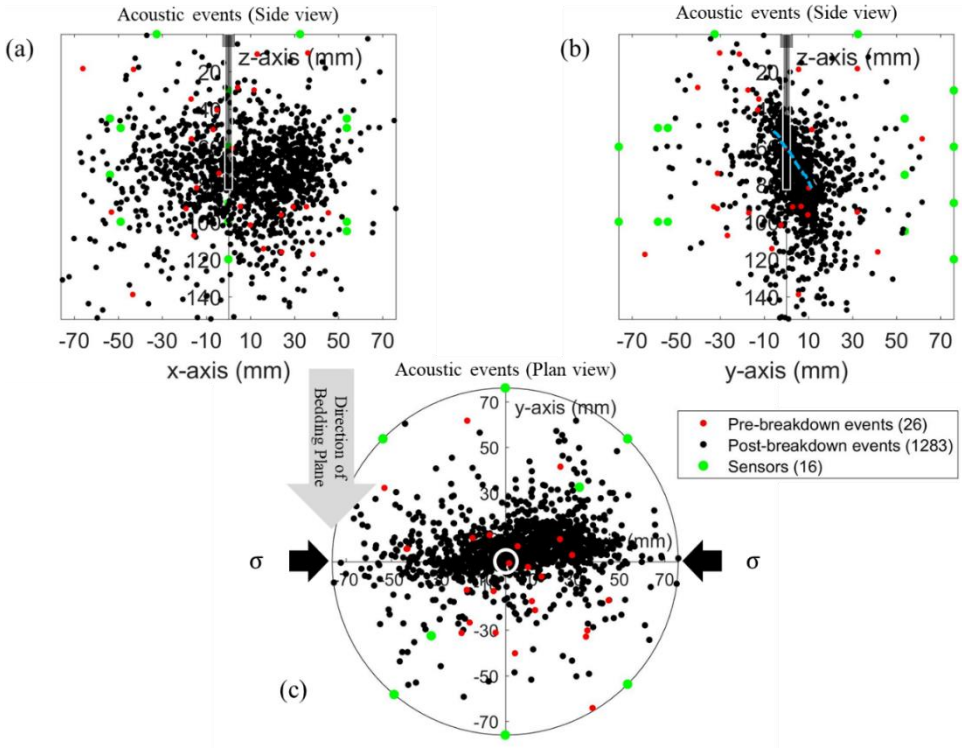

Figure 4.3 Plot of AE events for fractured sample TSU-6, fractured under uniaxial stress of 870 psi (shown by black arrows in plan view). Pre-breakdown events shown in red circles and post-breakdown events in black circles; (a) and (b) lateral views of AE. Broken blue line in (b) shows the actual fracture trace visible on the circumference of the sample; (c) plan view of AE hypocenter

4.1.4 Shear Wave Response

Shear wave velocities are measured at various points on the sample before and after it has been fractured. The method of data acquisition is discussed in section 3.4.1. For every polarization on the top surface, the 7 pairs of transducers record a total of 931 shear wave forms.

The individual first arrival times of the shear wave recorded by each pair of shear wave transducer is automatically picked using an algorithm, known as Modified Energy Ratio (MER), discussed by Ortiz (2010). MER is a modification of the Short Time Average/Long Time Average (STA/LTA) algorithm and works better for signals with low SNR (≈3 dB).

Measurement error associated with recorded first arrival times of the shear wave is estimated by recording the shear wave travel time at the same point on the sample for 20 readings and is found to be approximately ± 1.5%.

(i) Shear Wave Velocity Analysis

The shear wave velocity was computed from the recorded shear wave arrival time for before and after fracturing for the two polarizations. For every corresponding reading before and after fracturing, difference in the shear velocity was computed and converted into a percentage shear wave slowness as shown below:

$$\text{Shear Wave velocity Reduction } (\%) = \frac{V_{s(pre)} - V_{s(post)}}{V_{s(pre)}} * 100 \qquad (4\text{-}9)$$

where $V_{s(pre)}$ and $V_{s(post)}$ represent the computed shear wave velocity pre- and post- fracturing respectively. Note a positive value indicates that the velocity decreased after fracturing.

As discussed about the characteristics of shear wave in section 2.7, S- waves are affected by presence of fractures or cracks when their direction of propagation or their direction of polarization is at an angle to the fracture faces. Hence, the cracks or fractures induced by the hydraulic fracturing process on the sample would result in difference in the shear wave velocity, which is denoted by shear wave velocity reduction (SWR) (Equation (4-9). SWR has an associated maximum experimental error of ± 3% (twice the error in travel time measurement which is ± 1.5%). Plotting SWR in a heatmap would allow us to analyze the regions in the sample affected by fracturing and hence infer an SRV. The calculated SWR from equation (4-9) was plotted in a heatmap using convergent interpolation method in Petrel 2016 version. Figure 4.4 (a) and (b) shows the SWR heatmap for shear wave polarization parallel and perpendicular respectively, to the direction of the rock fabric determined from CVA (See

Figure 3.2) for top surface. Direction of rock fabric is along the y-axis. Acoustic events are superimposed onto the SWR map for comparison.

Hotter colors in the heatmap represent slower shear wave post fracturing, cooler colors represent low or no change in shear wave. Negative SWR is due to associated measurement error (± 3%) represented by the darker shades of blue color in the heatmap. Direction of the applied stress is indicated by the black arrows. Shaded regions in Figure 4.4 (a) and (b) are the regions where no shear wave data was recorded. The convergent interpolation method used to generate the heatmap extrapolates the available data to regions where no data is recorded. Hence, the region is shaded to avoid misrepresentation of recorded data. Acoustic events are superimposed into the SWR map in Figure 4.4 (a) and (b) for comparison.

Figure 4.4 (a) represents the SWR map for transducer polarization perpendicular to the applied stress direction. Shear wave would be slowed by presence of cracks and microfractures perpendicular to the direction of the polarization. A maximum slowness of 22% in shear wave is observed. Hence, hotter colors in Figure 4.4 (a) represent the presence of cracks in the direction parallel to x-axis i.e. they represent the slowness in shear wave due to primary fractures.

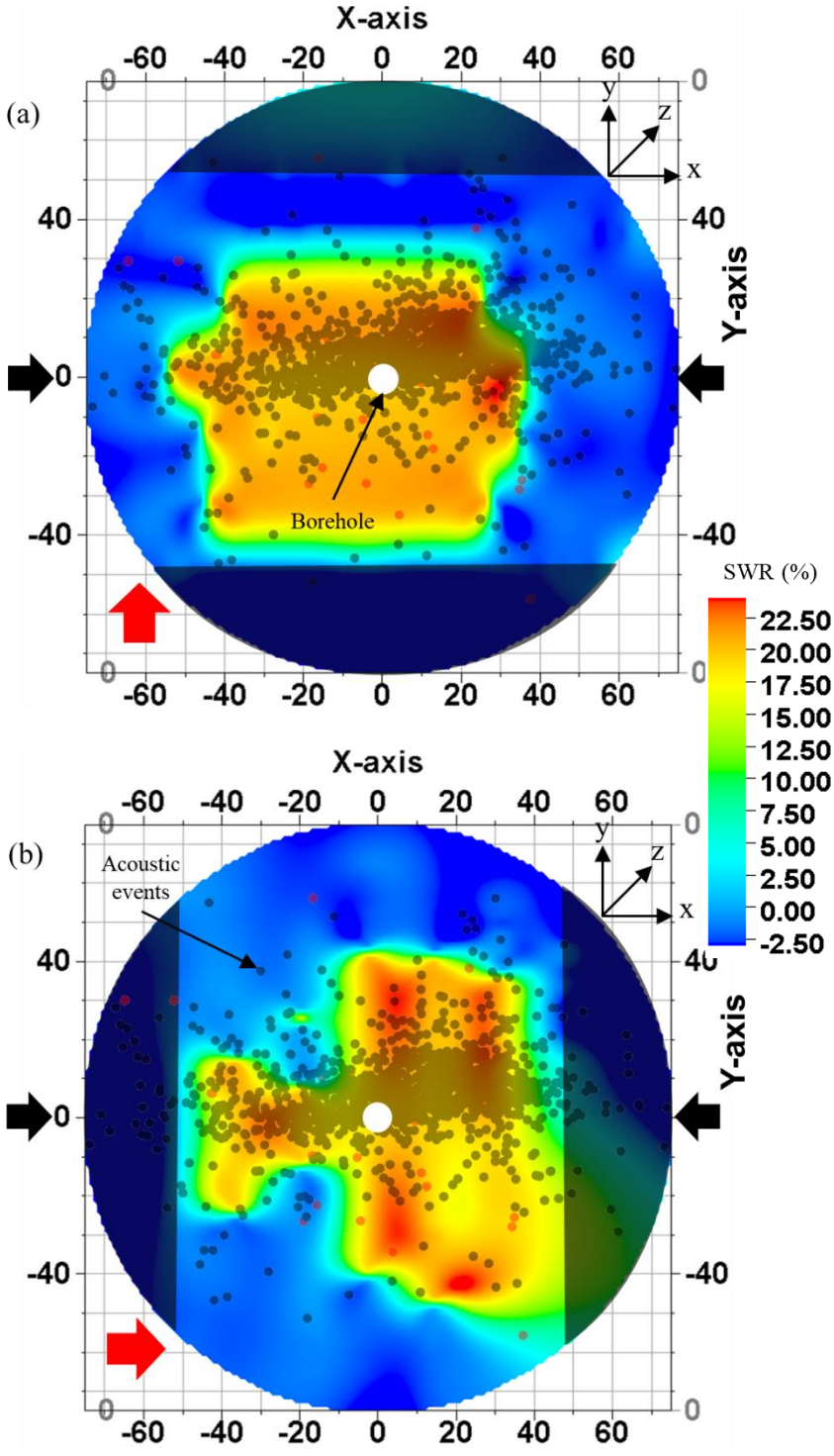

Figure 4.4 SWR map for top surface of Tennessee sandstone TSU-6 sample. Shear wave propagation is along z-axis. Transducer polarizations denoted by the red arrow in (a) and (b). Shaded areas represent areas of no recorded data. AE event locations are superimposed on the map.

Figure 4.4 (b) represent the SWR map for polarization parallel to the applied stress direction. A maximum of 24% slowness in shear wave is observed. Hotter colors represent the presence of cracks in the direction parallel to the y-axis.

The fracture growth seems to diminish as it propagated outwards from the central borehole towards the circumference along the x-axis. The SWR map also show a good match with the AE locations.

As discussed in section 3.4.3, the sample is cut 0.5-inch from the sample boundaries parallel to the fracture plane and shear wave response is taken through the sample. Figure 4.5 shows the side view of the sample after it had been cut. The sub-horizontal lines on the sample are the visible bedding planes in the sample.

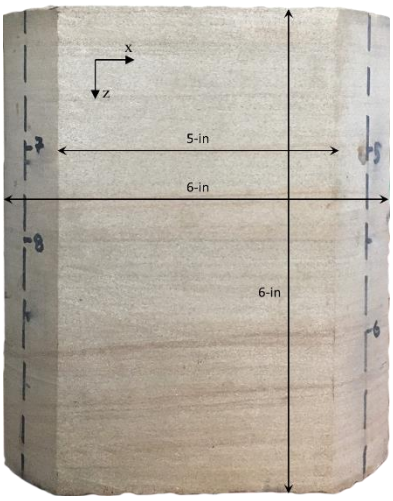

Figure 4.5 Side view of sample TSU-6, cut as per Figure 3.22

Shear wave response was not recorded through the sample in this direction. Hence, it is not possible to generate SWR map, however, the shear wave velocity (V_s) across the core is analyzed for orthogonal transducer polarizations. Figure 4.6 (a) and (b) show the V_s map for two polarizations in the plane parallel to the fracture plane. The mapped area shown

corresponds to the flat surface in Figure 4.5. The transducer polarizations are marked with the red arrow in each figure. Regions where no data are recorded is shaded.

The cooler colors in the map represent faster V_s while the warmer colors represent slower V_s. It is observed in Figure 4.6 (a), transducer polarization directed vertically in the plane, parallel to the Z axis (as shown by red arrow). V_s is in the range 2.10 – 2.15 km/s, from the sample top down to z = 80 mm below which the V_s gradually increases.

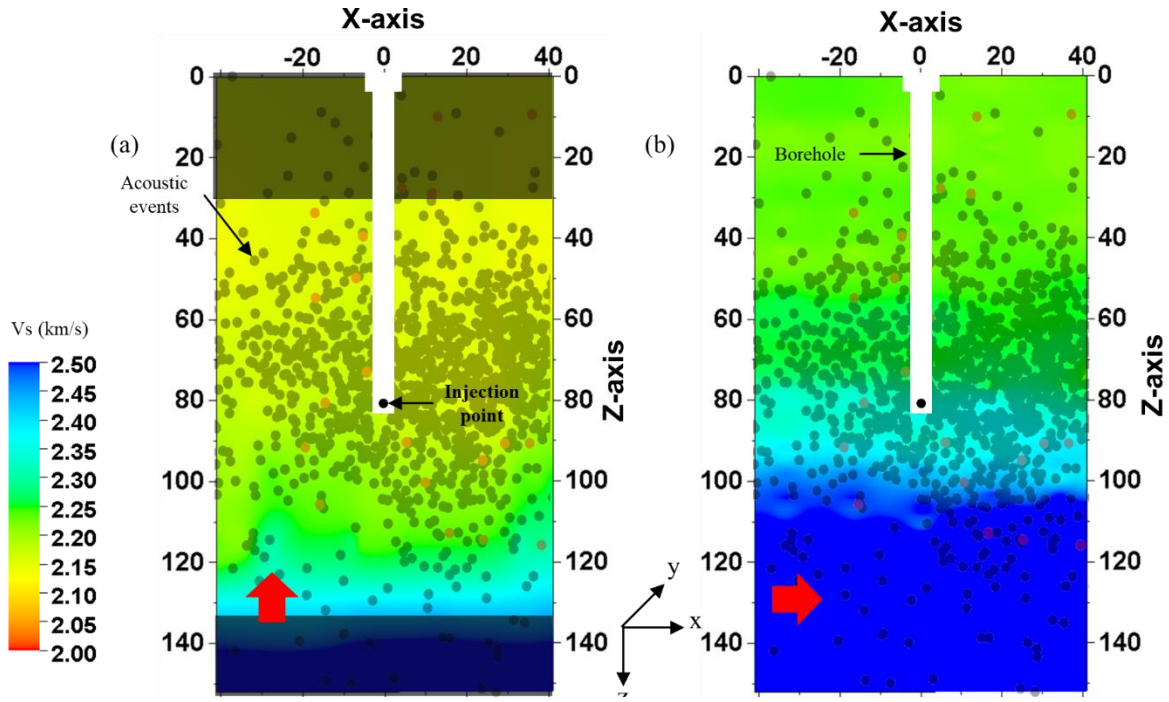

Figure 4.6 Shear velocity map on Tennessee sandstone sample TSU-6 across the sides parallel to fracture plane. Shear wave propagation is along y-axis. (a) and (b) map for orthogonal transducer polarizations represented by red arrows. AE event locations are superimposed on the velocity map. Shaded areas represent areas of no recorded data.

In Figure 4.6 (b), for polarization directed horizontally, in the X direction (as shown by red arrow), V_s is in the range 2.25 – 2.30 km/s, from z = 0 up to the injection point depth (z = 80 mm). V_s gradually increases above the injection point. Tennessee sandstone is an isotropic medium (see Figure 3.2), hence the slower V_s can be attributed to the presence of induced

primary fractures in sample. V_s is 5-7% slower in Figure 4.6 (a) compared to Figure 4.6 (b) although both the polarizations are perpendicular to the plane of the fracture. This can be attributed to presence of inclined fracture with respect to the direction of shear wave propagation. Secondly, it can also be due to the presence of secondary microfractures normal to the primary fractures in the horizontal plane. Based on SEM imaging of laboratory hydraulic fracturing of Tennessee sandstone core, Ratzlaff (2018) observed that secondary microfractures are oriented perpendicular to the primary fractures. The microscale SEM imaging observation aligns well with the observations in this study.

Sample is cut 0.5 inch from sample circumference, normal to the fracture plane as discussed in section 3.4.3, to analyze shear wave response. The sample is cut as shown in Figure 3.25. The cut sample is shown in Figure 4.7. Visible fracture outline on the flat surface is outlined with black marker as can be seen on the figure. It is observed that the fracture is inclined at an angle of 31^o to vertical. The sub-horizontal lines on the sample are the visible bedding planes in the sample.

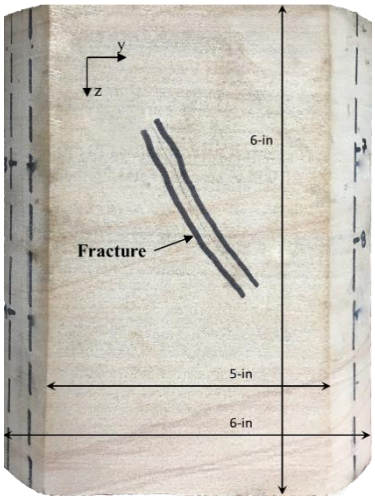

Figure 4.7 Side view of sample TSU-6, cut as per Figure 3.25

Shear wave first arrival travel times were recorded across this surface at various location and V_s was calculated for all the locations. Figure 4.8 (a) and (b) show the V_s map for two orthogonal polarizations in the plane parallel to the fracture plane. The mapped area shown corresponds to the flat surface in Figure 4.7. The transducer polarizations are marked with the red arrow in each figure. Regions where no data is recorded is shaded. Fracture outline visible on the sample surface is marked by the black dashed line.

In Figure 4.8 (a), transducer polarization is vertical, parallel to the Z axis (as shown by red arrow), slower V_s region (hotter color) appears to be inclined and correlates well with the physically observed fracture orientation on the sample (denoted by the black dotted line).

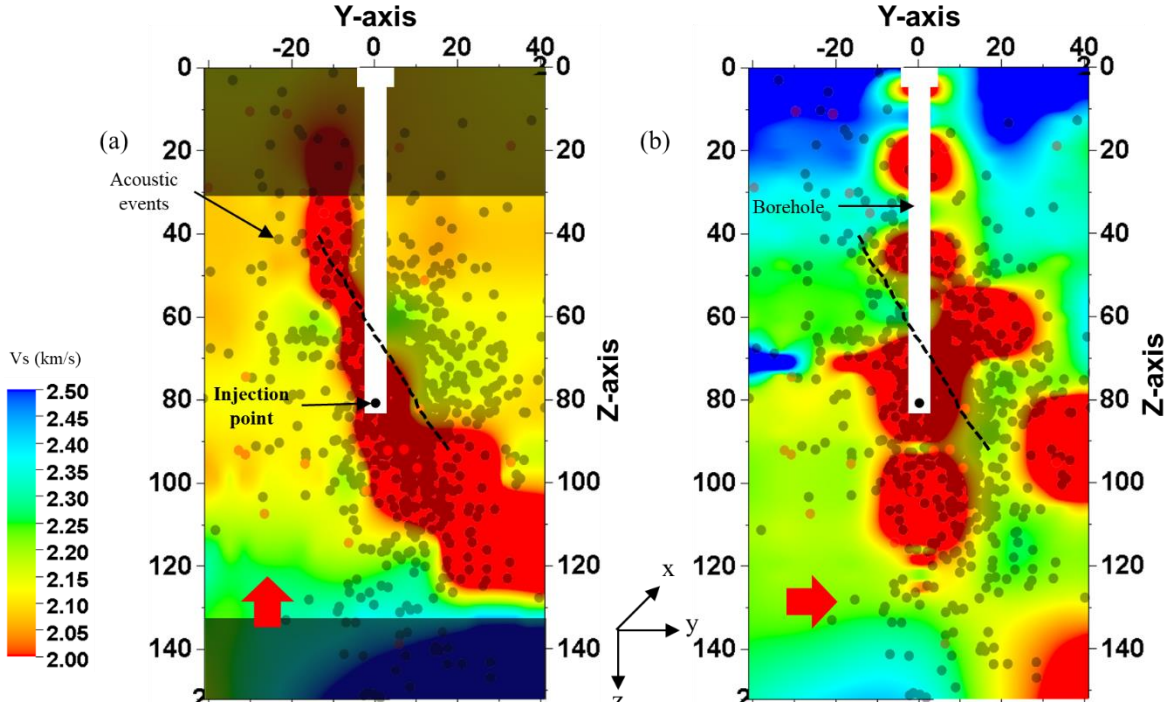

Figure 4.8 Shear velocity map on Tennessee sandstone sample TSU-6 across sides normal to fracture plane. Shear wave propagation is along x-axis. (a) and (b) map for orthogonal transducer polarizations represented by red arrows. AE event locations are superimposed on the map. Fracture visible on surface is shown by the black dotted line. Shaded areas represent areas of no recorded data.

Similar behaviour is observed in Figure 4.8 (b) where the transducer polarization is parallel to the horizontal plane as shown by the red arrow. The slower V_s area does not have an inclined signature as in Figure 4.8 (a). It captures the anisotropy introduced due to fracturing of the rock sample as both the polarizations have different response to the same fracture plane. Figure 4.8 (a) maps the introduction of cracks in the horizontal plane perpendicular to the fracture plane while Figure 4.8 (b) map the cracks in the vertical plane parallel to the fracture plane. Both the maps show good agreement with the spatial locations of acoustic events.

(ii) Shear Wave Frequency Analysis

Presence of cracks and fractures not only affect the first arrival, but also results in signal attenuation. The attenuation can be quantified by computing the frequency of the shear wave response around the first arrival. Spectral analysis of the shear waveforms was carried out by using Fast Fourier Transform (FFT) performed on a ± 5 μs window centered on the first arrival of the shear wave. Primary frequency (corresponding to the maximum amplitude in the frequency domain) was determined through FFT analysis. Figure 4.9 shows a sample shear waveform recorded during this experimental study and a 10 μs window around the first arrival time of the waveform.

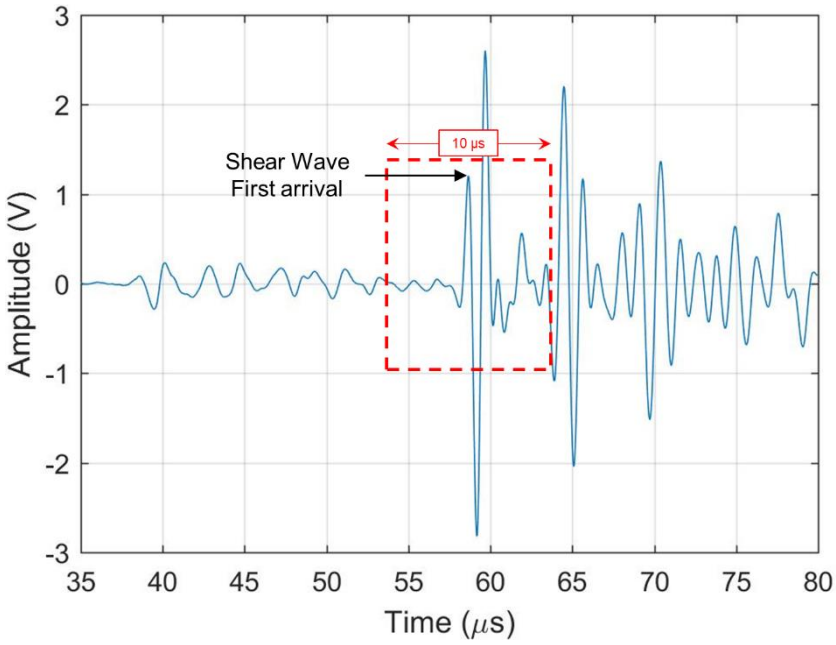

Figure 4.9 The 10µs window centered on the first arrival of the shear wave used for FFT computation

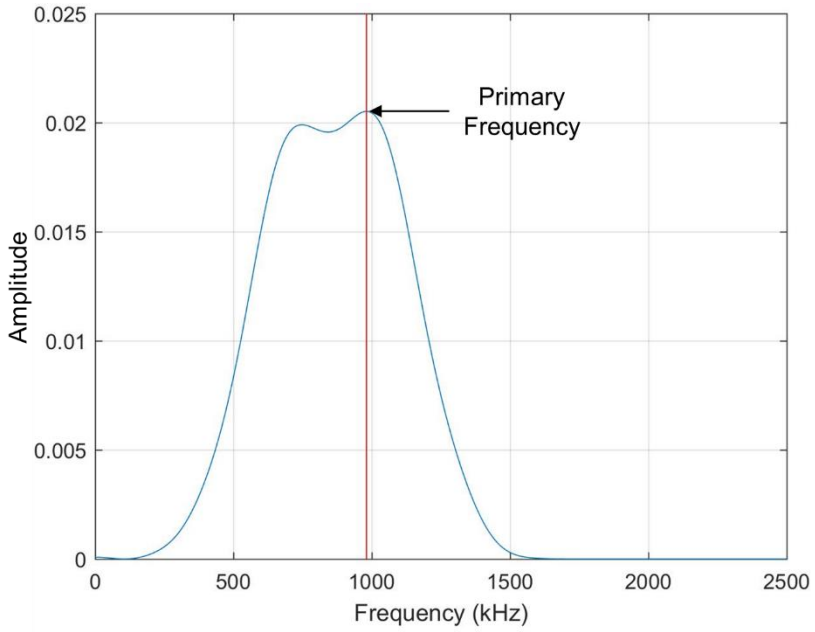

Figure 4.10 Frequency spectra of the waveform in Figure 4.9. The red line shows the peak frequency used in the analysis

The dominant frequency corresponding to the maximum amplitude in the frequency domain was determined. Figure 4.10 shows the frequency spectra for the waveform in Figure 4.9

obtained after an FFT on the 10 µs window. The primary frequency marked by the red line in Figure 4.10 corresponds to the amplitude peak in the spectra. Zones of intense microfractures would be associated with higher attenuation of waveforms and hence would be associated with low primary frequency. (Sondergeld and Estey, 1981).

A heatmap of the primary frequency of all the shear waveforms around the first arrival, similar to that of SWR map and shear velocity map, is plotted using Convergent interpolation method in Petrel 2016.

Figure 4.11 (a) and (b) shows the frequency heatmap (plan view) for shear wave polarization perpendicular and parallel respectively, to the direction of applied stress.

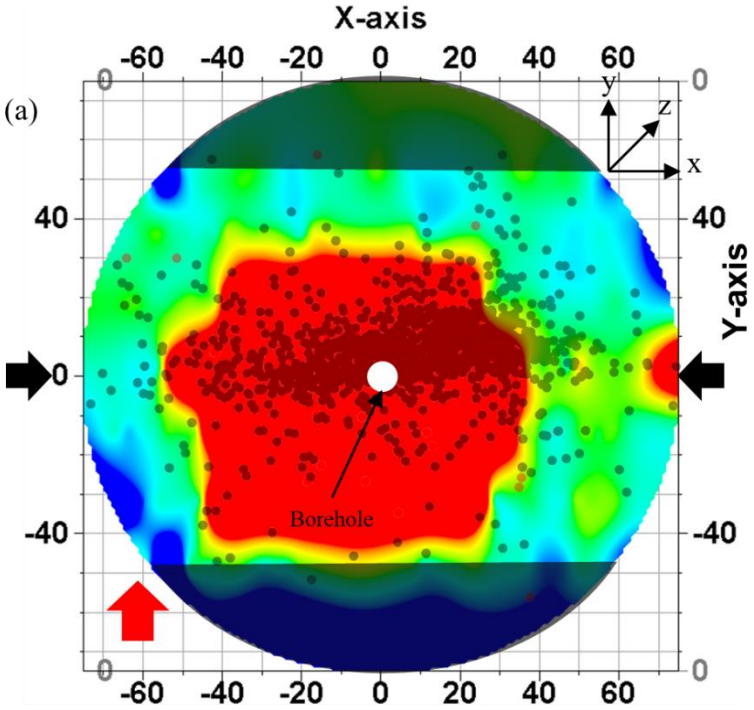

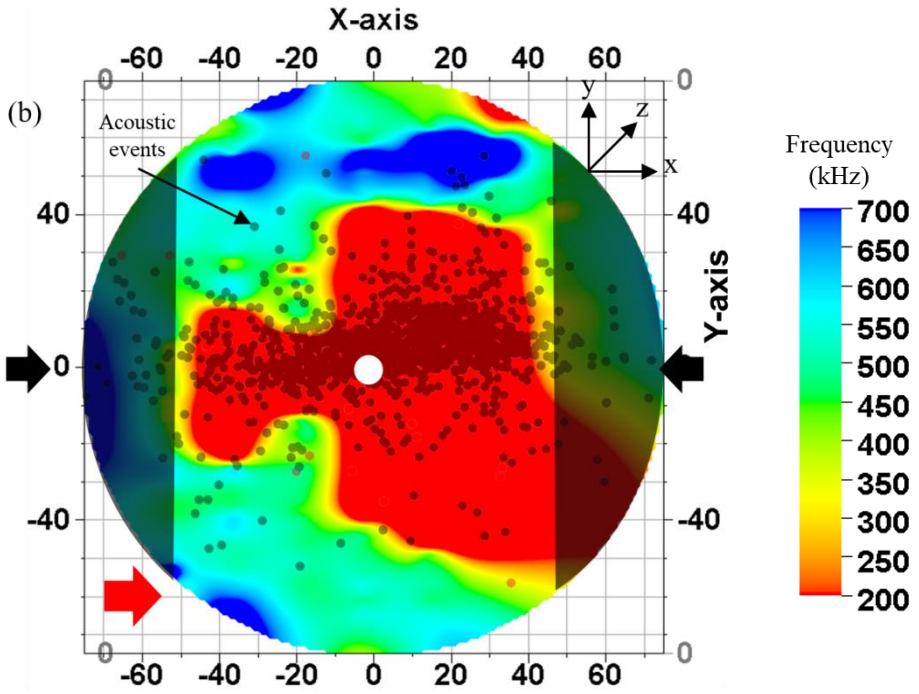

Figure 4.11 Frequency map for top surface of Tennessee sandstone TSU-6 sample. Shear wave propagation is along z-axis. Transducer polarizations denoted by the red arrow in (a) and (b). Shaded areas represent areas of no recorded data. AE event locations are superimposed on the map.

Hotter colors in the frequency heatmap in Figure 4.11 (a) and (b) represent lower primary frequency which can be associated with intense microfractures while cooler colors represent region with higher frequency or lower signal attenuation. Direction of the applied stress is indicated by the black arrows. Shaded regions in Figure 4.11 (a) and (b) are the regions where no shear wave data was recorded. Acoustic events are superimposed into the frequency map in Figure 4.11 (a) and (b) for comparison.

It is observed that the frequency map in Figure 4.11 is similar to the SWR map shown in Figure 4.4. The regions with higher SWR correlate directly with zones having lower primary frequency which supports the claim that the area is associated with intense microfractures. Additionally, the parallel and perpendicular polarization shear wave data in Figure 4.4 and Figure 4.11 show that there is presence of primary fractures as well as secondary fractures, as

already discussed in the SWR map analysis as well as observed by Ratzlaff (2018) in SEM fracture analysis in Tennessee sandstone.

As discussed in section 3.4.3, the sample is cut 0.5-inch from the sample boundaries parallel to the fracture plane and shear wave response is taken on the sides of the sample. Figure 4.5 shows the side view of the sample after it had been cut.

Frequency analysis for the recorded shear waveform is done after the sample was first cut 0.5-inch from the sample boundaries (Section 3.4.3) parallel to the fracture plane (See Figure 4.5). The frequency map is shown in Figure 4.12.

Figure 4.12 (a) and (b) show the frequency map for two orthogonal polarizations in the plane perpendicular to the fracture plane. The mapped area shown corresponds to the flat surface in Figure 4.5. The primary frequency appears uniform throughout the sample surface in the range 300 – 500 kHz with patches of higher and lower frequency areas. Frequency map is consistent with the V_s map in Figure 4.6.

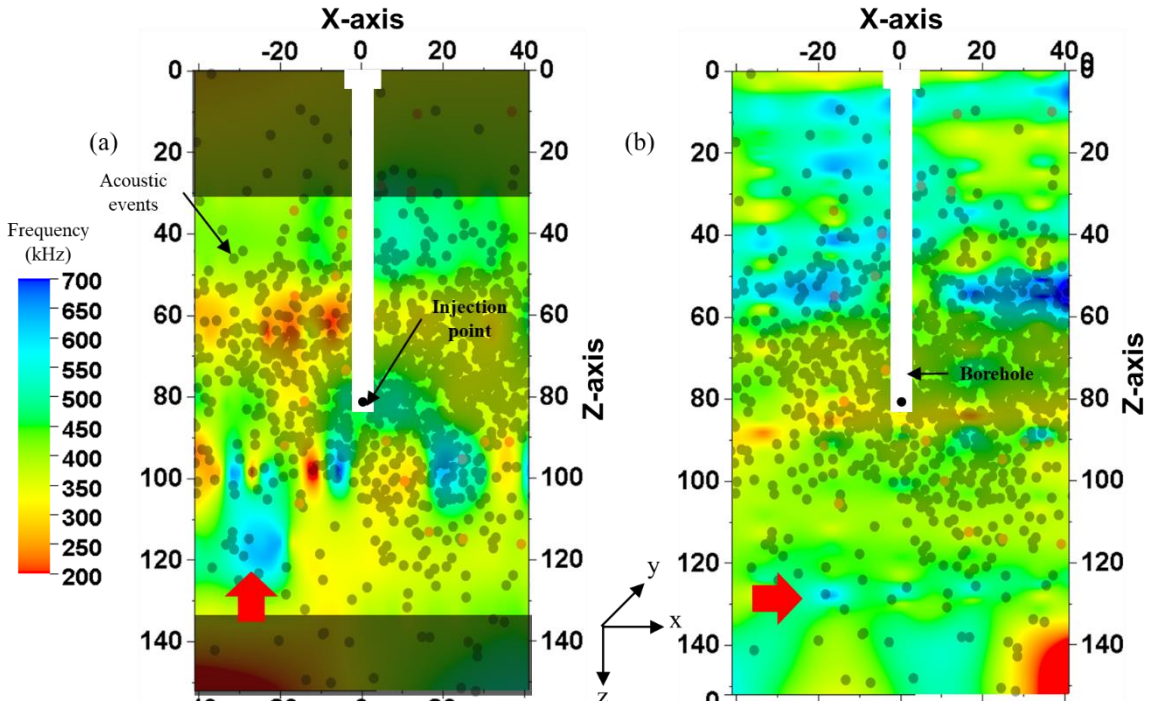

Figure 4.12 Dominant frequency map on Tennessee sandstone sample TSU-6 across sides parallel to fracture plane but with propagation through the main fracture. Shear wave propagation is along y-axis. (a) and (b): map for orthogonal transducer polarizations represented by red arrows. AE event locations are superimposed on the map. Shaded areas represent areas of no recorded data.

Frequency analysis for the recorded shear waveform is done for the sample cut 0.5-inch from sample circumference, normal to the fracture plane as discussed in section 3.4.3. The sample is cut as shown in Figure 3.25. The cut sample is shown in Figure 4.7and Figure 4.13 shows the frequency map.

The frequency map in Figure 4.13 is similar to the V_s map in Figure 4.8. The areas with low V_s have a low primary frequency (< 250 kHz) confirming presence of cracks and microfractures, allowing us to map the stimulated areas with more confidence. AE locations consequently have good correlation to the frequency map as well.

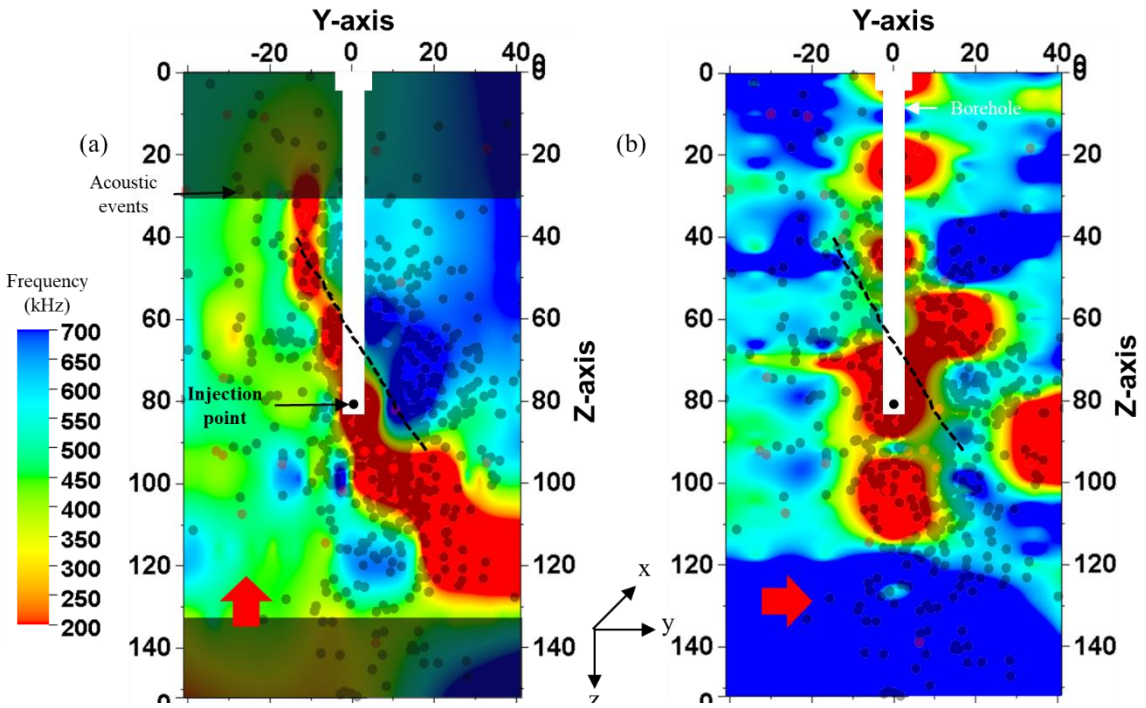

Figure 4.13 Dominant frequency map on Tennessee sandstone sample TSU-6 across sides normal to fracture plane. Shear wave propagation is along x-axis. (a) and (b): map for orthogonal transducer polarizations represented by red arrows. AE event locations are superimposed on the map. Fracture visible on surface shown by the black dotted line. Shaded areas represent areas of no recorded data.

(iii) Crack Density Analysis

Various methods have been proposed to make a rough estimation of the crack density in a rock sample. One of the methods chosen for this work is O'Connell and Budiansky Self-Consistent Model (O' Connell and Budiansky, 1974) which is used to relate the shear wave velocity to the crack density. The model proposes a relation between the ratio of G_{dry} and G_{grain} to the crack density in the rock sample as shown in Figure 4.14. G_{dry} is the dry porous frame shear modulus of the rock sample; G_{grain} is the gain shear modulus of the rock sample.

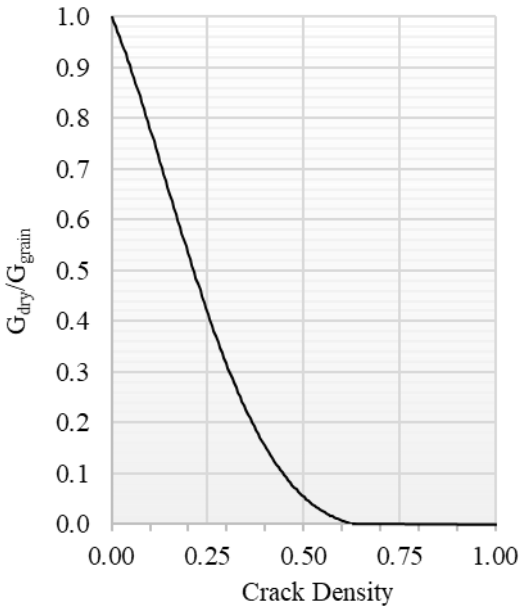

Figure 4.14 O'Connell and Budiansky Self-Consistent Model. (O' Connell and Budiansky, 1974)

The crack density defined in the model is not the standard crack density as understood in the industry. It is defined as some measure of the area of surface in contact. When crack density (ε) = 1, the crack cuts through all the four faces of the sample. A schematic of the crack density with respect to a sample surface is shown in Figure 4.15. Lower value of ε shows low or no cracks cutting the surface of the sample area.

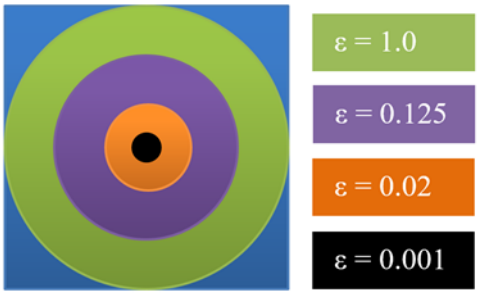

Figure 4.15 Schematic of crack density definition as per O'Connell and Budiansky Self-Consistent Model. When ε = 1, the crack cuts through all four faces.

The ratio G_{dry}/G_{grain} is calculated using equation (4-10) (Bhoumick et al., 2017):

$$\frac{G_{dry}}{G_{grain}} = \frac{\rho(1-\varphi)V_s^2}{G_{rock\ sample}} \quad (4\text{-}10)$$

where G_{dry} is the dry porous frame shear modulus of the rock sample; G_{grain} is the gain shear modulus of the rock sample; ρ is the bulk density of the rock sample; φ is the porosity in pu; V_s is the calculated shear wave velocity of the sample using the measured shear wave travel time.

For Tennessee sandstone, ρ = 2.65 g/cc; φ = 0.06 pu; G = 44 GPa. Figure 4.16 (a) and (b) shows the crack density heatmap (plan view) for shear wave polarization perpendicular and parallel respectively, to the direction of applied stress.

Hotter colors in the crack density heatmap in Figure 4.16 (a) and (b) represent higher crack density which can be associated with intense microfractures while cooler colors represent region with lower crack density. Direction of the applied stress is indicated by the black arrows. Shaded regions in Figure 4.16 (a) and (b) are the regions where no shear wave data was recorded. Acoustic events are superimposed into the crack density map in Figure 4.16 (a) and (b) for comparison.

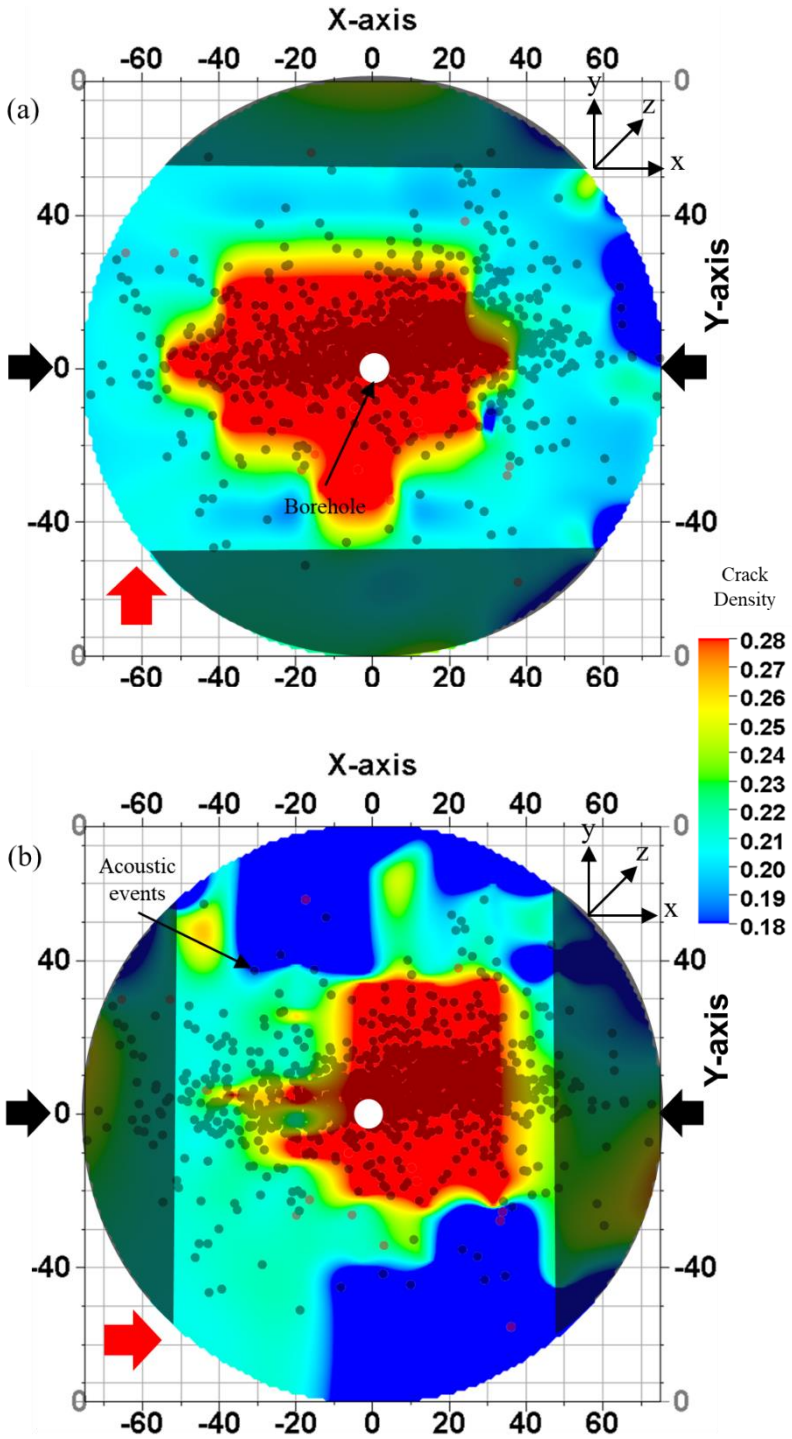

Figure 4.16 Crack density map for top surface of Tennessee sandstone TSU-6 sample. Shear wave propagation is along z-axis. Transducer polarizations denoted by the red arrow in (a) and (b). Shaded areas represent areas of no recorded data. AE event locations are superimposed on the map.

It is observed that the crack density map in Figure 4.16 is similar to the SWR map shown in Figure 4.4. The regions with higher SWR correlate directly with zones having higher crack density which supports the claim that the area is associated with intense microfractures. Additionally, the parallel and perpendicular polarization crack density maps in Figure 4.16 reinforce the presence of primary fractures as well as secondary fractures, as already discussed in the SWR and frequency map analysis.

As discussed in section 3.4.3, the sample is cut 0.5-inch from the sample boundaries parallel to the fracture plane and shear wave response is taken on the sides of the sample. Figure 4.5 shows the side view of the sample after it had been cut.

Crack density analysis for the recorded shear waveform is done after the sample was first cut 0.5-inch from the sample boundaries (Section 3.4.3) parallel to the fracture plane (See Figure 4.5). The crack density map is shown in Figure 4.17.

Figure 4.17 (a) and (b) show the crack density map for two orthogonal polarizations in the plane perpendicular to the fracture plane. The mapped area shown corresponds to the flat surface in Figure 4.5. The crack density appears uniform throughout the sample surface in the range 0.19 - 0.22 with patches of higher and lower crack density areas. Crack density map is consistent with the V_s map in Figure 4.6 as well as frequency map in Figure 4.12.

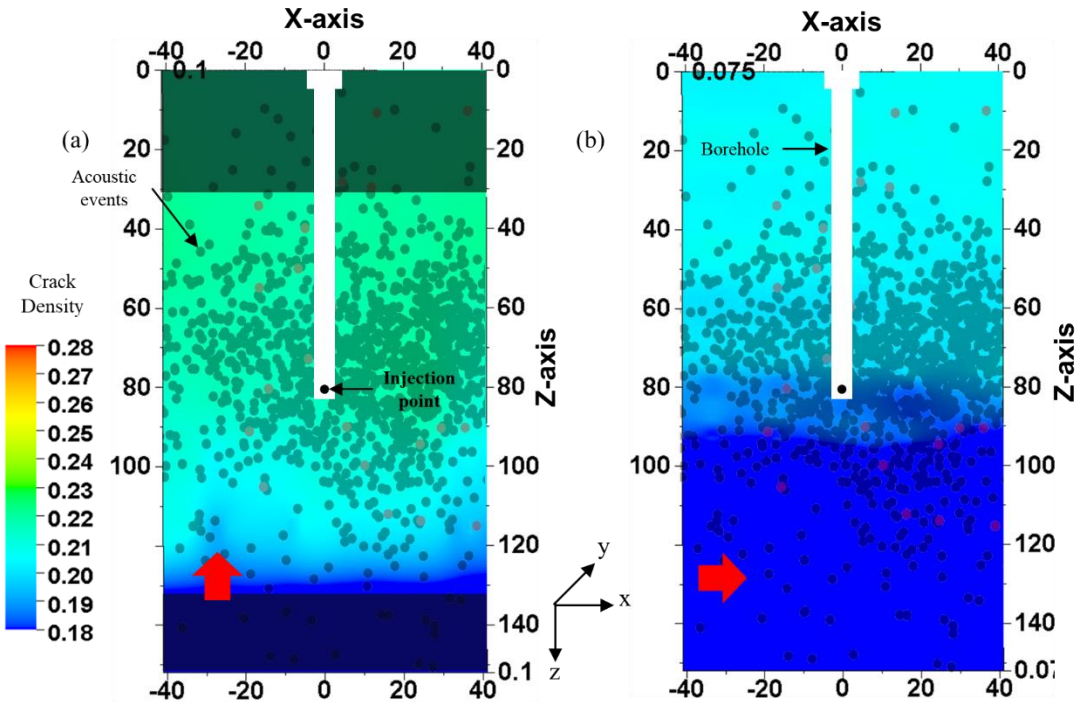

Figure 4.17 Crack density map on Tennessee sandstone sample TSU-6 across sides parallel to fracture plane but with propagation through the main fracture. Shear wave propagation is along y-axis. (a) and (b): map for orthogonal transducer polarizations represented by red arrows. AE event locations are superimposed on the map. Shaded areas represent areas of no recorded data.

Crack density analysis for the recorded shear waveform is done for the sample cut 0.5-inch from sample circumference, normal to the fracture plane as discussed in section 3.4.3. The sample is cut as shown in Figure 3.25. The cut sample is shown in Figure 4.7 and Figure 4.18 shows the crack density map.

The crack density map in Figure 4.18 is similar to the V_s map in Figure 4.8. The areas with low V_s have a higher crack density (≥ 0.28) confirm the presence of cracks and microfractures, allowing us to map the stimulated areas with more confidence. AE locations consequently have good correlation to the crack density map as well.

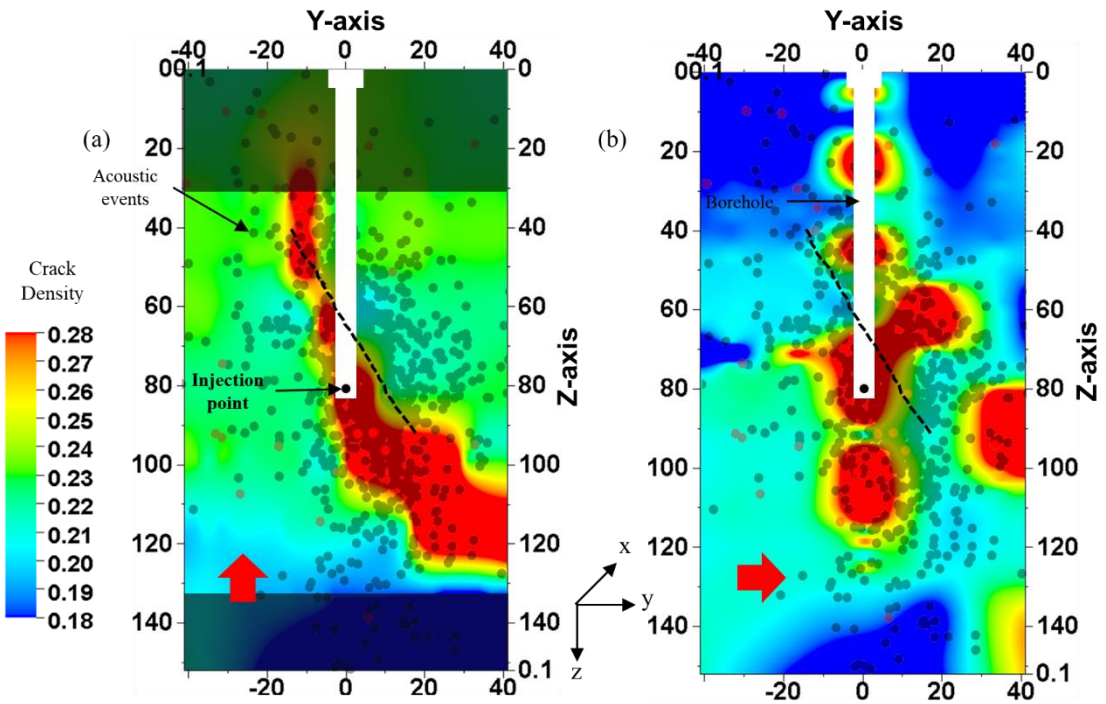

Figure 4.18 Crack density map on Tennessee sandstone sample TSU-6 across sides normal to fracture plane. Shear wave propagation is along x-axis. (a) and (b): map for orthogonal transducer polarizations represented by red arrows. AE event locations are superimposed on the map. Fracture visible on surface shown by the black dotted line. Shaded areas represent areas of no recorded data.

In summary, shear wave velocity, frequency and crack density analysis are complementary in defining induced microfractures and consequently the probable SRV zone. AE event locations are also consistent with velocity, crack density and frequency analysis.

4.2 Pyrophyllite

Pyrophyllite is a fine grained monomineralic metamorphic rock formed of the mineral pyrophyllite which is structurally similar to illite, but the rock does not have organic content and lacks the mechanical fragility and reactivity of clays. It is a member of the illite family; an analogy for natural shale. Pyrophyllite is an ideal substitute for shale, for this study. Agrawal (2012) reported the measured permeability of pyrophyllite as 140 ± 45 nd at 1000 psi confining pressure.

CVA analysis on pyrophyllite (See Figure 3.3, Figure 3.4) reveal a P-wave anisotropy of up to 20%. Two uniaxial hydraulic fracturing tests were performed on pyrophyllite samples as summarized in Table 4-2. One of the samples was fractured using water (1 cP) and the other using oil (50 cP), injected at a constant rate of 15 cc/min.

Table 4-2 Uniaxial hydraulic fracture test parameters on pyrophyllite (horizontal cores)

Sample ID	Stress (psi)	Fracturing fluid	Viscosity (cP)	Flow rate (cc/min)	Breakdown Pressure (psi)	Located AE/Good AE
PY-1	840	Water	1	15	1924	98/411
PY-2	820	Oil	50	15	3790	51/196

4.2.1 Pressure and AE response

(a) PY-1

This sample was fractured using water (1 cP) as injection fluid. The effective applied stress was 840 psi perpendicular to the direction of the foliation as determined by CVA (See Figure 3.3). Figure 4.19 shows the pump pressure (black markers) and the acoustic emission count (blue markers) recorded as a function of time. Pressure increases rapidly at 485 psi/s up till the breakdown pressure of 1924 psi when the rock failed. Following the breakdown, the pressure rapidly dropped at the rate of 2604 psi/s, finally stabilizing to a pressure of 860 psi.

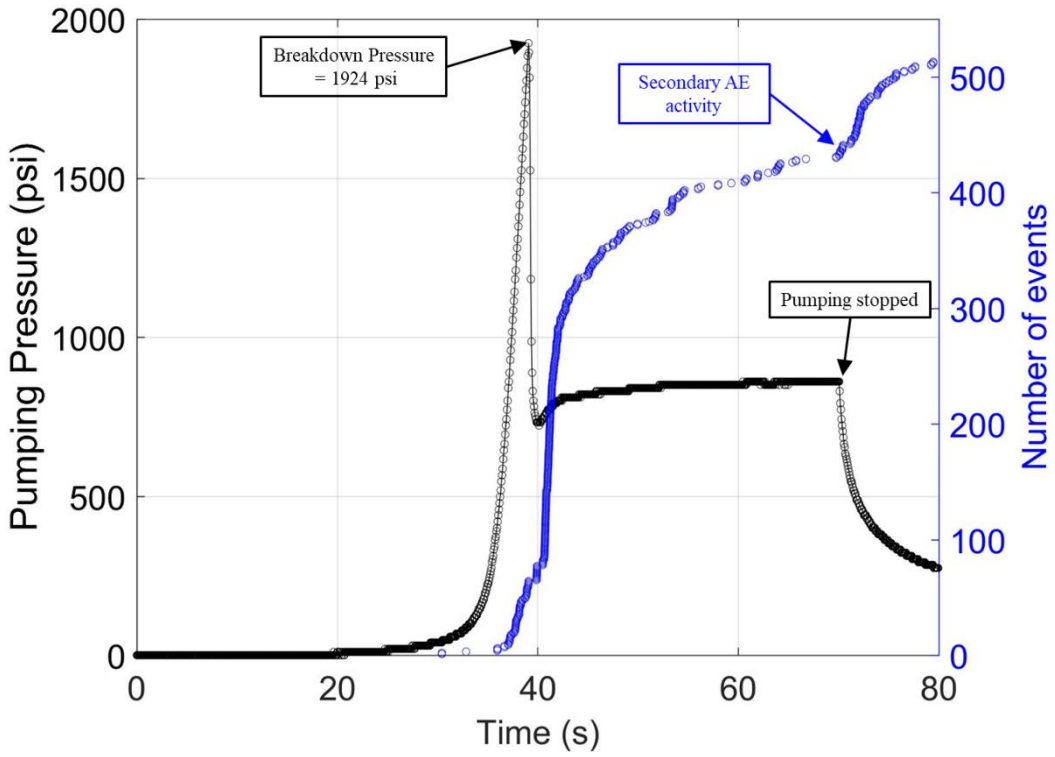

Figure 4.19 Injection pressure (black markers) and acoustic event (blue markers) is plotted as a function of time for pyrophyllite sample, PY-1. Most events are associated with pre-breakdown and breakdown. Note there is a factor of 6 between the number of events recorded for Tennessee sandstone and pyrophyllite.

A total of 513 acoustic events were recorded. It is observed that AE activity begins before the breakdown occurs. There is no distinct gap between pre-breakdown and post-breakdown in AE as was in the case of Tennessee sandstone, since not as many events are recorded during PY-1 fracturing and the system does not become saturated with the event recordings during breakdown. The AE rate decreased once the fracture wings are developed.

After the injection was stopped, a rapid burst of secondary AE was observed. It may be due to the failure of the asperities associated with fracture closure when the injection is stopped (Chitrala, 2011), which is a similar signature noticed in the Tennessee sandstone fracturing test as well.

(b) PY-2

The sample was fractured using oil with a viscosity of 50 cP as injection fluid. The effective applied stress was 840 psi perpendicular to the direction of the foliation as determined by CVA (See Figure 3.4). Figure 4.20 shows the pump pressure (black markers) and the acoustic emission count (blue markers) recorded as a function of time. Pressure increases rapidly at 597 psi/s up till the breakdown pressure of 3790 psi when the rock failed. Following the breakdown, the pressure rapidly dropped at the rate of 3600 psi/s, finally stabilizing to a pressure of 780 psi.

A total of 219 acoustic events were recorded. It is observed that AE activity begins before the breakdown occurs. As was the case for sample PY-1, most of the events are associated with pre-breakdown and breakdown. There is no distinct gap between pre-breakdown and post-breakdown in AE. There are far fewer events recorded post-breakdown than in PY-1.

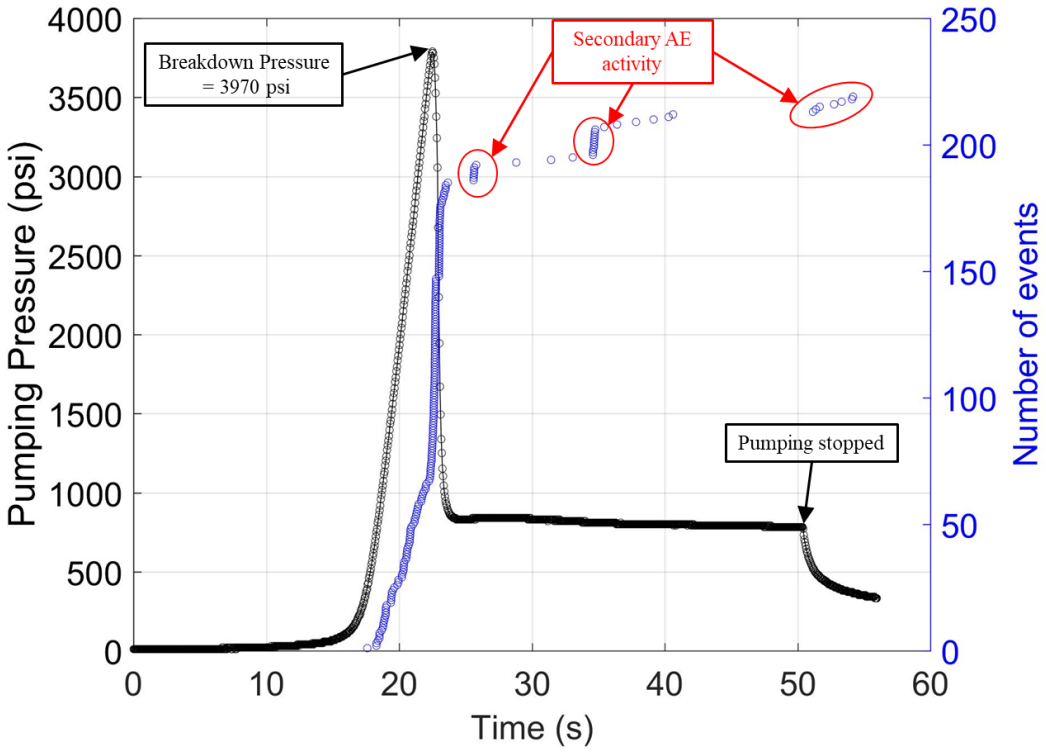

Figure 4.20 Injection pressure (black markers) and acoustic event (blue markers) is plotted as a function of time for pyrophyllite sample, PY-2. Most events are associated with pre-breakdown and breakdown. There are bursts of secondary AE after breakdown

After the injection was stopped, multiple rapid bursts of secondary AE were observed. Few secondary AE are recorded once the injection stopped. All the bursts of secondary AE happen due to the failure of the asperities associated with fracture closure.

The results suggest that breakdown pressure is lower in pyrophyllite as compared to Tennessee sandstone when fractured using water as injection fluid. However, when a more viscous fluid such as oil is used in place of water for fracturing, pyrophyllite exhibit far higher breakdown pressure. The total number of acoustic events detected is far fewer in pyrophyllite as compared to Tennessee sandstone. It is even less in pyrophyllite when oil is used as injection fluid compared to when water is used. This lower energy associated with failure events in pyrophyllite is probably due to its small grain size i.e. < 4µm which results in smaller shear

slippage along grain boundaries in comparison to sandstone (grain size ≈ 190 μm) (Damani, 2013).

4.2.2 Fracture Orientation and AE Location

(a) PY-1

The effective uniaxial stress on the sample during fracturing was 840 psi, applied perpendicular to the bedding in the rock. There is evidence of fracture wings extending from one side of the wellbore to the other side inclined at an angle of 9^{o} to the bedding plane direction which is determined from CVA (See Figure 3.3), as shown in Figure 4.21. The fracture propagation is not symmetrical around the borehole. A uniaxial stress of 840 psi was not sufficient to orient the fracture to the direction of the maximum stress, though it made the fracture propagate at an angle to the bedding plane. Elastic anisotropy of the rock seems to be dominant in controlling the fracture orientation overcoming the stress applied perpendicular to the bedding direction. Also, the fracture traverses inclined to the vertical along the Z axis visible only on one of the fracture wings (see Figure 4.21 (b)).

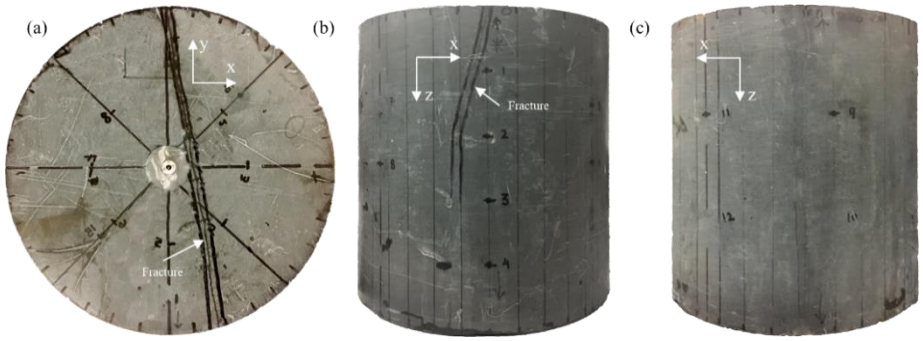

Figure 4.21 Surface observation of induced hydraulic fracture on PY-1: (a) plan view; (b) and (c) side view (Sample length–152.6 mm; Diameter–152.6 mm)

A total of 411 good and detectable first arrival acoustic events were recorded on at least 8 out of 16 sensors out of which only 98 events could be located inside the sample using anisotropic

velocity model (See Table 4-2). Figure 4.22 shows the side (Figure 4.22 a, b) and the plan (Figure 4.22 c) views of the located AE. Events occurring before the breakdown are marked with red dots and the post-breakdown events are shown with black dots. A total of 32 AE events were located pre-and during breakdown, and 66 AE events were located post-breakdown. In general, the distribution in Figure 4.22 (c) align with the observed fracture trace on the sample. The average error in hypocenter locations for this test was $\pm$7.2 mm.

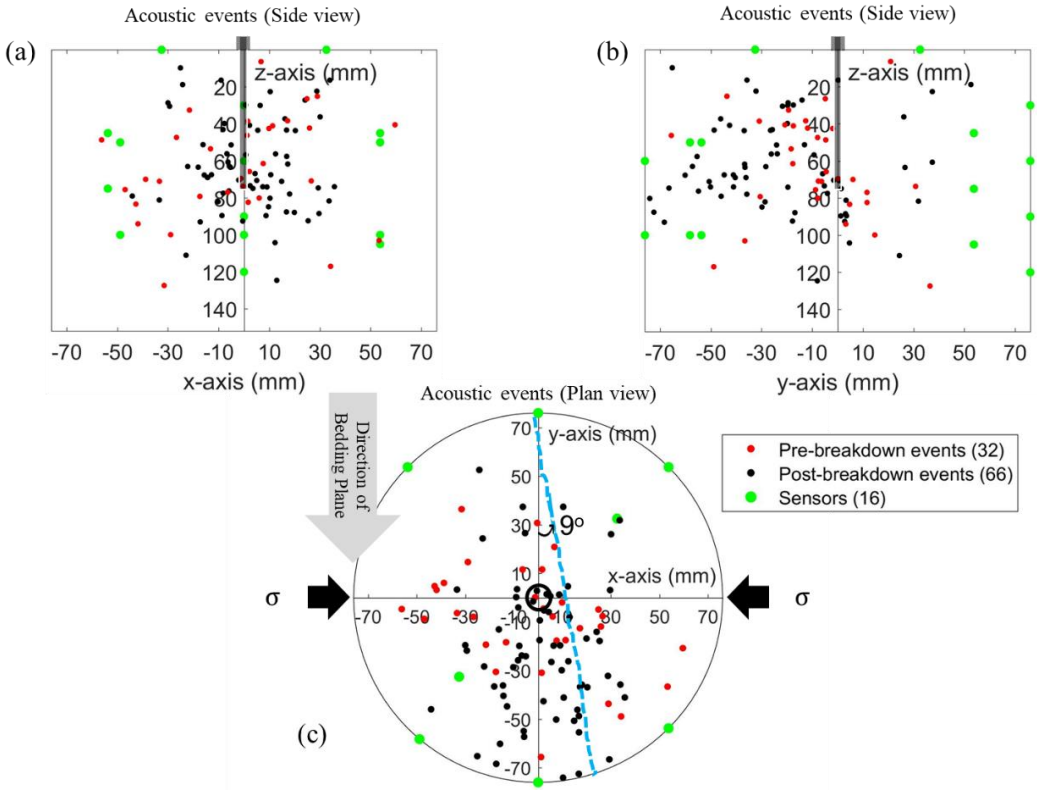

Figure 4.22 Plot of AE for fractured pyrophyllite sample PY-1, fractured under uniaxial stress of 840 psi (shown by black arrows in plan view). Pre-breakdown events shown in red circles and post-breakdown events in black circles; (a) and (b) lateral views of AE; (c) plan view of AE hypocenter; broken blue line shows the actual fracture trace visible on sample top surface

(b) PY-2

The effective uniaxial stress on the sample during fracturing was 820 psi, applied perpendicular to the bedding in the rock. In Figure 4.23, two fracture wings were visible on surface sample, inclined at an angle of approximately 20^{o} to the bedding plane direction, as shown in Figure 4.23. The fracture is not symmetrical about the borehole. A uniaxial stress of 820 psi was not sufficient to orient the direction of the fracture in the direction of the maximum stress, though it made the fracture propagation at an angle to the bedding plane. Like PY-1, the elastic anisotropy of PY-2 also dictated the direction of fracture propagation overcoming the applied stress perpendicular to the bedding plane. Also, the fracture traverses inclined to the vertical along the Z axis on both the fracture wings (see Figure 4.23 (b) and (c)).

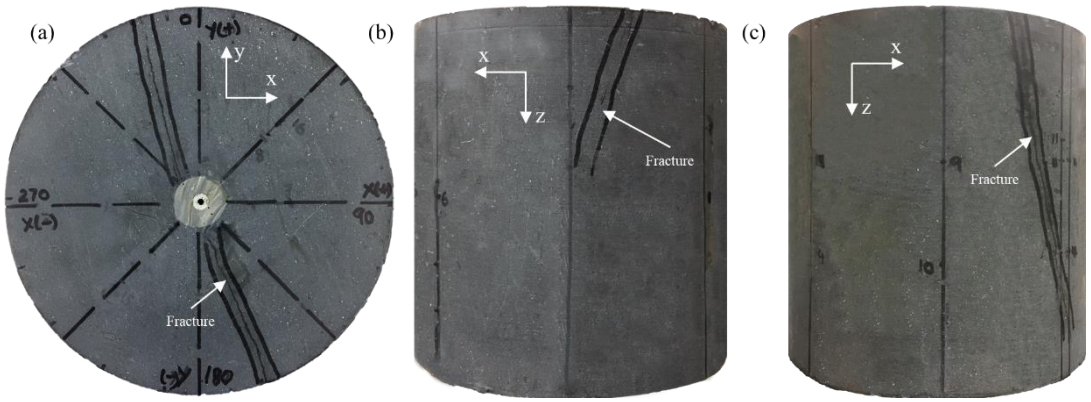

Figure 4.23 Surface observation of induced hydraulic fracture on PY-2: (a) plan view; (b) and (c) side view (Sample length – 152.5 mm; Diameter – 152.5 mm)

A total of 196 good and detectable first arrival acoustic events were recorded on at least 8 out of 16 sensors; out of which only 51 events could be located inside the sample (See Table 4-2). Figure 4.24 shows side (Figure 4.24 a, b) and the plan (Figure 4.24 c) views of the located AE. Events occurring before the breakdown are marked in red dots and the post-breakdown events are shown in black dots. Majority of the events happen during pre-breakdown and breakdown

(30 events) with no clear distinction between pre- and post-breakdown events (21 events), as discussed in section 4.2.1 (b). The AE distribution in Figure 4.24 (c) do not align with the observed fracture trace on the sample. Limited number of AE events precludes accurate mapping of the fracture plane.

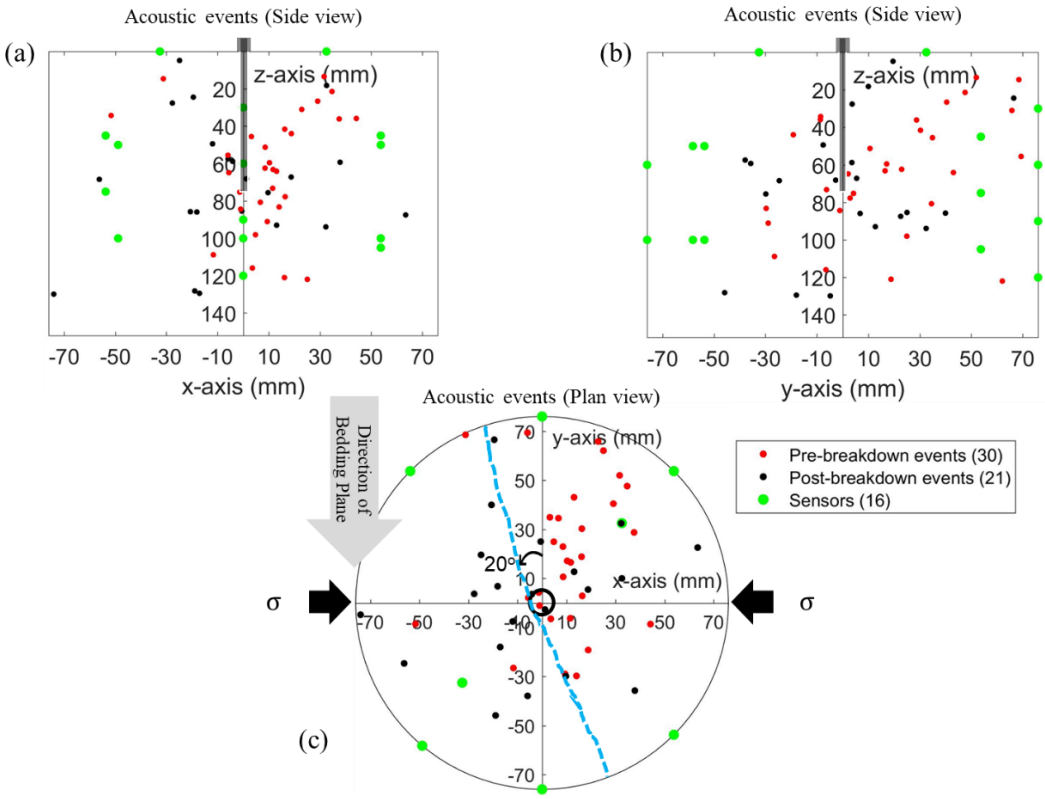

Figure 4.24 Plot of AE for fractured pyrophyllite sample PY-2, fractured under uniaxial stress of 840 psi (shown by black arrows in plan view). Pre-breakdown events shown in red circles and post-breakdown events in black circles; (a) and (b) lateral views of AE; (c) plan view of AE hypocenter; broken blue line shows the actual fracture trace visible on sample top surface

4.2.3 Shear Wave Response

(a) PY-1

(i) Shear Wave Velocity Analysis

Figure 4.25 (a) and (b) shows the SWR heatmap for shear wave polarization parallel and perpendicular respectively, to the direction of the rock fabric determined from CVA (See Figure 3.3) for top surface. Direction of rock fabric is parallel to the y-axis. Acoustic events are superimposed onto the SWR map for comparison. Fracture outline visible on the sample surface is marked by the red dashed line.

Figure 4.25 (a) represents the SWR map for transducers parallel polarization to the rock fabric direction. Shear wave would be slowed by presence of cracks and microfractures perpendicular to the polarization direction. A maximum of 30% slowness in shear wave is observed. Hotter colors in Figure 4.25 (a) represent the slowness in shear wave due to induced primary fractures. It is observed that the hotter color (higher SWR) do not align with the actual fracture visible on the sample top surface. It is because the fracture is inclined in the sample as can be seen in the lateral view in Figure 4.21 (b). Only one of fracture wings (in the negative Y axis) could be distinctly identified by the SWR map.

Figure 4.25 (b) represent the SWR map for transducer perpendicular to the rock fabric direction. There is a maximum of 28% slowness in shear wave observed showing strong slowness in the zone. The SWR map in the figure shows the presence of secondary fractures.

The SWR map show a similar trend as the AE locations.

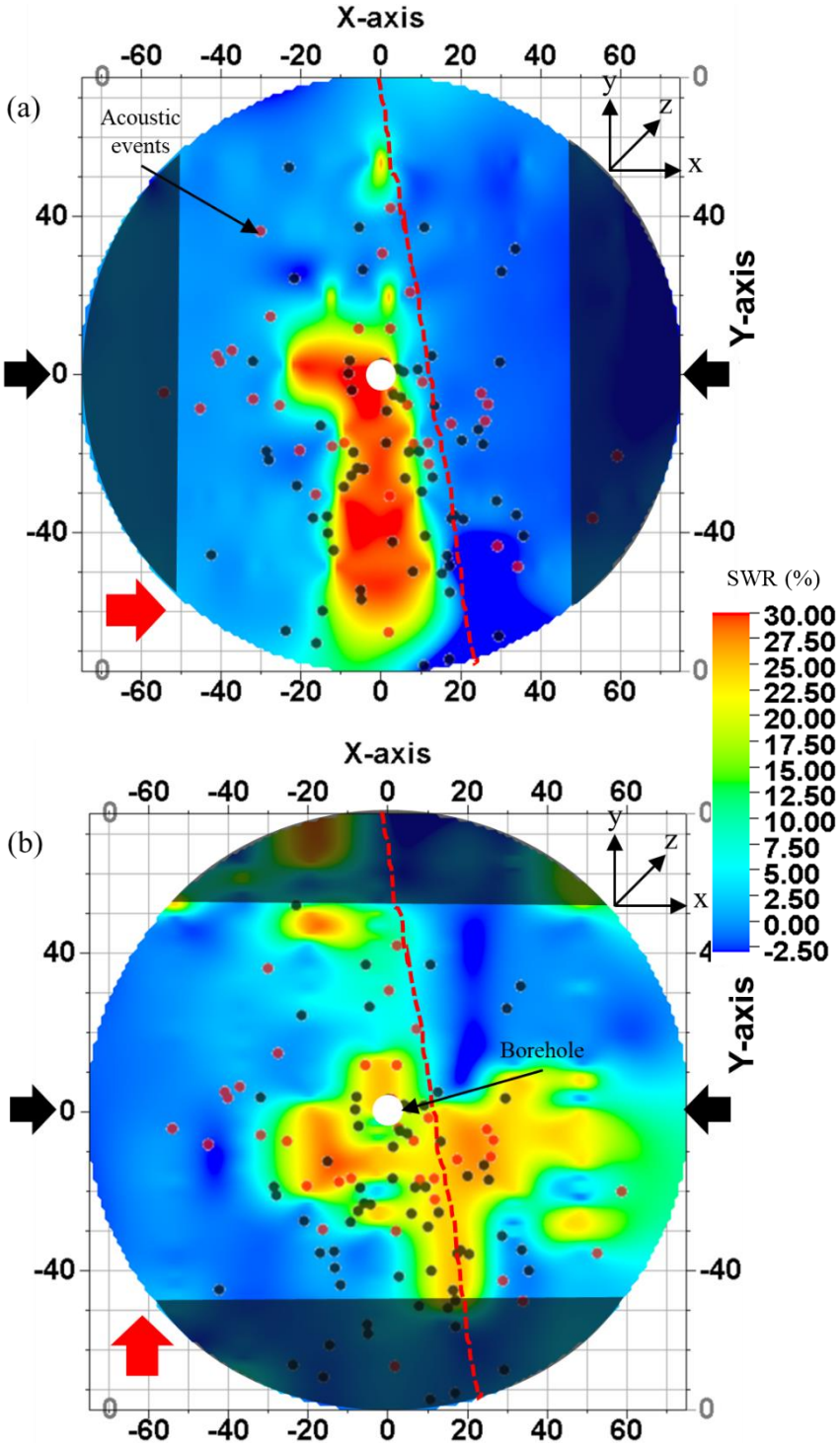

Figure 4.25 SWR map for top surface of pyrophyllite PY-1 sample. Shear wave propagation is along z-axis. Transducer polarizations denoted by the red arrow in (a) and (b). Shaded areas represent areas of no recorded data. AE event locations superimposed on the map. Red dashed lines represent fracture physically visible on sample top surface

Negative SWR is due to associated measurement error (± 3%) represented by the darker shades of blue color in the heatmap.

As discussed in section 3.4.3, the sample is cut 0.5-inch from the sample boundaries parallel to the fracture plane and shear wave response is measured across the sides of the sample. Figure 4.26 shows the side view of the sample after it had been cut.

Figure 4.26 Side view of sample PY-1, cut as per Figure 3.22

Shear wave response was not recorded on the sides before fracturing. Hence, it is not possible to generate SWR map, however, the shear wave velocity (V_s) across the core is analyzed for two orthogonal transducer polarizations. Figure 4.6 (a) and (b) show the V_s map for two orthogonal polarizations in the plane parallel to the fracture plane. The mapped area shown corresponds to the flat surface in Figure 4.26. The transducer polarizations are marked with the red arrow in each figure. Regions where no data is recorded is shaded.

The cooler colors in the map represent faster V_s while the warmer colors represent slower V_s (opposite of what people associate with these colors) It is observed in Figure 4.27 (a), for

polarization directed vertically, parallel to the Z axis (as shown by red arrow), the V_s is in the range 2.47 – 2.49 km/s.

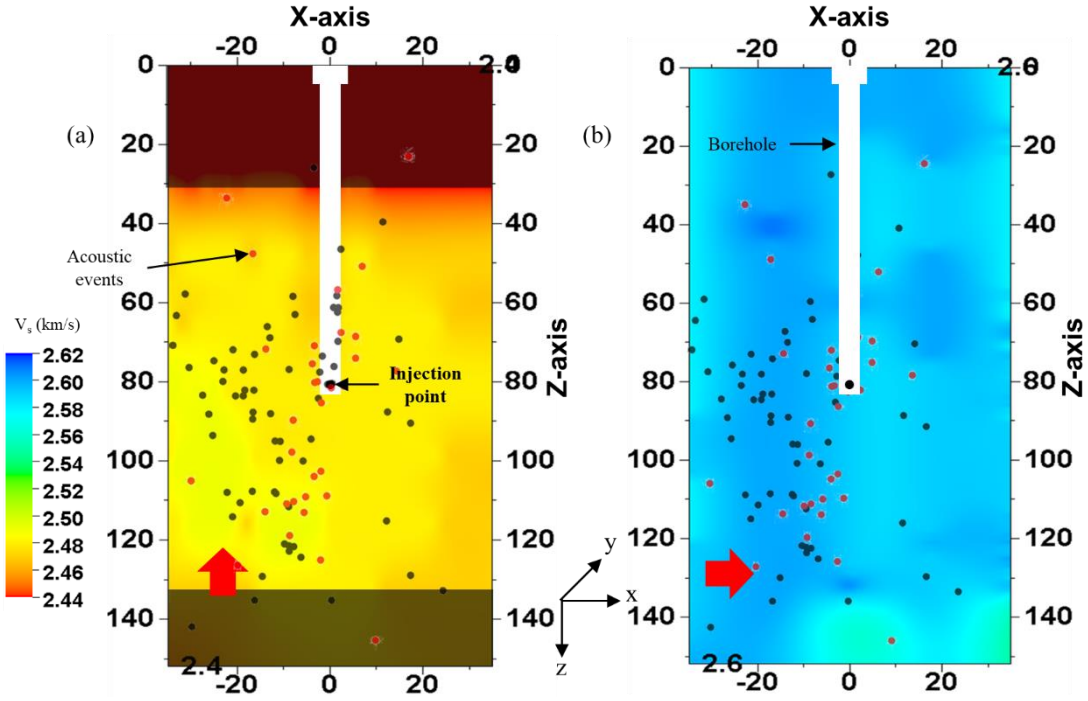

Figure 4.27 Shear velocity map on pyrophyllite sample PY-1 across the sides parallel to fracture plane. Shear wave propagation is along y-axis. (a) and (b): map for orthogonal transducer polarizations represented by red arrows. AE event locations are superimposed on the map. Shaded areas represent areas of no recorded data.

In Figure 4.27 (b), transducer polarization directed horizontally i.e. parallel to the X axis, in the plane (as shown by red arrow). V_s is in the range 2.57 – 2.62 km/s, throughout the sample space shown. V_s is 6% slower for z-axis polarization compared to the z-axis polarization in Figure 4.27 (a) although shear wave is polarized perpendicular to the plane of the fracture in both the cases. This can be attributed to presence of inclined fracture with respect to the direction of shear wave propagation. Secondly, it can also be due to the presence of secondary microfractures normal to the primary fractures in the horizontal plane, similar to the observation in Tennessee sandstone sample.

The sample was damaged before it could be cut on the other side as shown in Figure 4.7. The data is not available for analysis.

(ii) Shear Wave Frequency Analysis

Spectral analysis of the shear waveforms was carried out by using FFT performed on a ±5 µs window centered on the first arrival of the shear wave, as explained in section 4.1.4 (b).

A heatmap of the primary frequency of all the shear waveforms around the first arrival, similar to that of SWR map and shear velocity map, is plotted using convergent interpolation method in Petrel 2016.

Figure 4.28 (a) and (b) shows the frequency heatmap for the pyrophyllite sample PY-1, for shear wave polarization parallel and perpendicular respectively, to the direction of the rock fabric determined from CVA (See Figure 3.3) for top surface.

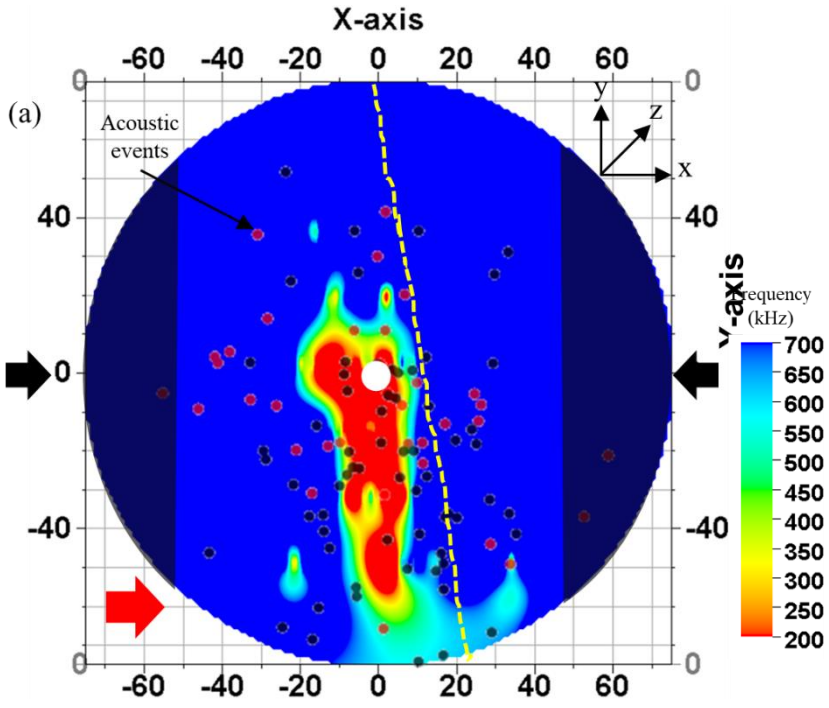

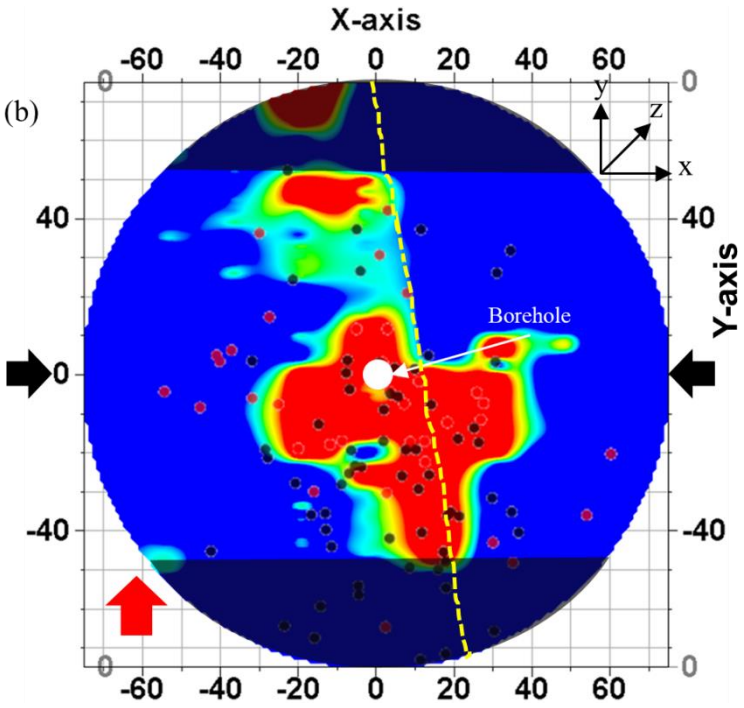

Figure 4.28 Dominant frequency map for top surface of pyrophyllite PY-1 sample. Shear wave propagation is along z-axis. Transducer polarizations denoted by the red arrow in (a) and (b). Shaded areas represent areas of no recorded data. Red (pre-breakdown) and black (post-breakdown) dots represent the superimposed AE event recorded during fracturing. Yellow dashed lines represent fracture physically visible on sample top surface

Hotter colors in the heatmap in Figure 4.28 (a) and (b) represent lower primary frequency or higher signal attenuation which can be associated with microfractures while cooler colors represent region with higher frequency. Direction of the applied stress is indicated by the black arrows. Shaded regions in Figure 4.28 (a) and (b) are the regions where no shear wave data was recorded. Acoustic events are superimposed onto the frequency map for comparison.

The frequency map in Figure 4.28 is similar to the SWR map shown in Figure 4.25. The regions with higher SWR correlate directly with zones having lower primary frequency which strengthens the observation that the area is associated with intense microfractures. Additionally, frequency map for the two polarizations in Figure 4.25 and Figure 4.28 show

that there is presence of primary fractures as well as secondary fractures, as already discussed in the SWR map analysis.

Frequency analysis for the recorded shear waveform is done after the sample was cut 0.5-inch from the sample boundaries (Section 3.4.3) parallel to the fracture plane (See Figure 4.5). The frequency map is shown in Figure 4.29. Figure 4.29 (a) and (b) show the frequency map for two orthogonal shear wave polarizations in the plane parallel to the fracture plane. The primary frequency is consistently above 700 kHz throughout the map for both the polarizations. The frequency map does not show the contrast as seen in the V_s map (as shown in Figure 4.27) where the two polarizations have varying shear velocity responses.

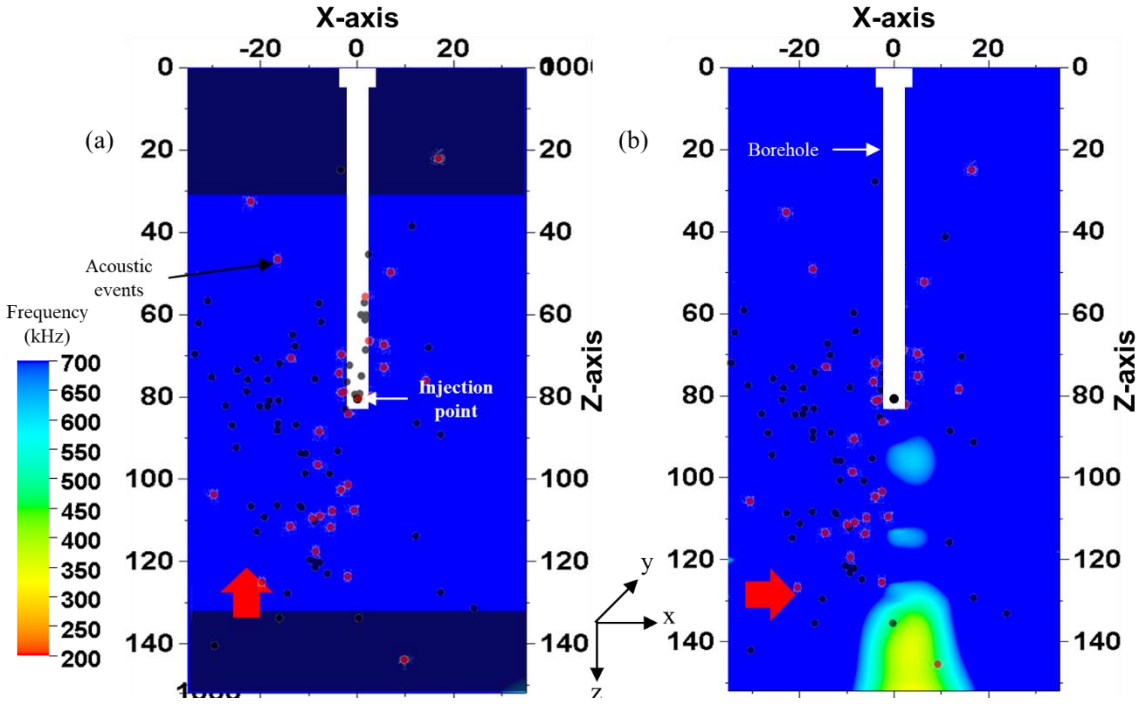

Figure 4.29 Dominant frequency map on pyrophyllite sample PY-1 across the sides parallel to fracture plane. Shear wave propagation is along y-axis. (a) and (b): map for orthogonal transducer polarizations represented by red arrows. AE event locations are superimposed on the map. Shaded areas represent areas of no recorded data.

(iii) Crack Density Analysis

Crack density analysis of the shear waveform is carried out using the O' Connell and Budiansky Self-Consistent model (O' Connell and Budiansky, 1974), as explained in section 4.1.4 (iii).

For pyrophyllite, the ratio of G_{dry} and G_{grain} is calculated using ρ = 2.84 g/cc; φ = 0.02 pu; G = 8 GPa. For pyrophyllite sample, PY-1, Figure 4.30 (a) and (b) shows the crack density heatmap (plan view) for shear wave polarization perpendicular and parallel respectively, to the direction of applied stress.

Hotter colors in the crack density heatmap in Figure 4.30 (a) and (b) represent higher crack density which can be associated with intense microfractures while cooler colors represent region with lower crack density. Direction of the applied stress is indicated by the black arrows. Shaded regions in Figure 4.30 (a) and (b) are the regions where no shear wave data was recorded. Acoustic events are superimposed into the frequency map in Figure 4.30 (a) and (b) for comparison.

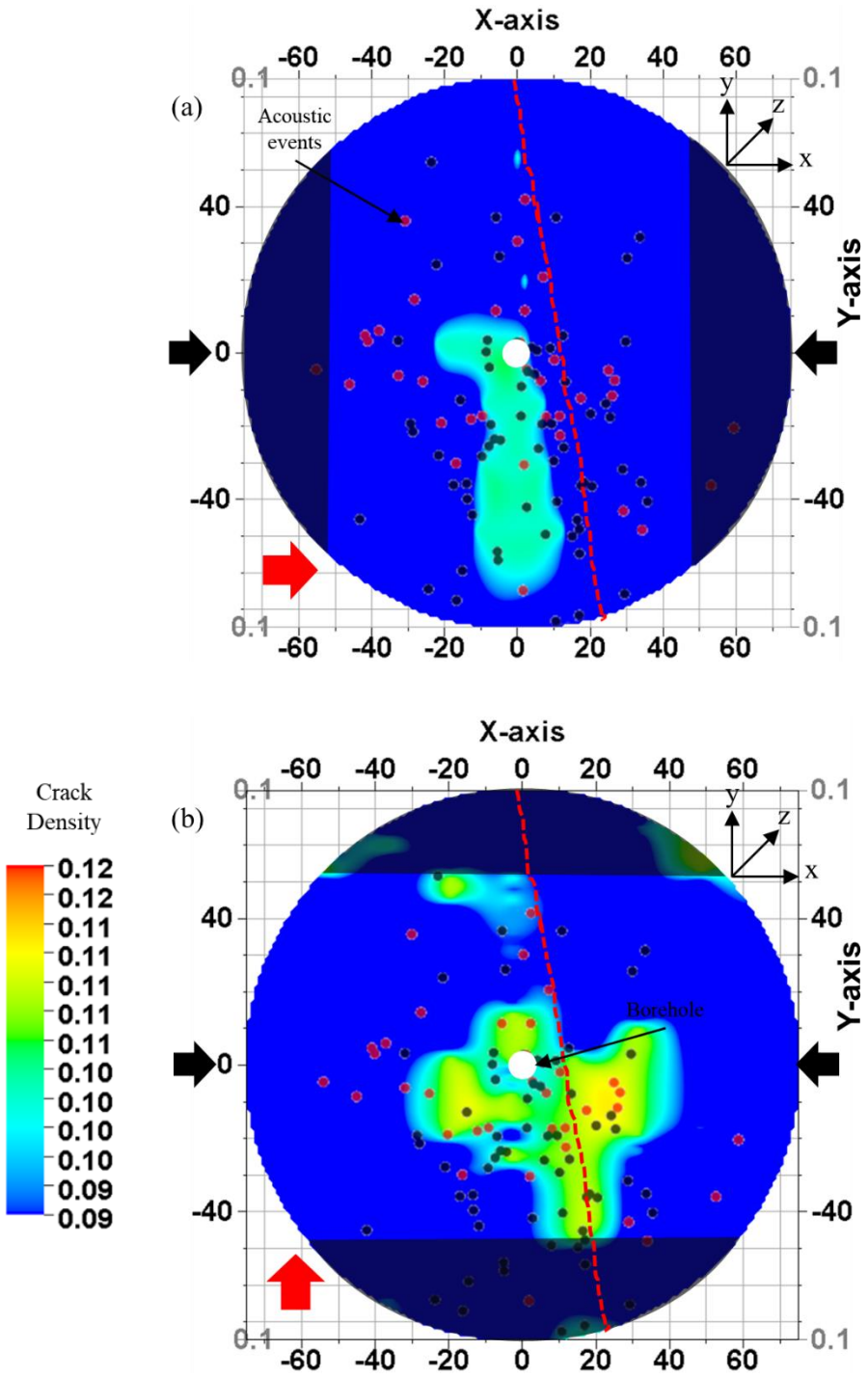

Figure 4.30 Crack density map for top surface of pyrophyllite PY-1 sample. Shear wave propagation is along z-axis. Transducer polarizations denoted by the red arrow in (a) and (b) . Shaded areas represent areas of no recorded data. AE event locations are superimposed on the map.

The crack density map in Figure 4.30 is similar to the SWR map shown in Figure 4.25 and frequency map in Figure 4.28. The regions with higher SWR correlate directly with zones having higher crack density which strengthens the observation that the area is associated with intense microfractures. Crack density map in Figure 4.28 (a) denote the crack density distribution for the primary fracture while Figure 4.28 (b) show the crack density inherent in the secondary microfractures, similar to the discussion in SWR and frequency map analysis.

Crack density analysis for the recorded shear waveform is done after the sample was cut 0.5-inch from the sample boundaries (Section 3.4.3) parallel to the fracture plane (See Figure 4.5). The crack density map is shown in Figure 4.31. Figure 4.31 (a) and (b) show the crack density map for two orthogonal shear wave polarizations in the plane parallel to the fracture plane. The crack density is consistently below 0.09 throughout the map for both the polarizations. The crack density map is similar to frequency map behaviour (see Figure 4.29) and does not show the contrast as seen in the V_s map (as shown in Figure 4.27) where the two polarizations have varying shear velocity responses.

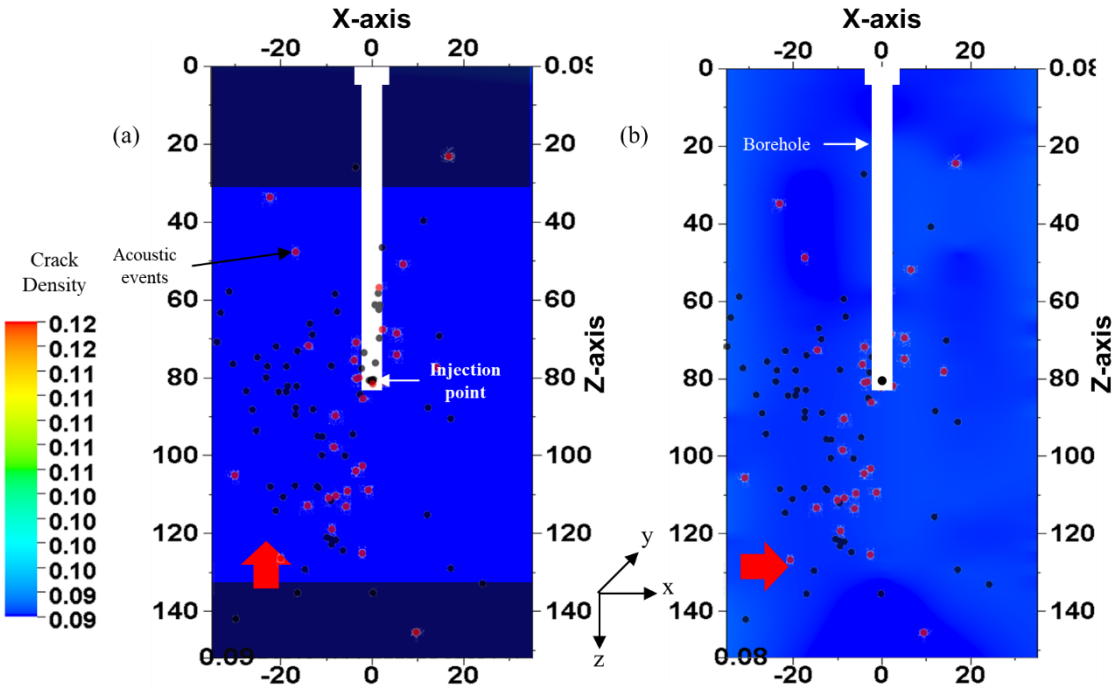

Figure 4.31 Crack density map on pyrophyllite sample PY-1 across the sides parallel to fracture plane. Shear wave propagation is along y-axis. (a) and (b): map for orthogonal transducer polarizations represented by red arrows. AE event locations are superimposed on the map. Shaded areas represent areas of no recorded data.

Unlike in Tennessee sandstone sample, TSU-6, where the crack density was in the range of 0.18 – 0.28, crack density is in far lower range of 0.09 – 0.12 in pyrophyllite sample, PY-1, with less variability in crack density as well compared to in Tennessee sandstone.

(b) PY-2

(i) Shear Wave Velocity Analysis

Figure 4.32 (a) and (b) shows the end face SWR heatmap for shear wave polarization parallel and perpendicular respectively, to the direction of the rock fabric determined from CVA (see Figure 3.4) for top surface. Direction of rock fabric is along the y-axis. Acoustic events are superimposed onto the frequency map for comparison. Fracture outline visible on the sample surface is marked by the red dashed line.

A maximum of 25 % reduction in shear wave velocity in observed. Reduction in shear wave velocity is represented by hotter colors. It is observed that the hotter colors are mostly concentrated around the borehole and unlike the SWR map in PY-1, there is not much color contrast in the SWR map in PY-2 across the fracture.

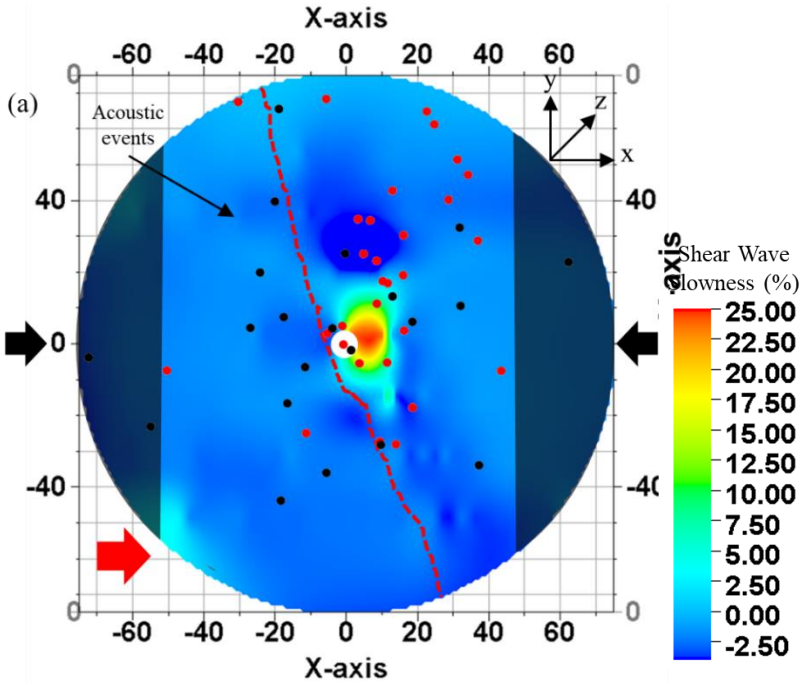

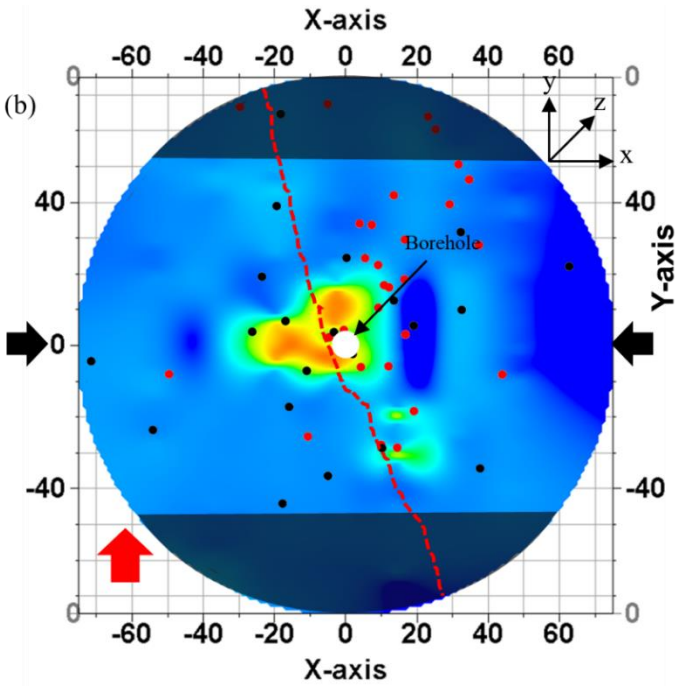

Figure 4.32 SWR map for top surface of pyrophyllite PY-2 sample. Shear wave propagation is along z-axis. Transducer polarizations denoted by the red arrow in (a) and (b). Shaded areas represent areas of no recorded data. AE event locations superimposed on the map. Red dashed lines represent the visible fracture on sample top surface

Negative SWR is due to associated measurement error (± 3%) represented by the darker shades of blue color in the heatmap.

As discussed in section 3.4.3, the sample is cut 0.5-inch from the sample boundaries parallel to the fracture plane and shear wave velocities are measured across the sides of the sample. Figure 4.33 shows the side view of the sample after it had been cut.

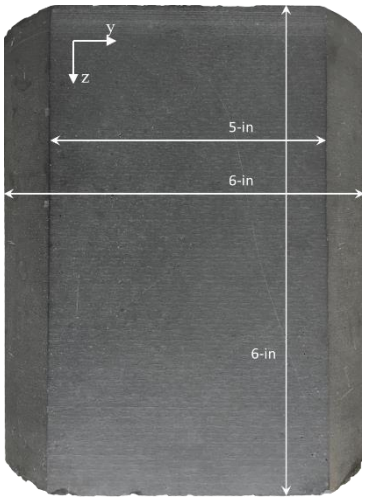

Figure 4.33 Side view of sample PY-2, cut as per Figure 3.22

Shear wave response was not recorded on the sides before fracturing for reasons mentioned earlier. V_s across the core after fracturing is analyzed for orthogonal transducer polarizations. Figure 4.34 (a) and (b) show the V_s map for two orthogonal polarizations in the plane parallel to the fracture plane. The mapped area shown corresponds to the flat surface in Figure 4.33. The transducer polarizations are marked with the red arrow in each figure. Regions where no data is recorded is shaded.

The cooler colors in the map represent faster V_s while the warmer colors represent slower V_s. In Figure 4.34 (a) as well as in Figure 4.34 (b), V_s is in the range 2.38 – 2.41 km/s, throughout the mapped sample space. This can be attributed to presence of uniform fracture distribution all throughout the YZ plane. There is a patch of slowness just below the injection point in Figure 4.34 (a) which can be due to the presence of secondary microfractures. However, unlike in PY-1 (which was fractured using water as injection fluid), the presence of secondary microfractures normal to the primary fractures in the horizontal plane is not as distinct in PY-2 (which was fractured using oil). The color contrast between the two maps is low.

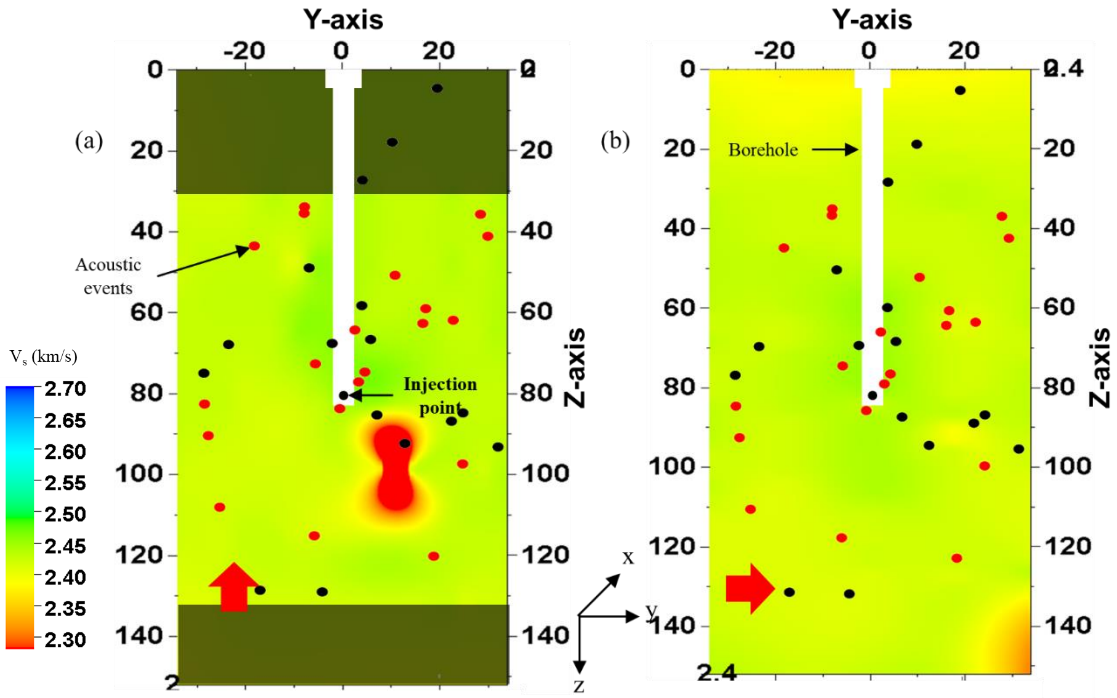

Figure 4.34 Shear velocity map on pyrophyllite sample PY-2 across the sides parallel to fracture plane. Shear wave propagation is along x-axis. (a) and (b): map for orthogonal transducer polarizations represented by red arrows. AE event locations are superimposed on the map. Shaded areas represent areas of no recorded data.

Sample is cut 0.5 inch from sample circumference, normal to the fracture plane as discussed in section 3.4.3, to analyse shear wave response. The sample is cut as shown in Figure 3.25. The opposite faces of the cut sample are shown in Figure 4.35. The fracture plane is parallel to YZ plane and perpendicular to the XZ plane shown in Figure 4.35; the visible fracture on the flat surface is outlined with black marker. The fracture is inclined to the axis of the core at an angle of 31^o in Figure 4.35 (a) and at an angle of 28^o in Figure 4.35 (b), both inclined towards positive x-axis.

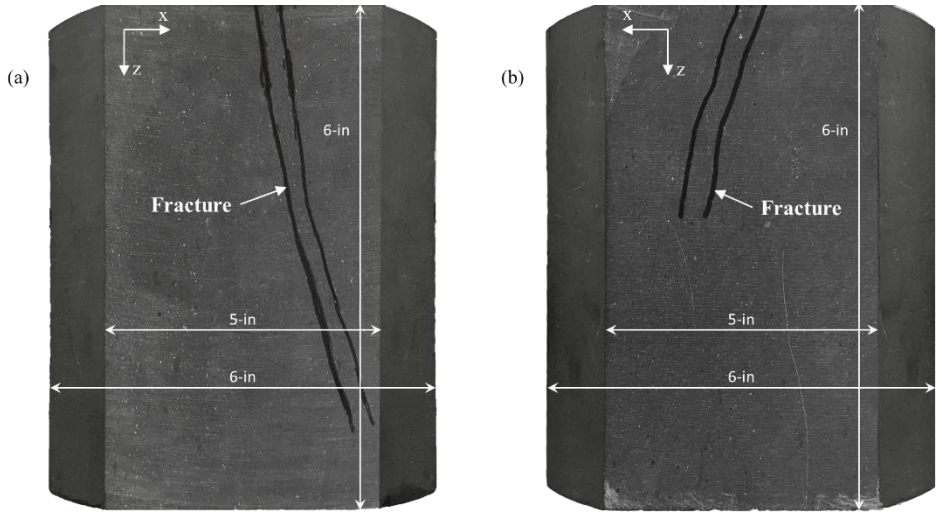

Figure 4.35 Side view of pyrophyllite sample PY-2, cut as per Figure 3.25. (a) and (b) represent the sample view on the two opposite faces after it was cut.

Figure 4.36 (a) and (b) show the V_s map for two orthogonal polarizations in the plane normal to the fracture plane (polarizations marked by red arrows). The mapped area shown corresponds to the flat surface in Figure 4.35.

In Figure 4.36 (a), shows the presence of slower V_s on the positive X axis than in the other half, thus indicating the presence of secondary microfractures that are in horizontal plane in X axis. In Figure 4.36 (b), large cluster of hotter color exists around the injection point, with V_s being as low as 2.3 km/s. This is interpreted to represent the presence of primary microfractures in the vertical plane (Z axis). The V_s is of the order of 2.38 - 2.41 km/s between (X = 10, Z = 100) and (X = 20, Z = 130). The slowness in the map can be matched with the fracture visible on the sample surface (see Figure 4.35 (a)). In Figure 4.34, the fracture extends in YZ plane, and V_s was in the range 2.38 – 2.41 km/s. Similar V_s is observed below the injection point, as discussed in Figure 4.36 (a).

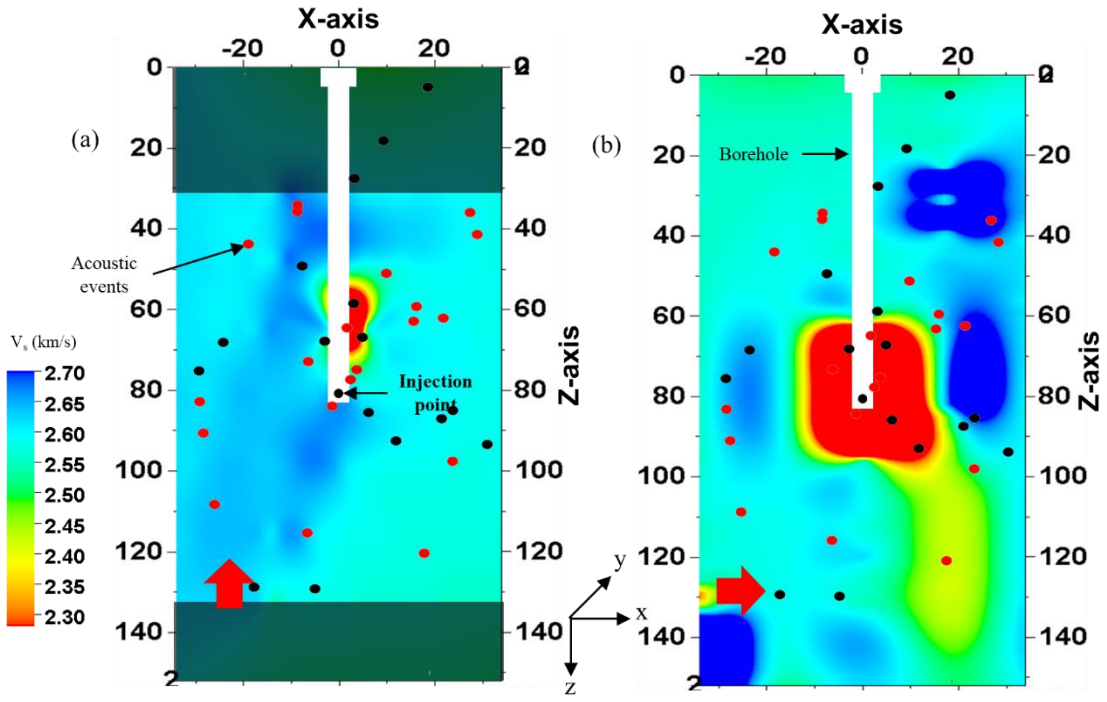

Figure 4.36 Shear velocity map on pyrophyllite sample PY-2 across the sides normal to fracture plane. Shear wave propagation is along y-axis. (a) and (b): map for orthogonal transducer polarizations represented by red arrows. AE event locations are superimposed on the map. Shaded areas represent areas of no recorded data.

Comparing the SWR maps on PY-1 and PY-2, we note that SWR is more conclusive in defining the fracture network in PY-1 which was fractured using water, compared to PY-2 which was fractured using oil. We will try to strengthen our understanding of the fracture network in PY-2 by analyzing the shear wave frequency as were done for previous samples.

(ii) Shear Wave Frequency Analysis

Spectral analysis of the shear waveforms was carried out by using FFT performed on a ± 5 µs window centered on the first arrival of the shear wave, as explained in section 4.1.4 (b).

A heatmap of the primary frequency of all the shear waveforms around the first arrival, similar to that of SWR map and shear velocity map, is plotted using convergent interpolation method in Petrel 2016.

Figure 4.37 (a) and (b) shows the frequency heatmap for the pyrophyllite sample PY-2, for shear wave polarization parallel and perpendicular respectively, to the direction of the rock fabric determined from CVA (See Figure 3.4). Fracture outline visible on the sample surface is marked by the yellow dotted line.

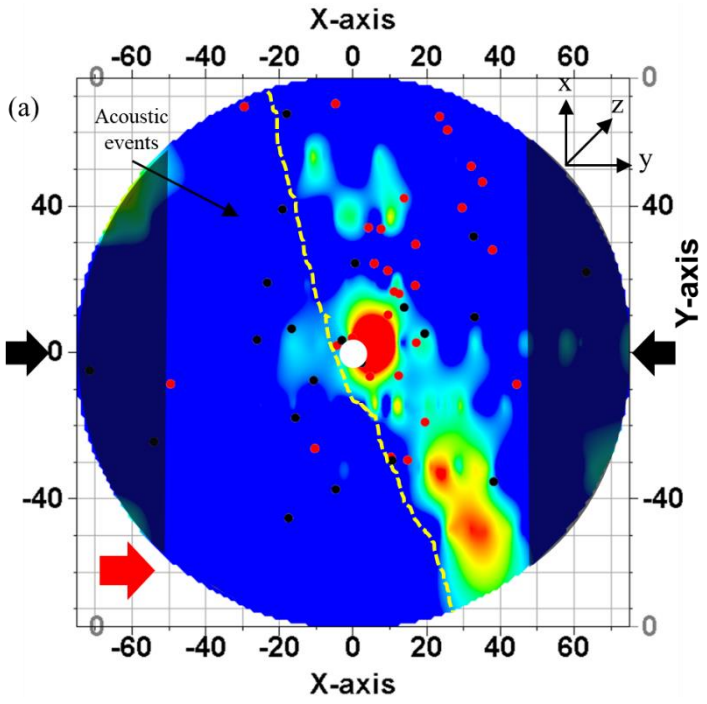

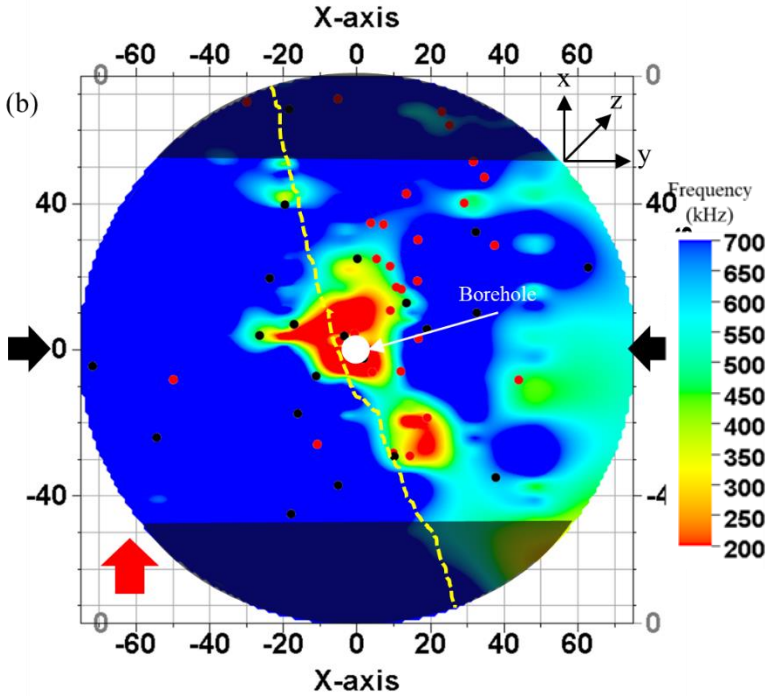

Figure 4.37 Dominant frequency map for top surface of pyrophyllite PY-2 sample. Shear wave propagation is along z-axis. Transducer polarizations denoted by the red arrow in (a) and (b). Shaded areas represent areas of no recorded data. Red (pre-breakdown) and black (post-breakdown) dots represent the superimposed AE event recorded during fracturing. Yellow dashed lines represent fracture physically visible on sample top surface.

Hotter colors in the heatmap in Figure 4.37 (a) and (b) represent lower primary frequency which can be associated with intense microfractures while cooler colors represent region with higher frequency or lower signal attenuation. The direction of the applied stress is indicated by the black arrows. Shaded regions in Figure 4.37 (a) and (b) are the regions where no shear wave data was recorded.

In contrast to the SWR map for PY-2 (see Figure 4.32), the frequency map shows distinct microfractures around the zones where fracture is visible on the sample surface. Figure 4.37 (a) shows the presence of primary fractures and Figure 4.37 (b) is representative of the secondary microfractures. Lowest frequency areas are shifted towards the positive X axis with respect to the yellow dotted lines (representing the visible fracture). Since the measured shear

wave averages over the length of the sample, the shift is due to the inclined nature of the fracture going into the sample, as can be seen in Figure 4.35.

Frequency analysis is done for the data recorded after the sample had been first cut 0.5-inch from the sample boundaries (Section 3.4.3) parallel to the fracture plane (See Figure 4.5). The frequency maps are shown in Figure 4.38 (a) and (b) for two orthogonal polarizations in the plane parallel to the fracture plane.

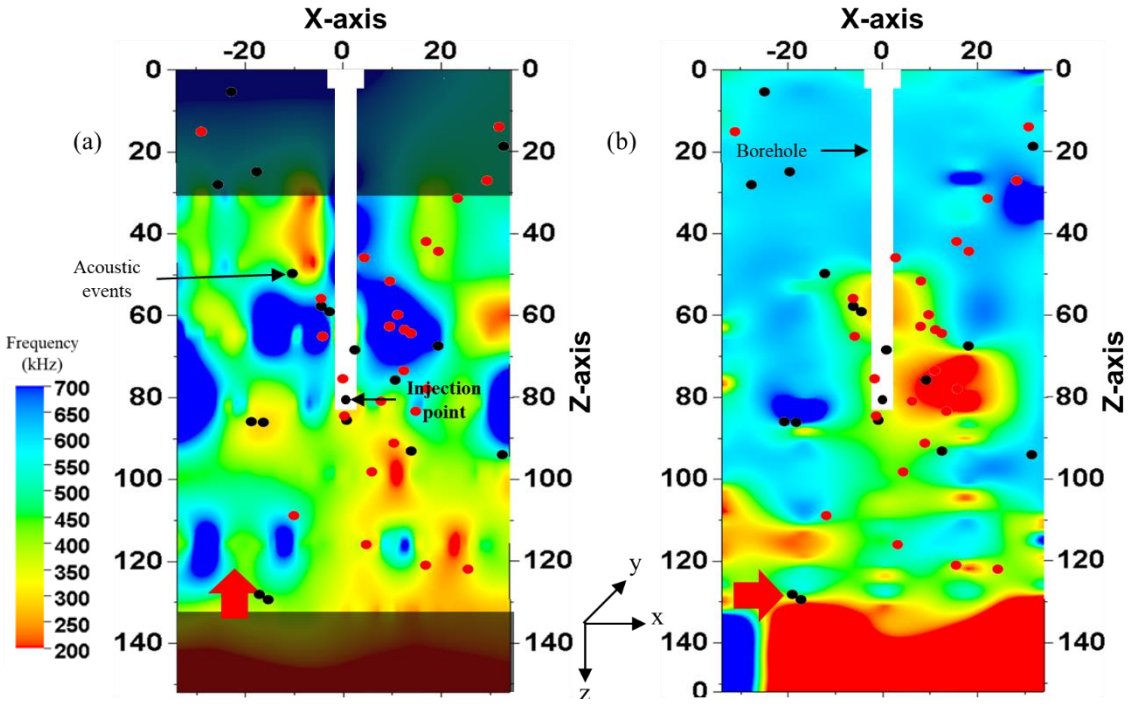

Figure 4.38 Dominant frequency map for the pyrophyllite sample PY-2 across the sides parallel to fracture plane. Shear wave propagation is along y-axis. (a) and (b): map for orthogonal transducer polarizations represented by red arrows. Red (pre-breakdown) and black (post-breakdown) dots represent the superimposed AE event recorded during fracturing. Shaded areas represent areas of no recorded data.

In Figure 4.38 (a), the signal attenuation is consistent all throughout the sample, with patches of higher frequencies. Figure 4.38 (b) shows lower frequencies (~400-550kHz) more concentrated near the wellbore and and in the range 450-650 kHz below the wellbore. Consequently, Figure 4.38 (a) shows the presence of microfractures in the horizontal plane

while Figure 4.38 (b) shows the presence of primary fracture plane. The presence and orientation of microfractures could not be confirmed with the SWR map (see Figure 4.34); however, it is quite evident with the frequency map.

Frequency analysis for the recorded shear waveform is done for the sample cut 0.5-inch from sample circumference, normal to the fracture plane as discussed in section 3.4.3. The sample is cut as shown in Figure 3.25. The cut sample is shown in Figure 4.35 and Figure 4.39 shows the frequency map.

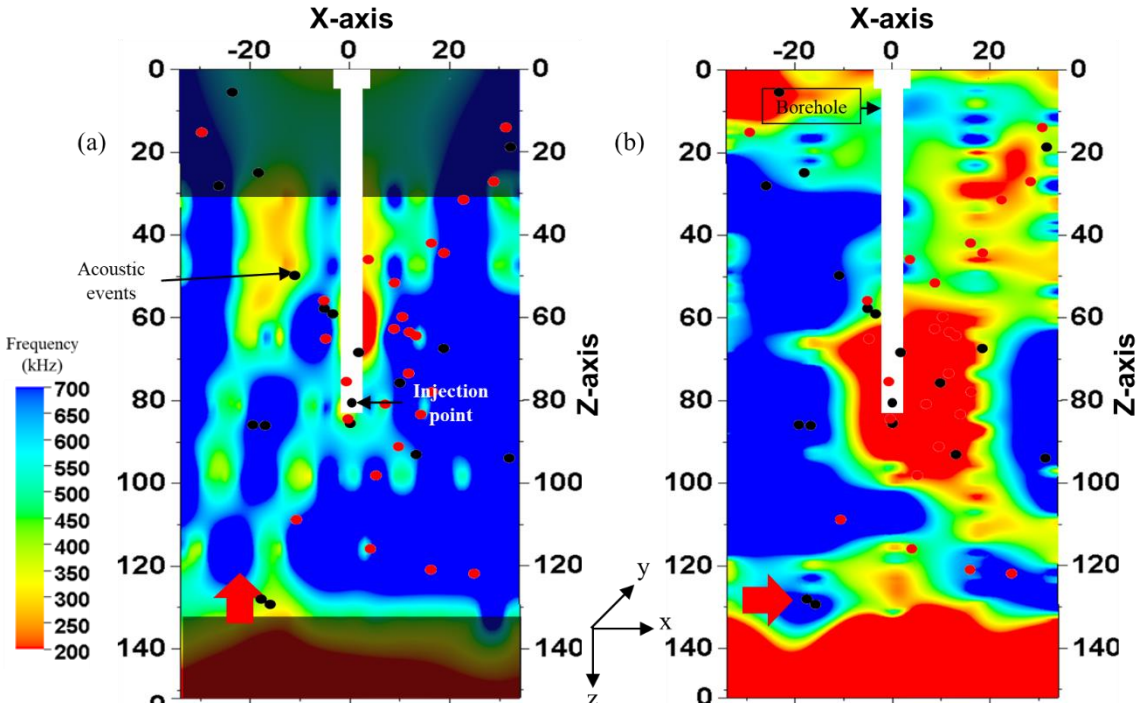

Figure 4.39 Dominant frequency map on pyrophyllite sample PY-2 across the sides normal to fracture plane. Shear wave propagation is along y-axis. (a) and (b): map for orthogonal transducer polarizations represented by red arrows. AE event locations are superimposed on the map. Shaded areas represent areas of no recorded data.

The signal attenuation is not evident in Figure 4.39 (a) which can be attributed to cracks or microfractures being oriented in the horizontal plane. Figure 4.39 (b) shows attenuation around

the wellbore correlating with the visible fracture as well as correlating with the SWR map on the side of the core as shown in Figure 4.35 (a). The attenuation is high near the injection point and gradually fades away towards the bottom of the sample along an inclined path.

(iii) Crack Density Analysis

Crack density analysis of the shear waveform is carried out using the O' Connell and Budiansky Self-Consistent model (O' Connell and Budiansky, 1974), as explained in section 4.1.4 (iii).

For pyrophyllite, the ratio of G_{dry} and G_{grain} is calculated using ρ = 2.84 g/cc; φ = 0.02 pu; G = 8 GPa. For pyrophyllite sample, PY-2, Figure 4.40 (a) and (b) shows the crack density heatmap (plan view) for shear wave polarization perpendicular and parallel respectively, to the direction of applied stress.

A heatmap of the crack density of all the shear waveforms around the first arrival, similar to that of all previous maps, is plotted using convergent interpolation method in Petrel 2016.

Figure 4.40 (a) and (b) shows the crack density heatmap for the pyrophyllite sample PY-2, for shear wave polarization parallel and perpendicular respectively, to the direction of the rock fabric determined from CVA (See Figure 3.4). Fracture outline visible on the sample surface is marked by the yellow dotted line.

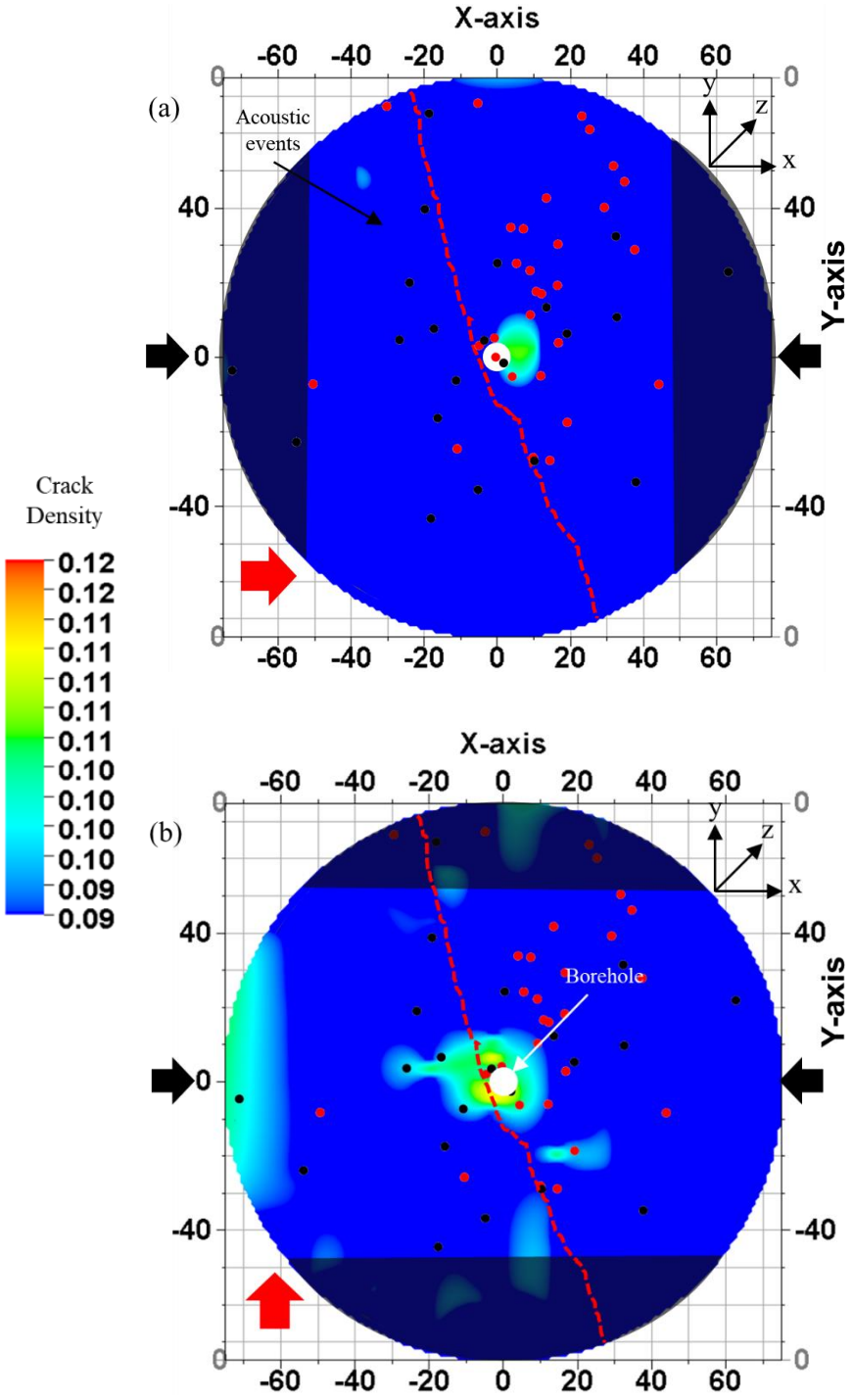

Figure 4.40 Crack density map for top surface of pyrophyllite PY-2 sample. Shear wave propagation is along z-axis. Transducer polarizations denoted by the red arrow in (a) and (b). Shaded areas represent areas of no recorded data. AE event locations are superimposed on the map.

Hotter colors in the heatmap in Figure 4.40 (a) and (b) represent higher crack density which can be associated with intense microfractures while cooler colors represent region with lower crack density. The direction of the applied stress is indicated by the black arrows. Shaded regions in Figure 4.40 (a) and (b) are the regions where no shear wave data was recorded.

Similar to the SWR map for PY-2 (see Figure 4.32) and in contrast to frequency map (see Figure 4.37), it is observed in Figure 4.40 that the higher crack density is mostly concentrated around the borehole and unlike the crack density map in PY-1, there is not much color contrast in the crack density map in PY-2 across the fracture. Figure 4.40 (a) shows the crack density of primary fractures and Figure 4.40 (b) is representative of the crack density in secondary microfractures. Highest crack density areas are shifted towards the positive X axis with respect to the yellow dotted lines (representing the visible fracture). Since the measured shear wave averages over the length of the sample, the shift is due to the inclined nature of the fracture going into the sample, as discussed earlier with respect to SWR map in Figure 4.35.

Crack density analysis is done for the data recorded after the sample had been first cut 0.5-inch from the sample boundaries (Section 3.4.3) parallel to the fracture plane (See Figure 4.5). The crack density maps are shown in Figure 4.38 (a) and (b) for two orthogonal polarizations in the plane parallel to the fracture plane.

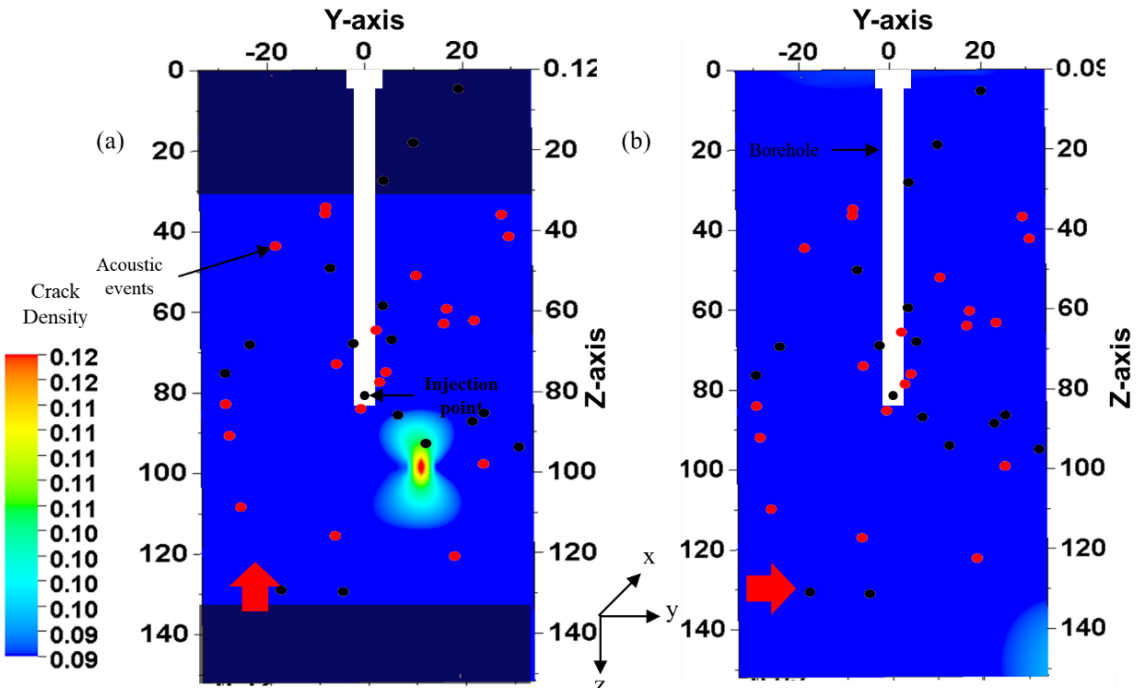

Figure 4.41 Crack density map for the pyrophyllite sample PY-2 across the sides parallel to fracture plane. Shear wave propagation is along y-axis. (a) and (b): map for orthogonal transducer polarizations represented by red arrows. Red (pre-breakdown) and black (post-breakdown) dots represent the superimposed AE event recorded during fracturing. Shaded areas represent areas of no recorded data.

The cooler colors in the map represent low crack density while the warmer colors represent high crack density. Crack density map in Figure 4.41 show a similarity in color contrast with the V_s map (see Figure 4.34). There is a patch of high crack density just below the injection point in Figure 4.41 (a) which can be due to the presence of secondary microfractures. However, unlike in PY-1 (which was fractured using water as injection fluid), the crack density of secondary fractures does not have good contrast with crack density of primary fractures in PY-2 (which was fractured using oil).

Crack density analysis for the recorded shear waveform is done for the sample cut 0.5-inch from sample circumference, normal to the fracture plane as discussed in section 3.4.3. The

sample is cut as shown in Figure 3.25. The cut sample is shown in Figure 4.35 and Figure 4.42 shows the crack density map.

In Figure 4.42, crack density map is consistent with the V_s map shown in Figure 4.36. The low V_s zone in Figure 4.36 (b) correlates with a high crack density of 0.12 around a large cluster around the injection point in Figure 4.42 (b) representing the crack density of the primary fracture zone. Unlike the V_s map in Figure 4.36 (b), the tail of the fracture beneath the injection point is not represented with a contrasting crack density as can be observed on the V_s map.

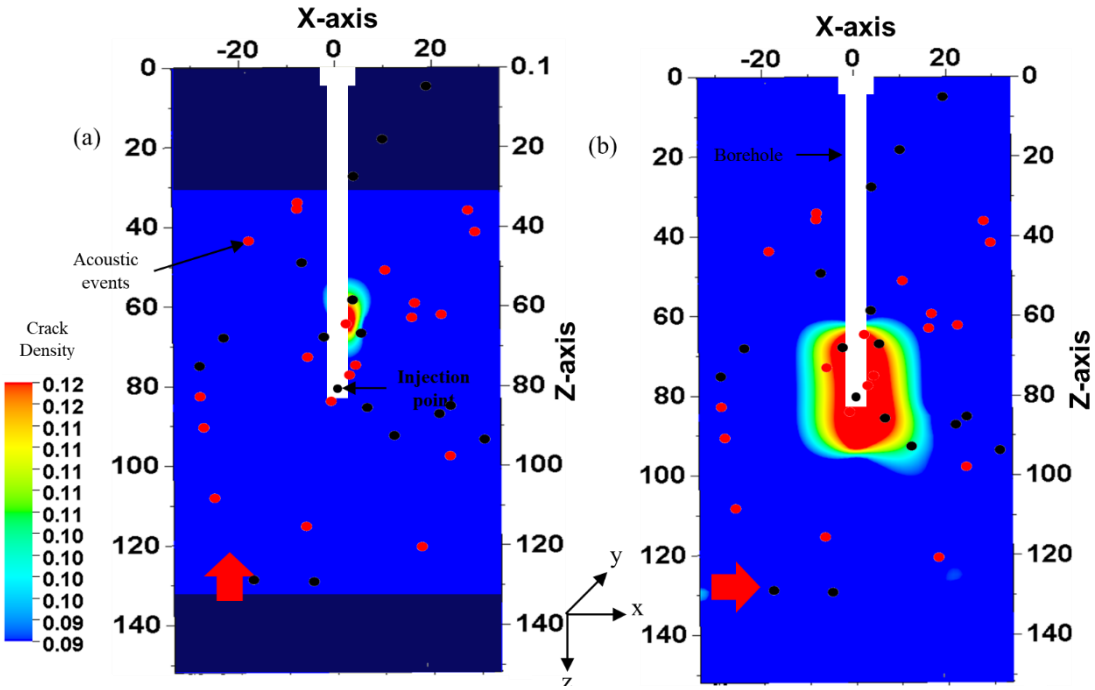

Figure 4.42 Crack density map on pyrophyllite sample PY-2 across the sides normal to fracture plane. Shear wave propagation is along y-axis. (a) and (b): map for orthogonal transducer polarizations represented by red arrows. AE event locations are superimposed on the map. Shaded areas represent areas of no recorded data.

Crack density range of values for PY-2 (0.09 – 0.12) is in the similar range as in PY-1 and is lower than crack density values observed in Tennessee sandstone (0.18 – 0.28).

5 CONCLUSION

1. In isotropic medium (Tennessee sandstone), induced fractures oriented with the direction of maximum horizontal stress overcoming the local rock heterogeneities.

2. In anisotropic sample (pyrophyllite), fracture is always induced in the direction of the rock fabric at the applied stress levels used in these tests. In PY-1, fracture is physically observed to be at 9^o to the rock fabric direction, and in PY-2, it is observed to be at 20^o to the rock fabric.

3. Physical observation of fractures shows non-linear and non-planar in both Tennessee sandstone and pyrophyllite.

4. The acoustic activity recorded in Tennessee sandstone (TSU-6) occurred in two rapid bursts, first during the fracture initiation and propagation stage and a second burst in AE activity was observed during fracture closure after fluid injection was stopped. The secondary activity may be due to the shearing of asperities along the closing fracture faces. Similar acoustic activity is noticed in pyrophyllite (PY-1) with bursts of acoustic activities during fracture initiation and propagation followed by a second burst of acoustic activity (total 513 AE events). In sample PY-2, after the breakdown, multiple rapid bursts of secondary acoustic activity were observed but, very few acoustic events were recorded (total 219 AE events).

5. Breakdown pressure is lower in pyrophyllite as compared to Tennessee sandstone when fractured with water. However, when a more viscous fluid such as oil is used for fracturing, pyrophyllite exhibit more than 2000 psi higher breakdown pressure.

6. AE event map for Tennessee sandstone as well as for the pyrophyllite (PY-1) test correlated well with the physical observation of induced fractures.

7. SWR reflects intensity of cracks or fractures induced by the hydraulic fracturing process. It can be used as a qualitative representation of the complexity and intensity of induced fracturing. Maximum SWR observed (for both shear wave polarizations) in Tennessee sandstone is 24% post fracture, while it is as high as 30% in pyrophyllite (PY-1) fractured using water and is around 25% in pyrophyllite (PY-2) fractured using oil. Mapping the reduction in velocity can be used to interpret the stimulated zone post-fracturing i.e. SRV.

8. Shear wave frequency map is consistent with the physically observed fracture for Tennessee sandstone as well as both the pyrophyllite samples. Though SWR map is inconclusive for PY-2 to map fractures, SWR map can be analyzed alongside the frequency map to trace the fractures in it. Despite low recorded microseismic activity during the fracturing of PY-2, polarized shear wave could potentially map the fracture network in pyrophyllite whereas fracture mapping was not possible through microseism.

9. Crack density map is consistent with the SWR and V_s map for all the three samples.

10. Crack density is more than twice in Tennessee sandstone (0.18 – 0.28) compared to pyrophyllite (0.09 – 0.12).

11. Polarized shear wave can be used to potentially identify orientation of primary as well as secondary fractures induced by hydraulic fracturing in laboratory and can be directly used to identify the SRV. Microfracture network study in lab experiments using SEM imaging also show similar observations (Ratzlaff, 2018).

12. The microscopic properties of fracture analyzed by SEM would be reflected in the shear waveforms; the shear wave is affected by the presence of cracks and fractures. Shear birefringence can be useful in bridging the microscopic level of SEM imaging to the microseismics in hydraulic fracture analysis. This would allow better understanding of the SRV.

13. SWR mapping of hydraulic fracture is a repeatable process whereas AE event recording can occur only during the fracturing process and is non-repeatable.

6 FUTURE RECOMMENDATIONS

1. Polarized shear wave is a potential diagnostic tool for fractures induced during hydraulic fracturing under laboratory conditions and can potentially better define the stimulated reservoir volume.

2. Presence of natural fractures can make the injection of fluid or gas breakthrough to nearby producing wells. Mapping fault and natural fractures using shear wave splitting can help in planning the injection process and in accessing confinement for EOR projects

3. Shear-wave VSP can be conducted on field to detect hydraulic fractures induced in a nearby well (Turpening et al., 1981). An impulsive S-wave source can be located at the surface and receiver geophones can be installed in a receiver well. Various VSP operations are listed by Gal'perin (1977), Robertson and Corrigan (1983), Meadows and Winterstein (1994), Winterstein et al. (1995) and Winterstein et al. (2001). Shear wave predominantly travel through the un-stimulated path; downhole arrays placed at the heel of the reservoir will be suitable for characterizing reservoir heterogeneity while if the downhole arrays are placed at the toe of the treatment, the response of the reservoir to the hydraulic stimulation can be made.

7 REFERENCES

1. Agarwal, R., 2012. Measurement of Shale Permeability Using a Pressure Build-up Technique, Master's Thesis, University of Oklahoma:1-91

2. Albright, J. N., and Pearson, C. F., 1982. Acoustic Emissions as a Tool for Hydraulic Fracture Location: Experience at the Fenton Hill Hot Dry Rock Site. Soc. of Petr. Eng. doi:10.2118/9509-PA

3. Aldridge, D. and Bartel, L., 2016. Systems and Methods for Locating and Imaging Proppant in an Induced Fracture, US Patent No 9,250,351

4. Alford, R. M., 1986. Shear data in the Presence of Azimuthal Anisotropy: Dilley, Texas: 56th Ann. Internal. Mtg., Soc. Expl. Geophys., Expanded Abstracts, 476-479.

5. Alford, R. M., 1986a. Multisource Multireceiver Method and System for Geophysical Exploration, European Patent Application Publication, 0 169 075.

6. API (American Petroleum Institute), 2013. Investment in U.S. Shale Well Drilling Surges in 2011, http://www.api.org/news-and-media/news/newsitems/2013/april-2013/investment-in-us-shale-well-drilling-surges-in-2011 (2013) (accessed August 1, 2017)

7. Berryman, J. G., 2008. Exact Seismic Velocities for Transversely Isotropic Media and Extended Thomsen Formulas for Stronger Anisotropies, Geophys., V. 73 (1): D1-D10.

8. Bhoumick, P., Dang, S. T., Damani, A., Sondergeld, C., and Rai, C. S., 2017. Stimulated Reservoir Volume Evaluation Using Shear Wave. Amer. Rock Mech. Assoc. ARMA-17-0409. Pages 1-10.

9. Bhoumick, P., Sondergeld, C., and Rai, C. S., 2018. Mapping Hydraulic Fracture in Pyrophyllite Using Shear Wave. Amer. Rock Mech. Assoc, ARMA-18-151. Pages 1-7.

10. Bohloli, B. and de Pater, C. J., 2006. Experimental Study on Hydraulic Fracturing of Soft Rocks: Influence of Fluid Rheology and Confining Stress, J. of Petr. Sci. and Eng., V. 53(1): 1-12.

11. Bonner, B., 1974. Shear Wave Birefringence in Dilating Granite: Geophys. Res. Lett., 1, 217-220.

12. Cannan, C., Bartel, L., Palisch, T. and Aldridge, D., 2015. Electrically Conductive Proppant and Methods for Detecting, Locating and Characterizing the Electrically Conductive Proppant, US Patent No 8,931,553

13. Carter, R., 1957. Derivation of General Equation for Estimating the Extent of the Fracture Area, 261-168 pp., Drill. And Prod. Prac, API.

14. Cheung, L.S. and Haimson, B., 1989. Hydrofracturing Stress Measurements in Fractured Rock: A Laboratory Study, Presented at the 30th U.S. Symp. on Rock Mech., June 19-22, 1989, Morgantown, WV.

15. Chitrala, Y., 2011. Laboratory Study of Fluid Induced Hydraulic Fractures - Hypocenter Locations, Source Mechanism, Frequency Analysis and Microscopic Observations, Master's Thesis, University of Oklahoma, Norman: 1-239.

16. Cipolla, C.L. and Wright, C.A., 2000. Diagnostic Techniques to Understand Hydraulic Fracturing: What? Why? and How?, SPE 59735, Soc. Of Petr. Eng. Gas Technology Symposium, Calgary, Alberta, Canada.

17. Coffer, H.F., Bray, B.G., Knutson, C.F. and Rawson, D.E., 1964. "Effects of Nuclear Explosions on Oil and Gas Reservoir Stimulation," J. of Petr. Tech., 473-480.

18. Cox, V. D., Rizer, W. D., Anno, P. D., and Queen, I. H., 1989. An Integrated Study of Seismic Anisotropy and the Fracture System in the Spraberry Sandstone, Pembrook Field, Upton and Reagan Counties, Texas. Presented at the SEG summer workshop on Recording and Processing Vector Wavefield Data, Snowbird, Utah

19. Craddock, P. R., Herron, M. M., and Herron, S. L., 2016. Quantitative Mineral Analysis of Sedimentary Formations Using FTIR Spectroscopy. Soc. of Petrophys. and Well-Log Analysts.

20. Crampin S., 1977. Seismic Wave Propagation in Anisotropic Media: I: Computations, Geophys. J. R. Astr. Soc., 49, 303.

21. Crampin, S., 1978. Seismic Wave Propagation through a Cracked Solid: Polarization as a Possible Dilatancy Diagnostic, Geophys. J. R. Astr. Sot., 53, 467-496.

22. Crampin, S., 1981. A Review of Wave Motion in Anisotropic and Cracked Elastic-Media, Wave Motion, 3, 343-391.

23. Crampin, S., 1984. Effective Anisotropic Elastic Constants for Wave Propagation through Cracked Solids, Geophys. J. of the Royal Astr. Soc., 76, 135–145, doi: 10.1111/j.1365-246X.1984.tb05029.x.

24. Crampin, S., and Love, J. H., 1991. A Decade of Shear-Wave Splitting in the Earth's Crust: What does it Mean? What use can we make of it? and what should we do next? Geophys. J. Intern., 107, 387–407.

25. Crampin, S., Bush, I., Naville, C., and Taylor, D., 1986. Estimating Stress-Aligned Pore Space in Sedimentary Basins with Shear-Wave VSPs: A Case Study: Soc. Petr. Eng. Ann. Tech. Conf.

26. Crampin, S., Lynn, H. B., and Booth, D. C., 1989. Shear-Wave VSP: A Powerful New Tool for Fracture and Reservoir Description. Soc. of Petr. Eng. doi:10.2118/16866-PA

27. Crampin, S., McGonigle, R., and Bamford, C., 1980. Estimating Crack Parameters from Observations of P-Wave Velocity Anisotropy: Geophys., 45, 345-360

28. Damani, A., 2013. Acoustic Mapping and Fractography of Laboratory Induced Hydraulic Fractures, Master's Thesis, University of Oklahoma, Norman: 1-223.

29. Damani, A., Sharma, A., Sondergeld, C. and Rai, C., 2012. Acoustic Emission and SEM Analyzes of Hydraulic Fractures Under Triaxial Stress Conditions. Soc. of Expl. Geophys, Pages 1-5. https://doi.org/10.1190/segam2012-1585.1.

30. Daneshy, A. A., 1973. A Study of Inclined Hydraulic Fractures, Soc. Of Petr. Eng. J, V. 13(2): 61-68.

31. Dang, S., Gupta, I., Chakravarty, A., Bhoumick, P., Taneja, S., Sondergeld, C., and Rai, C., 2017. Recovering Elastic Properties from Rock Fragments. Soc. of Petrophys. and Well-Log Analysts.

32. de Figueiredo, J. J. S., Schleicher, J., Stewart, R. R., Dayur, N., Omoboya, B., Wiley, R. and William, A., 2013. Shear Wave Anisotropy from Aligned Inclusions: Ultrasonic Frequency Dependence of Velocity and Attenuation, Geophys. J. Intern., Volume 193, Issue 1, Pages 475–488, https://doi.org/10.1093/gji/ggs130

33. Detournay, E., McLennan, J. D. and Roegiers, J. C., 1986. Poroelastic Concepts Explain Some of the Hydraulic Fracturing Mechanisms, SPE 15262.

34. Economides, M. J., 2011. Hydraulic Fracturing: The State of the Art, Energy Tribune Article.

35. Economides, M. J., Martin, T. (eds), 2007. Modern Fracturing - Enhancing Natural Gas Production. ET Publishing, Houston, Texas

36. Fisher, M. K., Wright, C. A., Davidson, B. M., Goodwin, A. K., Fielder, E., O., Buckler, W. S., and Steinsberger, N. P., 2002. Integrating Fracture Mapping Technologies to Optimize Stimulations, SPE 77441, Soc. Of Petr. Eng. ATCE, San Antonio, Texas.

37. Gal'perin, E. I., 1977. The Polarization Method of Seismic Exploration: (in Russian): Nedra, Moscow; English translation, 1984, D. Reidel Publishing Co.

38. Garotta, R., and Granger, P., 1988. Acquisition and Processing of 3cX3c-D Data Using Converted Waves. 58th Ann. Internat. Mtg., Soc. Expl. Geophys., Expanded Abstracts, 995-997.

39. Grebe, J. J. and Stosser S. M., 1935. “Increasing Crude Production 20,000,000 Barrels from Established Fields”, World Petr. 6, 8, 473.

40. Grebe, J. J., 1943. “Tools and Aims of Research”, Chem. and Eng. News.

41. Greestma, J. and De Klerk, F. 1969. A Rapid Method of Predicting Width and Extent of Hydraulic Induced Fractures, J. of Petr. Tech., V.21 (12): 1571-1581.

42. Groat, C. G. and Grimshaw, T. W., 2012. Fact-Based Regulation for Environmental Protection in Shale Gas Development, Energy Institute Report, University of Texas, Austin,TX.

43. Gross, C., 2002. Hsu Nielsen Source, http://www.ndt.net/ndtaz/ndtaz.php

44. Guo, F., Morgenstern, N. R. and Scott, J. D., 1993a. An Experimental Investigation into Hydraulic Fracture Propagation - Part I. Experiment Facilities, Intern. J. Rock Mech. Min, Sci and Geomech. Abstr, V. 30(3):177-188.

45. Guo, F., Morgenstern, N. R. and Scott, J. D., 1993b. An Experimental Investigation into Hydraulic Fracture Propagation - Part 2. Single Well Tests, Intern. J. Rock Mech. Min, Sci and Geomech. Abstr, Vol. 30(3): 189-202.

46. Gupta, I. N., 1973. Seismic Velocities in Rock Subjected to Axial Loading up to Shear Fracture: J. Geophys. Res., 78,69366942.

47. Haimson, B. and Fairhurst, C., 1969. Hydraulic Fracturing in Porous Permeable Materials, J. of Petr. Tech., V. 21(7): 811‑817.

48. Hartog, R. and Schwartz, S. Y., 2000. Subduction-Induced Strain in the Upper Mantle East of the Mendocino Triple Junction, California, J. Geophys. Res., 105(B4), 7909–7930, doi:10.1029/1999JB900422.

49. Hassebroek, W. E. and Waters, A. B., 1964. Advancements through 15 Years of Fracturing, SPE 801, J. of Petr. Tech. 16(7): 760-764.

50. Holley, E. H., Zimmer, U., Mayerhofer, M. J. and Samson, E., 2010. Integrated Analysis Combining Microseismic Mapping and Fiber-Optic Distributed Temperature Sensing (DTS). Soc. of Petr. Eng. doi:10.2118/136565-MS

51. Howard, G. C. and Fast, C. R., 1970. Hydraulic Fracturing, Monograph Series Vol. 2, Soc. Of Petr. Eng., Dallas, Texas, USA

52. Hsu, N. N. and Breckenridge, F. R., 1981. Characterization and calibration of acoustic emission sensors, Mat. Evaluation, 39, 60.

53. Hubbert, M. K. and Willis, D. G., 1957. Mechanics of Hydraulic Fracturing, Tran. AIME, V. 210: 153‑168.

54. Hudson, J. A., 1981. Wave Speeds and Attenuation of Elastic Waves in Material containing Cracks, Geophys. J. Roy. Astr. Soc., 64, 133-150.

55. Jackson, R. B., Vengosh, A., Darrah, T. H., Warner, N. R., Down, A., Poreda, R. J., Osborn, S. G., Zhao, K. and Karr, J. D., 2013. Increased Stray Gas Abundance in a Subset of Drinking Water Wells Near Marcellus Shale Gas Extraction, Proc. Natl. Acad. Sci., 110 (28), pp. 11250–11255

56. Kale, S., 2009. Petrophysical Characterization of Barnett Shale Play, Master's Thesis, University of Oklahoma: 1-114.

57. Karpyn, Z., Alajmi, A., Parada, C., Grader, A., Halleck, P., and Karacan, O., 2003. Mapping Fracture Apertures Using Micro-Computed Tomography, The Soc. of Core Analysis 2003 Intern. Symp., Pau-France. SCA2003-50, p. 575-580.

58. Keith, C. M. and Crampin, S., 1977. Seismic Body Waves in Anisotropic Media, Geophys. J. R. Astr. Sot., 49, 181-243.

59. Kirsch, G. D., 1898. theorie der elastizitat und die bedurfnisse der festigkeitslehre. Veit Ver Deut Ing, 42: 797-807

60. Lefeuvre, F., Turpening, R., Caravana, C., Born, A. and Nicoletis, L., 1993. Vertical Open Fractures and Shear-Wave Velocities Derived from VSPs, Full Waveform Acoustic Logs, and Televiewer Data. Geophys. 58. 818-834. 10.1190/1.1443467.

61. Levin, V., Menke, W. and Park, J., 1999. Shear Wave Splitting in the Appalachians and the Urals: A Case for Multilayered Anisotropy,J. Geophys. Res.,104(B8),17975–17993, doi:10.1029/1999JB900168.

62. Loomis, J. and Haefele, M., 2017. Quantifying Market and Non-market Benefits and Costs of Hydraulic Fracturing in the United States: A Summary of the Literature. Ecological Economics 138:160–167. doi: 10.1016/j.ecolecon.2017.03.036

63. Martin, M. A., and Davis, T. L., 1987. Shear-Wave Birefringence: A New Tool for Evaluating Fractured Reservoirs: The Leading Edge, 6, 22–28

64. Masuda, K., Nishizawa, O., Kusunose, K. and Sato, T., 1990. Laboratory Study of Fluid Pressure Diffusion in Rock Using Acoustic Emissions: J. of Geophys. Res., 95, no. B13, 21593–21607.

65. Matsunaga, I., H., Kobayashi, S., Sasaki and Ishida, T., 1993. Studying Hydraulic Fracturing Mechanism by Laboratory Experiments with Acoustic Emission Monitoring. Intern. J. Rock Mech. Min. Sci. and Geomech. Abstr. 30(7): 909-912.

66. Maxwell, S. C., C. K. Waltman, N. R. Warpinski, M. J. Mayerhofer, and Boroumand, N., 2006, Imaging Seismic Deformation Associated with Hydraulic Fracture Complexity: SPE 102801.

67. Mayerhofer, M. J., Lolon, E. P., Warpinski, N. R., Cipolla, C. L. and Walser, D. and Rightmire, C. M., 2010. What is Stimulated Rock Volume? SPE 119890.

68. Meadows, M. A. and Winterstein, D. F., 1994. Seismic Detection of a Hydraulic Fracture from Shear-Wave VSP Data at Lost Hills Field, California. Geophys., 59(1), 11-26. https://doi.org/10.1190/1.1443523.

69. Mokhtari, M., Hayatdavoudi, A., Nizamutdinov, R., Rizvi, H., and Nath, F., 2017. Characterization of Complex Fracture Propagation in Naturally Fractured Formations Using Digital Image Correlation Technique. Soc. of Petr. Eng. doi:10.2118/184826-MS

70. Moreno, C., 2011. Microseismic Mapping of Fluid Induced Hydraulic Fractures and Analysis of Location Uncertainties, Master's Thesis, University of Oklahoma, Norman: 1-213.

71. Morita, N., Fuh, G. F. and Black, A. D., 1996. Borehole Breakdown Pressure with Drilling Fluids ‑I Empirical Results, Intern. J. rock Mech. Min. Sci and Geomech. Abstr, V.33 (1): 39-51.

72. Mueller, C. M., 1991. Prediction of Lateral Variability in Fracture Intensity Using Multicomponent Shear-Wave Surface Seismic as a Precursor to Horizontal Drilling in the Austin Chalk,Geophys. J. Intern., Volume 107, Issue 3, Pages 409–415, https://doi.org/10.1111/j.1365-246X.1991.tb01402.x

73. NDT Resource Center, 2017. Wave Propagation, https://www.nde-ed.org/EducationResources/CommunityCollege/Ultrasonics/Physics/wavepropagation.htm (accessed April 24, 2018)

74. Nolte, K., and Smith, M., 1981. Interpretation of Fracturing Pressures, J. of Petr. Tech., 33 (9), 1767–1775.

75. Nur, A., and Simmons, G., 1969. Stress Induced Velocity Anisotropy in Rock: An Experimental Study: J. Geophys. Res., 74,6667-6674.

76. O' Connell R. J., and Budiansky, B., 1974. Seismic Velocities in Dry and Saturated Cracked Solids, J. Geophys. Res., 79, 5412-5426.

77. O' Connell R. J., and Budiansky, B., 1974. Seismic Velocities in Dry and Saturated Cracked Solids, J. Geophys. Res., 79, 5412-5426.

78. Ortiz, A. A., 2010. Automatic Picking and Classification of Acoustic Emission Event Arrivals, Master's Thesis, University of Oklahoma, Norman: 1-156.

79. Palisch, T., Al-Tailji, W., Bartel, L., Cannan, C., Zhang, J., Czapski, M. and Lynch. K., 2017. Far-Field Proppant Detection Using Electromagnetic Methods - Latest Field Results. Soc. of Petr. Eng. doi:10.2118/184880-MS

80. Perkin, T.K. and Kern, L.R. 1961.Widths of Hydraulic Fractures, J. of Petr. Tech., V. 13(9): 937‐949.

81. Prince, M., and Tovar. C., 2015. How Much U.S. Oil and Gas Comes from Fracking?, Wall Street J., April 1, 2015

82. Rai, C. S. and Hanson, K. E., 1988. Shear-Wave Velocity Anisotropy in Sedimentary rocks: A Laboratory Study: Geophys., 53, 800–806, doi: 10 .1190/1.1442515.

83. Rassenfoss, S., 2016. Electromagnetic Imaging Offers First Look at the Propped Rock. Soc. of Petr. Eng. doi:10.2118/0316-0032-JPT

84. Rathore, J. S., Fjaer, E., Holt, R. M. and Renlie, L., 1991. Acoustic Anisotropy of Synthetics with Controlled Crack Geometries, Proc. Eur. Assoc. Expl. Geophys. Mtg., 538-539.

85. Ratzlaff, C. W., 2018. SEM Investigation of the Fracture Network (Stimulated Reservoir Volume) Induced by Hydraulic Fracturing, Master's Thesis, University of Oklahoma, Norman: 1-171.

86. Robertson, 1. D. and Corrigan, D., 1983. Radiation Studies on a Shear-Wave Vibrator in Near-Surface Shale: Geophys., 48,19-26.

87. Rutledge, J. T. and Phillips, W. S., 2003. Hydraulic Simulation of Natural Fractures as Revealed by Induced Microearthquakes, Carthage Cotton Valley gas field, East Texas. Geophys. 68 (2): 441. doi: 10.1190/1.1567212.

88. Savage, M. K., 1999. Seismic Anisotropy and Mantle Deformation: What Have we Learned from Shear Wave Splitting?,Rev. Geophys.,37(1),65–106, doi:10.1029/98RG02075.

89. Schoenberg, M., 1983. Reflection of Elastic Waves from Periodically Stratified Media with Interfacial Slip: Geophys. Prosp., 2, 265.

90. Simmons, G. and Wang, H., 1971. Single Crystal Elastic Constants and Calculated Aggregate Properties: Handbook, the MIT Press, p. 370.

91. Sondergeld, C. H. and Estey, L. H., 1982. Source Mechanisms and Micro-Fracturing During Uniaxial Cycling of Rock, Pure Appl. Geophys., V. 120 (1): 151-166.

92. Sondergeld, C. H. and Rai, C. S., 1992. Laboratory Observations of Shear Wave Propagation in Anisotropic Media: The Leading Edge, 11, 38–43, doi: 10.1190/1.1436871.

93. Sondergeld, C. H. and Rai, C. S., 2011a. Elastic Anisotropy of Shales, The Leading Edge, V. 30 (3): 324-331.

94. Sondergeld, C. H. and Rai, C. S., 2015. Seismic Reservoir Modelling, Classroom Lectures, University of Oklahoma.

95. Stein, S. and Wysession, M., 2003. An Introduction to Seismology, Earthquakes, and Earth Structure, Blackwell Publishing Ltd., Malden, MA, USA.

96. Stewart, R. R., Turpening, R. M. and Toksoz, M. N., 1981. Study of a Subsurface Fracture Zone by Vertical Seismic Profiling. Geophys. Res. Lett., 8: 1132-1135. doi:10.1029/GL008i011p01132

97. Tatham, R. H., Matthews, M. D., Sekharan, K. K., Wade, C. J. and Liro, L. M. 1987. A Physical Model Study of Shear Wave Splitting and Fracture Intensity. Soc. of Expl. Geophys.

98. Teanby, N., Kendall, J.-M., and van der Baan, M., 2004a, Automation of Shear-Wave Splitting Measurements Using Cluster Analysis, Bulletin of the Seis. Soc. of Amer., 94 (2), 453–463, doi:10.1785/0120030123.

99. Thiercelin, M. C. and Roegiers, J. C., 2001. Formation Characterization: Rock Mechanics, Reservoir Stimulation, 3rd Ed., Edited by Economides and Nolte, Schlumberger Educational Services, Houston, Texas, USA. 3.1 – 3.34.

100. Thomsen, L. A., 1988. Reflection Seismology over Azimuthal Anisotropic Media: Geophys., 53, 304-313.

101. Thomsen, L., 1986. Weak Elastic Anisotropy, Geophys., V. 51 (10): 1954-1966.

102. Tilmann, S. E. and Bennett, H. F., 1973. Ultrasonic Shear Wave Birefringence as a Test of Homogeneous Elastic Anisotropy: J. Geophys. Res., 78,7623-7629.

103. Timoshenko, S. P. and Goodier, J. N., 1970. Theory of Elasticity, 3rd Edition, McGraw Hill, New York.

104. Todd. T., Simmons. G. and Baldridge. W. S., 1973. Acoustic Double Refraction in Low-Porosity Rocks: Bull. Seis. Soc. Am., 63, 2007-2020.

105. Tsvankin, I., 1997. Anisotropic Parameters and P-Wave Velocity for Orthorhombic Media, Geophys., 62 (4), 1292, doi:10.1190/1.1444231.

106. Tsvankin, I., and Grechka, V., 2011. Seismology of Azimuthally Anisotropic Media and Seismic Fracture Characterization, 421–462 pp., Soc. of Expl. Geophys., doi:10.1190/1.9781560802839.ch9.

107. U.S. Energy Information Administration, 2015. Shale in the United States, http://www.eia.gov/energy_in_brief/article/shale_in_the_united_states.cfm (accessed August 1, 2017)

108. U.S. Energy Information Administration, 2016a. Hydraulically Fractured Wells Provide Two-Thirds of U.S. National Gas Production, Today in Energy (2016) (May 5, 2016)

109. U.S. Energy Information Administration, 2018. EIA's Annual Energy Outlook, https://www.eia.gov/outlooks/aeo/pdf/AEO2018.pdf

110. US Energy Information Administration, 2016.Trends in U.S. Oil and Natural Gas Upstream Costs (March 2016)

111. US Energy Information Administration, 2017. Where Our Natural Gas Comes From – Basics, https://www.eia.gov/energyexplained/print.php?page=natural_gas_where (Accessed October 7, 2018)

112. US. Energy Information Administration, 2016. Hydraulic Fracturing Accounts for About Half of Current U.S. Crude Oil Production, Today in Energy (2016) (March 15, 2016)

113. Veatch Jr., R. W., 1983. Overview of Current Hydraulic Fracturing Design and Treatment Technology-Part 1, J. of Petr. Tech., V. 35 (4): 677-687.

114. Verma, R. K., 1960. Elasticity of Some High-Density Crystals: J. Geophys. Res., 65, 757-766.

115. Wang, Z., 2002. Seismic Anisotropy in Sedimentary Rocks, Part 2: Laboratory data, Geophys., V. 67 (5): 1423-1440.

116. Warpinski, N. R. ,1996. Hydraulic Fracture Diagnostics. Soc. of Petr. Eng. doi:10.2118/36361-JPT

117. Warpinski, N.R., Wolhart, S. L. and Wright, C. A., 2004. Analysis and Prediction of Microseismicity Induced by Hydraulic Fracturing. Soc. Of Petr. Eng. J. 9 (1): 24-33. SPE-87673-PA. doi: 10.2118/87673-PA.

118. Waterman, P. C. and Teutonico, L. J., 1957. Ultrasonic Double Refraction in Single Crystals: J. Appl. Phys., 28, 266-270.

119. Winterstein, D. F. and Meadows, M. A., 1991a. Shear-Wave Polarizations and Subsurface Stress Directions at Lost Hills field: Geophys., 56, 1331-1348.

120. Winterstein, D. F. and Meadows, M. A., 1991b. Changes in Shear-Wave Polarization Azimuth with Depth in Cymric and Railroad Gap Oil Fields: Geophys., 56, 1349-1364

121. Winterstein, D. F. and Meadows, M. A., 1995. Analysis of Shear-Wave Polarization in VSP Data: A Tool for Reservoir Development. Soc. of Petr. Eng. doi:10.2118/23543-PA

122. Winterstein, D. F., De, G. S. and Meadows M. A., 2001. Twelve Years of Vertical Birefringence in Nine-Component VSP Data. Geophys.; 66 (2): 582–597. doi: https://doi-org.ezproxy.lib.ou.edu/10.1190/1.1444950

123. Wong, Teng-fong, Christian, D. and Beatriz, M., 2004. Chapter 2 "Mechanical Compaction" in Mechanics of Fluid-Saturated Rocks. Intern. Geophys. 89. 55-114. 10.1016/S0074-6142(03)80018-9.

124. Wuestefeld, A., Al-Harrasi, O., Verdon, J. P., Wookey, J. and Kendall, J. M., 2010. A Strategy for Automated Analysis of Passive Microseismic Data to Image Seismic Anisotropy and Fracture Characteristics, Geophys. Prosp., 58 (5), 755–773, doi:10.1111/j.1365-2478.2010.00891.x.

125. Yuster, R. T. and Calhoun, J. C., Jr., 1945. “Pressure Parting of Formations in Water Flood Operations – Part II”, Oil Weekly.

126. Yuster, S. T. and Calhoun, J. C., Jr., 1945. “Pressure Parting of Formations in Water Flood Operations – Part I”, Oil Weekly.

127. Zeng, Z., 2002. Laboratory Imaging of Hydraulic Fractures Using Microseismicity, PhD Dissertation, University of Oklahoma, Norman: 1-201.

128. Zoback, M. D., Rummel, F., Jung, R. and Raleigh, C. B., 1977. Laboratory Hydraulic Fracturing Experiments in Intact and Pre-Fractured Rock. Int, J. Rock Mech. Sci and Geomech Abstr., V. 14(2): 49-58.

8 APPENDIX

8.1 Sensor Locations

The schematic in Figure 8.1 shows the sensor locations of the 16 transducers on the rock samples (TSU-6, PY-1 and PY-2). The sensor locations are in cartesian co-ordinates (X, Y and Z). The azimuthal angles measured clockwise from the (+) Y- direction. The co-ordinates and the azimuthal data are listed in Table 8-1 for a sample of diameter 152.6 mm. The radial distance from the Z-axis for sensors 1-14 (that are mounted on the cylindrical surface) are 76.3 mm. Sensor 15 and 16 are mounted on the top and hence the radial distance from the Z-axis is zero. There are no delay times associated with the compressional wave transit on each transducer.

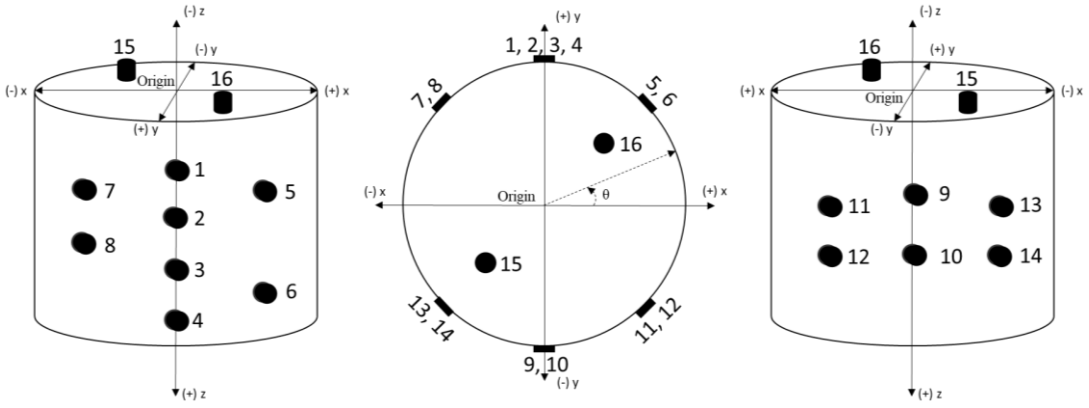

Figure 8.1 Schematic diagram of sensor locations on rock sample

Table 8-1 Cartesian and radial co-ordinates of transducer sensors. Note that R = 76 mm for all the surface mounted transducers (1-14) and 30 mm for the two top transducers (15-16)

Sensors	X (mm)	Y (mm)	Z (mm)	θ (degrees)
1	0	76	30	90
2	0	76	60	90
3	0	76	90	90
4	0	76	120	90
5	53.74	53.74	45	45
6	53.74	53.74	105	45
7	-53.74	53.74	45	135
8	-53.74	53.74	75	135
9	0	-76	60	270
10	0	-76	100	270
11	53.74	-53.74	50	315
12	53.74	-53.74	100	315
13	-48.85	-58.22	50	230
14	-48.85	-58.22	100	230
15	-32.53	-32.53	0	225
16	32.53	32.53	0	135

8.1 Calibration using pencil lead break

AE vents are calibrated using Hsu-Nielsen analysis (Hsu and Breckenridge, 1981). The objective of the calibration is to check the sensor contact with the sample and to check the accuracy of the acoustic emission locations program. Artificial AE events are generated using 0.5 mm pencil leads as shown in Figure 8.2.

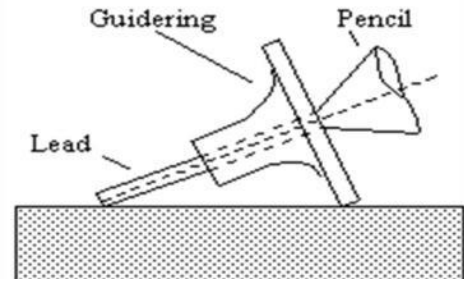

Figure 8.2 Calibration of acoustic emission system using Hsu-Nielson analysis (Gross, 2002)

Pencil break calibration is performed before experiment for all the three samples. The pencil break was performed on eight different pre-defined locations on the sample surface. The AE events were recorded during each pencil breaks and the arrival times were used to locate the recorded events. Subsequently, the absolute error associated with location were calculated for the simulated events. Table 8-2 shows the location of the pencil breaks in cartesian and cylindrical coordinates:

Table 8-2 Location of pencil breaks for AE system calibration

Event no.	X (mm)	Y (mm)	Z (mm)	Angle (degrees)
1	0	36	0	90
2	-25.45	25.45	0	135
3	-36	0	0	180
4	-25.45	-25.45	0	225
5	0	-36	0	270
6	25.45	-25.45	0	315
7	36	0	0	0
8	25.45	25.45	0	45

A constant velocity model is used for Tennessee sandstone sample, TSU-6 whereas an anisotropic velocity model is used for pyrophyllite (PY-1, PY-2) to locate the pencil break AE events.

Absolute error is defined as the distance between the simulated pencil break and the located events (Zeng, 2002) and is calculated using equation (8-1).

$$\text{Absolute error} = \sqrt{(x_s - x_i)^2 + (y_s - y_l)^2 + (z_s - z_i)^2} \qquad (8\text{-}1)$$

The Z-coordinates for all the simulated events are zero in all the pencil break calibration for the three samples. Only X and Y coordinates are computed using the source location algorithm. Hence, only the plan view is shown for each sample in Figure 8.3, where black circles represent

the simulated pencil break locations (known locations) while the red circles represent calculated locations generated by the source location program.

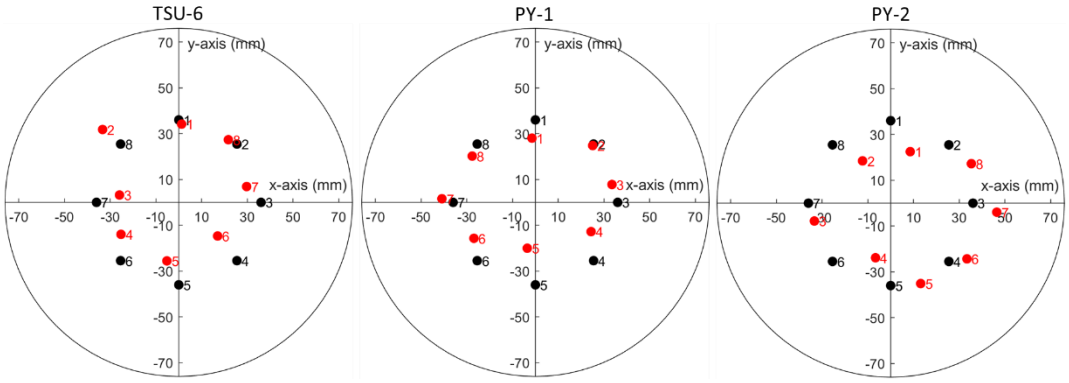

Figure 8.3 Pencil break calibration for the three samples (TSU-6, PY-1 and PY-2). Black circles represent the simulated pencil break locations. Red circles represent calculated locations.

Table 8-3 shows the summary of the average absolute error for each sample in locating the pencil break locations:

Table 8-3 Summary of results from calibration analysis of the three samples

Sample ID	Avg. Velocity (km/s)	Avg. Absolute error (± mm)
TSU-6	3.260	4.875
PY-1	4.182	7.354
PY-2	4.073	9.358

Tennessee sandstone sample (TSU-6) being isotropic has the least error associated in the calibration. Average absolute error in pyrophyllite samples are nearly twice that observed in Tennessee sandstone.

8.2 Equipment specifications

Table 8-4 describes the GX6021 Coax connector pins:

Table 8-4 Group A-D in GX0621 card

Pin	Transmitter Transducer	Function	Pin	Receiver Transducer	Function
A	Parent	CH 1A	M	Parent	CH 1C
B	1	CH 2A	N	1	CH 2C
C	2	CH 3A	P	2	CH 3C
D	3	CH 4A	R	3	CH 4C
E	4	CH 5A	S	4	CH 5C
F	5	CH 1B	T	5	CH 1D
H	6	CH 2B	U	6	CH 2D
J	7	CH 3F	V	7	CH 3D
K	Not used	CH 4B	W	Not used	CH 4D
L	Not used	CH 5B	X	Not used	CH 5D

Input waveform from the high voltage generator is sent to Pin A connector. The software switches to connect Pin A to Pin B to allow passing of signal on to transducer 1. Consequently, at the receiver end, pin M is connected to pin N by relay switching to receive the output signal after the signal passes through the rock sample. After data has been acquired and recorded for transducer 1, automatic relay switch occurs to connect pin A with pin C to send the signal to transmitter transducer 2 and pin M is connected to pin R through relay switching to receive the corresponding signal from receiver transducer 2.